The Dissertation Committee for Nihal Arju Certifies that this is the approved version of the following dissertation:

Fano-Resonant Plasmonic Metasurface for Cancer Detection using Few-Cell Spectroscopy and Other Optical Applications in Mid-Infrared

Committee:

Gennady Shvets, Supervisor

Andrea Alù

Ernst-Ludwig Florin

Xiaoqin Li

Konstantin Sokolov

Fano-Resonant Plasmonic Metasurface for Cancer Detection using Few-Cell Spectroscopy and Other Optical Applications in Mid-Infrared

by

Nihal Arju, B.Sc., M.S.

Dissertation

Presented to the Faculty of the Graduate School of

The University of Texas at Austin

in Partial Fulfillment

of the Requirements

for the Degree of

DOCTOR OF PHILOSOPHY

The University of Texas at Austin

August 2016

Dedicated to my parents.

Acknowledgements

Without the help of many people the work presented here would not be possible. Thanks to my graduate advisor Prof. Gennady Shvets, who guided the research and provided funding for the work. Thanks to my thesis committee for feedback and support. Especially Prof. E.L. Florin, who provided many valuable feedback and was enormously supportive. Thanks also to Prof. George Shubeita. Thanks to Profs. Mahajan and Valanju for lending a sympathetic ear and many hours of enlightening discussions. Thanks to Prof. Keto for all his help and being available, even at the last minute, when I needed his assistance. Thanks to Prof. Donglei Fan, Prof. Vernita Gordon, Prof. Hatice Altug, and Prof. Igal Brener for collaborating with us on various projects. My labmates provided invaluable support. Burton Neuner helped me learn to use the FTIR, and was available to answer questions even after he graduated, for which I am grateful. It was a pleasure to work with David Fozdar, and I am indebted to him for helping me get familiar with the JEOL electron beam lithography system. It is a monster without some friendly advice. Chih-Hui Wu and I worked on several projects and he was an excellent partner to work with, and a friend. Thanks also to Hossein Mousavi and Nima Dabidian. Shourya Dutta Gupta arrived late to the group, but his cheerful energy was contagious. I wish him all the luck. Thanks also to Simeon for discussing sundry topics at any hour. Thanks to Alexander Khanikaev for teaching me the coupled mode theory, how to write a paper, and having an open door. Tzuhsuan Ma helped with various projects, and he always amazes me with the brilliance, energy, and speed with which he does things. Glen Kelp, David Puerteseladze, Albert Lee, Esteban Esquivel, and Chao Liu were closely involved

with many projects I have worked on. Thanks to Kueifu Lai, Xi Zhang, Carl Siemon for their help with various things at various times.

I am deeply indebted to my parents. Without their thoughtful and selfless upbringing of us we could not hope to travel the distance us, their children, have. Thanks to my sisters, who have cheered me up at trying times. Thanks to my wife who helped with too many things to name, and was a driver for personal growth.

There are many friends who I must thank— Ehab and Marwa Hassan, Anindya Dey, Cynthia Correa, Heidi Seinige, Sudip Mondal, Reshmi Mondal, Naser Mohammed, Ashfaq Shukoor, Naveed Arsalan, Khalid Azam, M. Umer Ismail, Sandipan Kundu, Shivaraj Kandhasamy…

I am leaving out more people than I was able to include in this brief text.

Fano-Resonant Plasmonic Metasurface for Cancer Detection using Few-Cell Spectroscopy and Other Optical Applications in Mid-Infrared

Nihal Arju, PhD

The University of Texas at Austin, 2016

Supervisor: Gennady Shvets

The field of metamaterials holds enormous promise in our ability to engineer artificial ('meta') material to suit a wide variety of needs. Metamaterials have been designed to achieve electromagnetic cloaking, negative refractive index, perfect absorption and many other phenomena that were thought to be impossible to achieve. Fano resonant metamaterials form a subclass of metamaterials that possess one or more Fano-type resonances. The Fano resonance arises out of interference between two resonance modes with disparate lifetimes. A variety of Fano resonant asymmetric metamaterials (FRAMMs) have been investigated in this dissertation. A circularly dichroic double continuum FRAMM was constructed and the effect of tuning the interference between modes on a Fano resonance has been examined. These metamaterial surfaces (metasurfaces) have strong field confinement. As a result, a small change in the near vicinity of the metasurface creates a detectable change in the metasurface response, which allows the metasurfaces to be used as sensors. The FRAMM was used to detect monolayer of protein otherwise undetectable using Fluorescence microscopy. It was also used to examine different cell types. One promising strategy for early cancer detection involves detecting cancerous cells in the bloodstream. These circulating tumor cells

(CTCs) spread through the body and create tumors. Metasurface sensors may be used to conduct spectroscopy on cells in order to spectroscopically identify different cell types, including whether the cells are cancerous or not. A statistical analysis reveals that it is possible to detect different cell types using metasurfaces.

Table of Contents

List of Tables

List of Figures

SECTION A : INTRODUCTION

This dissertation is structured as follows: This section introduces the different topics, and how they tie together. Section B focuses on Metamaterial, or specifically, metasurfaces as sensing platforms. We explore in detail one type of metasurface (the `double continuum Fano resonant asymmetric metasurface' (FRAMM) or `pi structure') that we used in later studies. In Section C we explore the use of the FRAMM for sensing of monolayer protein, and for spectroscopically distinguishing cell types. Below is a brief overview of the motivation for this work.

A.1.1 METAMATERIALS

Metamaterials and metasurfaces[12] represent a remarkably versatile platform for light manipulation[3–6], biological and chemical sensing[7–10], and nonlinear optics[11–13]. Many of these applications rely on the resonant nature of metamaterials, which is the basis for extreme spectrally selective concentration of optical energy in the near field. In addition, metamaterial-based optical devices lend themselves to considerable miniaturization because of their subwavelength features. This additional advantage sets metamaterials apart from their predecessors, photonic crystals, which achieve spectral selectivity through their long range periodicity[14].

Traditional approach to materials is— Nature has provided materials with specified properties, and we pick and choose the ones that fit our needs, if one is available. In the field of metamaterials, the approach is different— we begin with the properties we are looking for in a material, and the goal is to design a material that emulates the desired properties[15,16]. The design process involves altering both the unit

cell and periodicity. This has allowed physicists to set on quests for the perfect absorber[17–22], the metamaterial cloak[23–27], and the perfect lens[28] etc. Metamaterials have opened up countless new opportunities in the field of electromagnetics and outside, by fundamentally altering how we think about materials. Some of these have already been demonstrated. This do-it-yourself material approach has expanded into other fields like acoustics[26,29–32].

The name metamaterial refers to the fact that these materials are artificial (`meta' or `beyond'). The first known work in this field was by Jagadish Chandra Bose[33–35] in 1898 at Presidency College, Kolkata. Bose investigated change of polarization of electromagnetic wave passing through twisted jute. The relatively more modern work of Victor Veselago[36–38] in 1967 is better known[38]. It is, however, the work of Sir John Pendry[28] that set off the field with his identification of a practical method of achieving negative index metamaterial in microwave.

Plasmonic metamaterials can be engineered to have tailored electromagnetic response over a broad range of frequencies: from visible to THz. Their optical properties go beyond those achievable using naturally-occurring optical materials, exhibiting a number of exotic phenomena which include negative refractive index, strong chirality, and indefinite electric permittivity[39–43]. Metamaterials manifesting these unusual optical properties are typically comprised of highly-resonant plasmonic elements (e.g., split-ring resonators) which have a spectrally-narrow response and high local field concentration.

In this work, we shall be concerned with metamaterials that show the so called Fano resonance[44]. In the field of atomic physics observed asymmetric ionization spectra inspired the work of Ugo Fano who in his breakthrough paper[44] explained asymmetric ionization spectra in atoms. To explain the phenomenon, Fano introduced interference

between discrete and continuous states of the atom. This type of resonance is now referred to as Fano resonance. The concepts of Fano resonance, interference, and line shape have been applied to several areas of optical science, including photonics, plasmonic nanostructures, and metamaterials[45–49]. The sharp spectral features in Fano-resonant metamaterials, combined with strong optical energy concentration, make them attractive for sensing and fingerprinting[19,34,35,50] and nonlinear[51,52] applications.

A.1.2 BIOSENSING

In-depth understanding of life-sustaining biomolecular binding processes has the potential for impacting every corner of life sciences and medicine[53,54]. In Section C we discuss biosensing using a plasmonic metamaterial sensor that we developed. We discuss two examples of biosensing using metamaterials— (i) sensing a monolayer of protein and (ii) distinguishing different cell types.

Protein Monolayer

Plasmonic metamaterials and single meta-molecules have recently emerged as a powerful photonic platform for sensing applications[9,18,35,55,56] and have been used for linear and nonlinear surface-enhanced spectroscopies[9,57,58]. Especially important for biosensing applications are infrared metamaterials, because bio-molecules possess mid-infrared vibrational fingerprints that can be used for their identification, thereby improving specificity of bio-detection[59].

In general, conformational rearrangements in biomolecular structures are required for matching of the binding sites between the host-guest molecules[60,61]. However, state-of-art biosensing techniques can only probe the biomaterial accumulations due to molecular bindings[62–64], not the underlying conformational alterations required for binding processes to occur[65]. While surface-enhanced Raman and infrared absorption spectroscopies[9,57,58,66,67] can provide the vibrational signatures of molecular conformational states[68–70], these spectroscopic approaches are not directly compatible with "gold standard" biosensing techniques[63] due to fundamentally different working principles.

Distinguishing Cell Types

Another possible application of these metamaterial sensors is in distinguishing different cell types using spectroscopy. While this study is motivated by the need for early cancer detection, the method is general and may be used for various other purposes— diagnostic, research and others. In fact the methods described here may easily be extended to study subtle changes in chemical composition in a variety of different situations. Different cell types have different function, and as a result their chemical compositions are expected to be different. Spectroscopy is a powerful tool to query chemical changes.

Cancer is the second largest cause of death in the United States and worldwide in the 21st century[71,72]. Worldwide an estimated 8 million peopled died of cancer in 2012; 30% of whom would have survived if cancer was detected earlier, according to the World Health Organization (WHO) 90% of all cancer deaths occur due to metastasis, which is the spread of cancer through a patient's blood[73].

Early detection of cancer, therefore, is an important tool for prevention of cancer related deaths. It significantly improves the chances of the patient survival. Cancer screening, or tests on prima facie healthy individuals to determine if there is a cancerous tumor in its early stages present in the body, will help early intervention. Breast cancer and cervical cancer screenings are performed using mammograms and pap smears[72]. Screening is effective when it can be performed on a large population in relatively short time, with relatively small staff members. WHO advocates cancer screening for only breast and cervical cancer based on effectiveness and availability of screening methods. For the vast majority of cancer types, screening is not available or practical in large scale.

Since cancer spreads through blood, detection of the spread of cancer through a patient's blood will allow treatment to begin before cancer spreads and becomes harder to cure or manage. In this work, we investigate a sensor based inexpensive and automated approach to cancer detection which has the potential to make cancer screening available in mass scale.

SECTION B : METASURFACE SENSING PLATFORMS

Chapter B.1: Introduction to the Fano Resonant Plasmonic Nanostructures

In this section of the dissertation I will focus on planer metamaterials, or metasurfaces. These surfaces were used for sensing application. We shall discuss these uses later in Section C. Here I shall discuss three of the metasurfaces that I investigated.

Firstly, I shall discuss the metallic double continuum Fano resonant structure (or FRAMM, or Pi structure) which was extensively used in biosensing applications. In this work, classical realization of a quantum mechanical phenomenon of double-continuum Fano interference using metasurfaces is experimentally demonstrated by engineering the near-field interaction between two bright and one dark plasmonic modes. The competition between the bright modes, one of them effectively suppressing the Fano interference for the orthogonal light polarization, is discovered. Coherent control of optical energy concentration and light absorption by the ellipticity of the incident light will be demonstrated theoretically.

Next, I shall discuss a circularly dichroic structure. We focused on circular dichroism and its connection to Ohmic losses for this study. It is a phenomena that arises out of interaction of internal degrees of freedom of electromagnetic waves with chiral materials, which is made of elements (molecules or metamolecules) that lack mirror symmetry. Optical activity is observed in naturally occurring material like sugar[74,75], and more recently in metamaterials. While the origin of optical activity is well known, it has

never been directly visualized on a chiral medium. By measuring amplitudes and phases of optical near fields we experimentally demonstrate that the circular dichroism in a metasurface emerges as a result of Fano interference that leads to a polarization dependent Ohmic loss.

Chapter B.2: Metallic Double Continuum Fano Resonant Metasurface (FRAMM)[1]

B.2.1 INTRODUCTION

Most of the recently reviewed[47,48,76] work on optical Fano resonances deals with near-field coupling between a single bright and a single dark resonance, respectively, emulating the continuum and discrete atomic states. However, the original Fano paper addressed a much broader class of couplings between atomic states, including one discrete and multiple continuum states. The key difference between the single-continuum and double-continuum cases is that the ionization probability vanishes for at least some values of energy loss of the ionizing particle in the former but not in the latter case[44]. Thus, the magnitude of Fano interference can be suppressed by the second continuum state.

Here we report the realization of the optical analog of double-continuum Fano (DCF) interference using a circularly dichroic (CD) plasmonic metasurface shown in Figure B.2-1, which supports one dark and two bright plasmonic modes. The modes are controllably coupled to each other in the near field through symmetry-breaking vertical displacement s_y of a horizontal nanorod coupler (HNC) from its symmetric position. Our experimental measurements of Fano-shaped polarized reflectivity spectra $R_{xx}(\lambda)$ and $R_{yy}(\lambda)$ shown in Figure B.2-2 (a) and (b) reveal a new optical phenomenon of continuum state competition in asymmetric photonic structures: the presence of the second (e.g., γ-

[1] The work in this chapter is based on a collaboration with coauthors in— Nihal Arju , Tzuhsuan Ma, Alexander B. Khanikaev, David Purtseladze, and Gennady Shvets, "Optical Realization of Double-Continuum Fano Interference and Coherent Control in Plasmonic Metasurfaces," Physical Review Letters, 114 (237403). Arju designed and fabricated the structures and performed the simulations. Ma, Khanikaev, Purtseladze and Arju worked on the analytic theory. Arju wrote the paper. Prof. Shvets edited the paper to its final version. Prof. Shvets guided the project.

polarized) continuum state can significantly affect the strength of the Fano interference of the dark state with the first (e.g., x-polarized) continuum state.

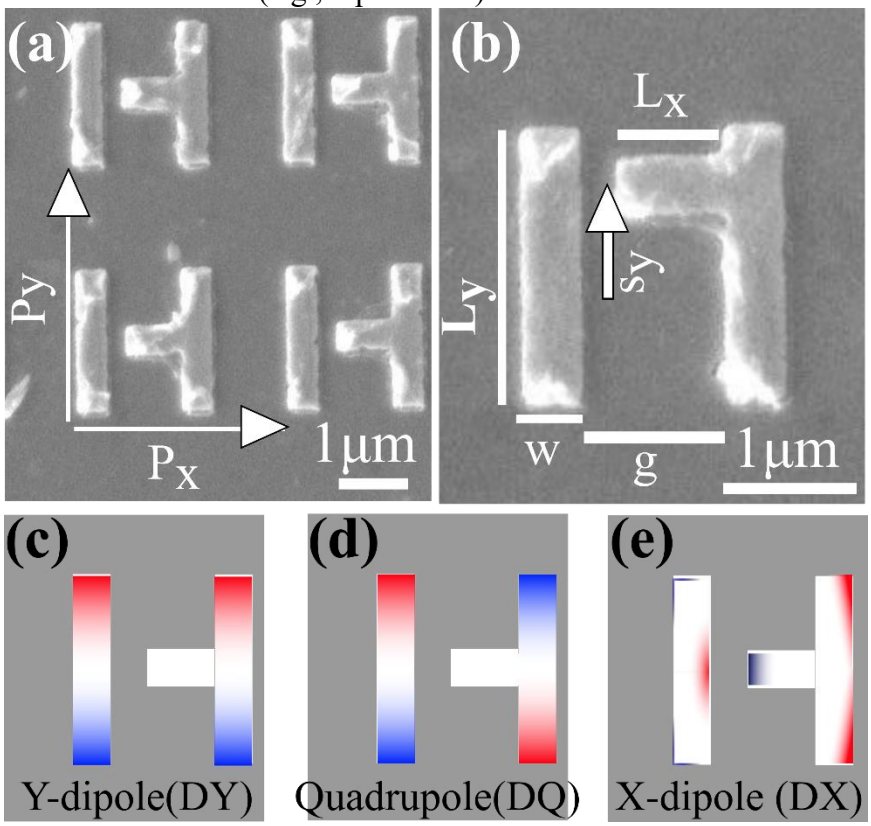

Figure B.2-1: (a) Scanning electron micrograph of a fabricated DCF metasurface. (b) Geometry definitions of a unit cell ($s_y = \ 0.52\ \mu m$). For all metasurfaces: $P_x = 2.7, P_y = 3.15, w = 0.36, L_x = 0.92, L_y = 1.8$, and$g = 0.66\mu m$. (c)–(e) Charge distributions of the three unperturbed eigenmodes of the symmetric ($s_y = 0$) metasurface. (c) and (e) Bright DY and DX, (d) dark DQ.

Unlike the plasmonic phenomenon[77] of the Fano feature reduction by nonradiative (Ohmic) losses, the continuum state competition directly emulates the atomic systems where the nonradiative decay rate of the discrete state is naturally negligible. This phenomenon was not addressed in the earlier optical DCF work[78,79] because the relative mode coupling cannot be controlled in a fixed geometry structure. An important practical

implication of DCF is the possibility of controlling the intensity of light concentrated at the metasurface using the ellipticity of the incident optical beam. Specifically, we demonstrate that by simply adjusting the phase difference between the x- and y-polarized electric field components of incident light, one can vary the intensity of concentrated light by more than an order of magnitude. Such coherently controlled optical field enhancement can be utilized for sensing and nonlinear applications. Moreover, because light intensity determines its absorption, CD metasurfaces open a new path to interference-based control of single-beam absorption, which is reminiscent of two-channel coherent absorbers[80] The consequences of such coherent absorption control include giant CD in absorption and transmission[81].

B.2.2 Experimental Results

A family of gold metasurfaces shown in Figure B.2-1 with different symmetry-breaking parameters s_y were fabricated on CaF_2 substrates using electron beam lithography. The lowest plasmonic resonances of the metasurfaces shown in Figure B.2-1 are classified as one dark quadrupolar (DQ) and two bright dipolar (DX and DY) plasmonic modes that are radiatively coupled to incident light polarized in the x and y directions, respectively, giving rise to two quasicontinua of electromagnetic states. The finite displacement s_y of the HNC that perturbs the DQ mode is used to control the coupling between the modes. Polarized reflection coefficients were measured using Fourier transform infrared microspectroscopy. The $R_{yy}(\lambda)$ and $R_{xx}(\lambda)$ spectra shown in Figure B.2-2(a) reveal broad reflectivity peaks inside the shaded (4.5 μm < λ < 6 μm) spectral window, corresponding to the bright DY and DX resonances, respectively. In the rest of the work we concentrate on the $6\,\mu m < \lambda_{DQ}(s_y) < 8\,\mu m$ spectral window containing the dark DQ mode.

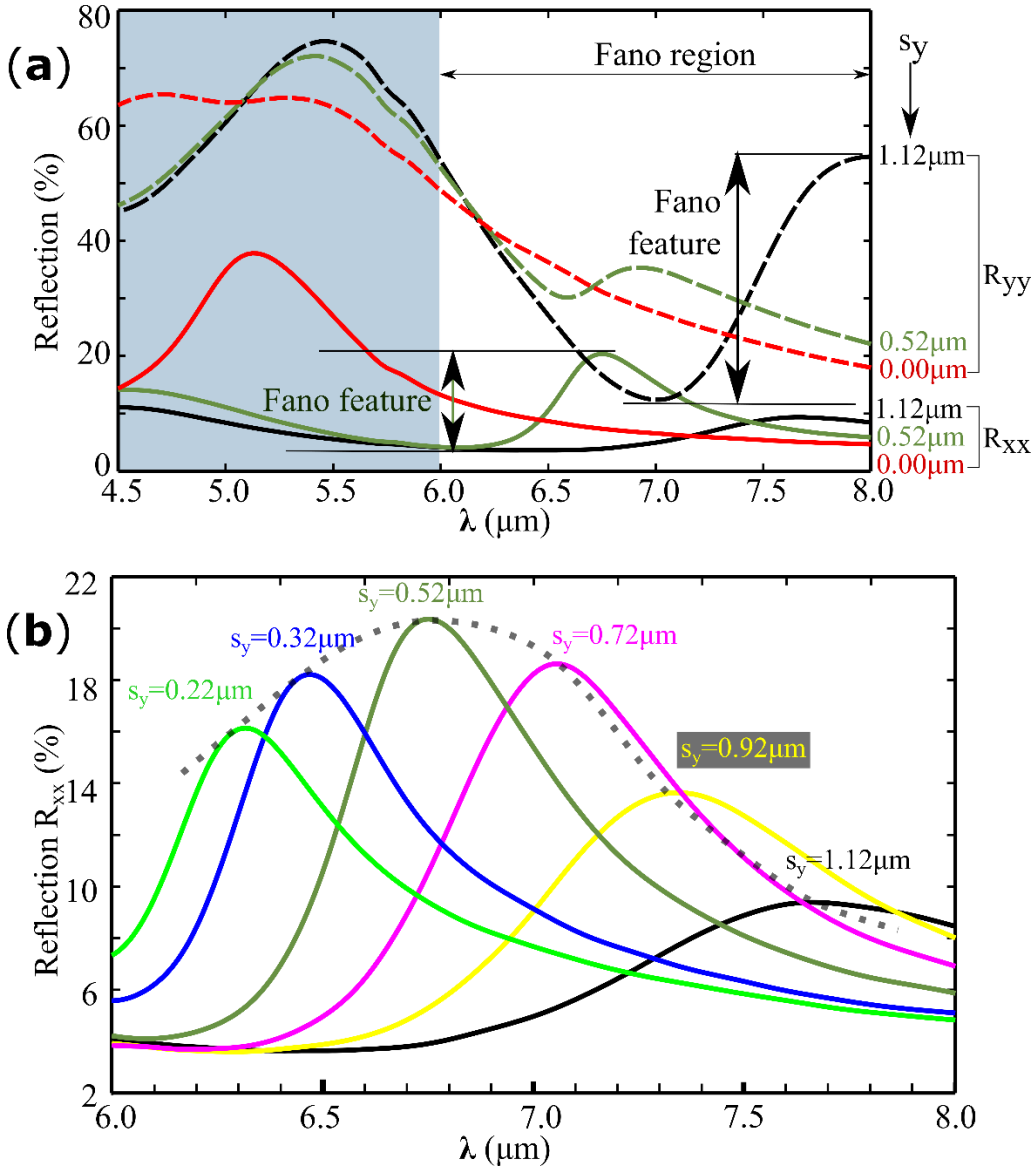

Figure B.2-2: (a) Measured reflectivity spectra R_{xx}(solid lines) and R_{yy} (dashed lines). Fano feature in R_{yy} is larger than in R_{xx} for $s_y = 1.12\mu m$ (black line); the opposite is true for $s_y = 0.52\mu m$ (green line). Fano features are absent for $s_y = 0$ (red lines). (b) Zoomed-in R_{xx} spectra for 0.22 μm < s_y < 1.22 μm. Dotted line: nonmonotonic behavior of the Fano feature with sy interpreted as the competition between x- and y-polarized continua.

Several key observations can be made based on the spectral Fano features measured for a wide range of the symmetry-breaking parameter s_y. First, we conclude from Figure B.2-2 that the relative coupling strengths $\tilde{\kappa}_{XQ}(s_y)$ (between DQ and DX) and $\tilde{\kappa}_{XQ}(s_y)$ (between DQ and DY) vary widely with s_y. This conjecture follows from the very different manifestations of Fano resonance in R_{xx} and R_{yy} spectra. Specifically, for small values of $s_y < L_y/4$, the Fano feature in the x polarization becomes strongly pronounced while it is barely noticeable in y polarization (e.g., $s_y = 0.52\,\mu m$.) The opposite is true for large values of s_y: the Fano feature in $R_{yy}(\lambda)$ is much stronger than in $R_{xx}(\lambda)$ for $s_y \geq \frac{L_y}{2}$ (e.g., $s_y = 1.12\,\mu m$).

Second, we observe from Figure B.2-3(b) that the magnitude of the Fano feature in x-polarization is nonmonotonic in s_y.The peak value of R_{xx} (dotted line) plotted in Figure B.2-2 (b) increases with s_y, reaches the maximum at $s_y = s_y^{max} = 0.52\,\mu m$ and decreases for $s_y > s_y^{max}$. The decrease of the Fano feature for large values of s_y is unexpected because the coupling coefficient $\tilde{\kappa}_{XQ}(s_y)$ continues monotonically increasing with s_y even for $s_y > s_y^{max}$. The observed decrease is the direct experimental evidence of continuum state competition in DCF originally predicted by Fano for atomic systems. Specifically, the linewidth $\delta\lambda_{DQ}(s_y)$ of the radiatively broadened Fano resonance increases [and the corresponding quality factor $Q(s_y) = \lambda_{DQ}/(\delta\lambda_{DQ})$ decreases] faster with s_y than the coupling coefficient $\tilde{\kappa}_{XQ}(s_y)$, thereby suppressing the Fano feature in R_{xx}.

B.2.3 Theoretical model of DCF in Plasmonic Metasurfaces

To explain these experimental results and to explore the possibility of circularly dichroic optical field concentration, in what follows we develop a simple analytic model of optical DCF. The interaction of light with the three modes (two quasicontinuum and

one discrete) of the metasurface is described by the following equations based on the [45,82] coupled mode theory (CMT):

$$\begin{aligned}\frac{dD_Y}{dt} &= i\tilde{\omega}_Y D_Y + i\kappa_{XY} D_X + \alpha_y E_y^{in},\\ \frac{dD_Q}{dt} &= i\tilde{\omega}_Q D_Q + i\kappa_{XQ} D_X,\\ \frac{dD_X}{dt} &= i\tilde{\omega}_X D_X + i\kappa_{XY} D_Y + \alpha_x E_x^{in}\end{aligned} \qquad \text{B.2-1}$$

where D_X, D_Y, and D_Q are the mode amplitudes, and $\alpha_{x(y)}$ are the radiative coupling efficiencies of the bright resonances to the far-field x- (y-) polarized incident waves with amplitudes $E_{x(y)}^{in}$, respectively. The three modes are characterized by their complex-valued unperturbed eigenfrequencies $\tilde{\omega}_{X,Q,Y} \equiv \omega_m - i\tau_m^{-1}$ ($m = X, Y, Q$ is the resonance's index), where ω_m and τ_m are the spectral position and unperturbed lifetime of the m'th mode, respectively.

Note that the κ_{YQ} component of the near-field coupling tensor κ_{lm} has been neglected in equation B.2-1 in comparison with its $\kappa_{XQ}(s_y)$ and $\kappa_{XY}(s_y)$ components for small value of s_y. Qualitatively, κ_{lm} is proportional to the overlap integral $\vec{E}_l \cdot \vec{E}_m$ inside the region occupied by the HNC. It can be observed from Figure B.2-1 (d)-(f) that (a) E_x is the largest electric field component for all three modes in the said region of space, and (b) E_x at $y = 0$ for the DQ and DY modes. Based on these symmetry considerations (see Appendix D.3 for details), $\kappa_{XQ}, \kappa_{XY} \propto s_y$, but $\kappa_{YQ} \propto s_y^2$ can be neglected for $s_y \ll \frac{L_y}{4}$. As demonstrated below, effective coupling between DQ and DY emerges in the second order of the perturbation theory based on equation B.2-1. The resulting indirect coupling coefficient, while also $\propto s_y^2$, is larger than the neglected direct coupling term κ_{YQ}. Also, from the energy conservation[45,76,81], $1/\tau_{X,Y}^{Ohm} = |\alpha_{x,y}|^2 + 1/\tau_{X,Y}^{Ohm}$, where $1/\tau_{X,Y}^{Ohm}$ are the intrinsic decay rates.

After solving equation B.2-1 in the vicinity of the dark resonance under the small-coupling ($|\kappa_{XY}|, |\kappa_{XQ}| \ll |\omega_Q - \omega_{X,Y}|$) assumption and using the expressions for the complex valued reflection amplitudes[76] $r_{xx(yy)} = \alpha^*_{x(y)} D_{X(Y)} / E^{in}_{x(y)}$, we obtain

$$r_{xx} = \frac{\alpha_x^2}{\omega - \widetilde{\omega}_X} + \frac{\alpha_x^2 \tilde{\kappa}_{XY}^2}{\omega - \widetilde{\omega}_Y} + \frac{\alpha_x^2 \tilde{\kappa}_{XQ}^2}{\omega - \widetilde{\omega}_Q}, \quad \text{B.2-2}$$

$$r_{yy} = \frac{\alpha_y^2}{\omega - \widetilde{\omega}_Y} + \frac{\alpha_y^2 \tilde{\kappa}_{XY}^2}{\omega - \widetilde{\omega}_X} + \frac{\alpha_y^2 \tilde{\kappa}_{YQ}^2}{\omega - \widetilde{\omega}_Q}, \quad \text{B.2-3}$$

Where the normalized coupling coefficients $\tilde{\kappa}_{lm}$ between the modes are given by

$$\tilde{\kappa}_{XY} = \frac{\kappa_{XY}}{(\widetilde{\omega}_X - \widetilde{\omega}_Y)}, \kappa = \frac{\kappa_{XQ}}{\widetilde{\omega}_X - \widetilde{\omega}_Q}, \quad \text{B.2-4}$$

$$\tilde{\kappa}_{YQ} = \tilde{\kappa}_{XY} \tilde{\kappa}_{YQ}$$

The renormalized or redshifted frequency ω'_Q and the radiatively reduced lifetime τ'_Q of the DQ mode are approximated as

$$\omega'_Q = \omega_Q - \frac{\kappa_{XQ}^2}{\omega_X - \omega_Q} - \frac{\kappa_{XY}^2 \kappa_{XQ}^2}{(\omega_X - \omega_Q)^2 (\omega_Y - \omega_Q)}, \quad \text{B.2-5}$$

$$\frac{1}{\tau'_Q} \approx \frac{1}{\tau_Q^{Ohm}} + \kappa_{XQ}^2 \frac{\alpha_x^2}{(\omega_Q - \omega_X)^2} + \kappa_{XY}^2 \kappa_{XQ}^2 \frac{\alpha_y^2 (\omega_X - \omega_Q)^2 + 2\alpha_x^2 (\omega_X - \omega_Q)(\omega_Y - \omega_Q)}{(\omega_Q - \omega_X)^4 (\omega_Y - \omega_Q)^2},$$

where the large modal separation assumption of $|\omega_{X,Y} - \omega_Q| \gg 1/\tau_{X,Y}$ is used.

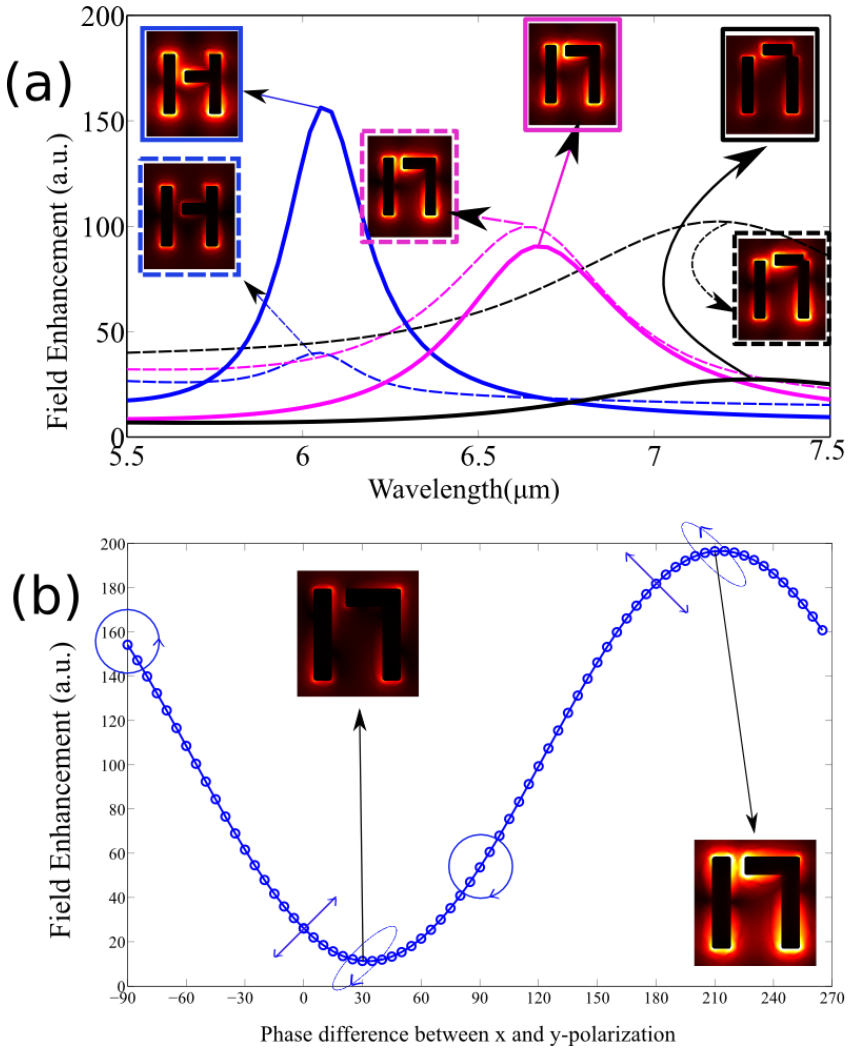

Figure B.2-4: COMSOL simulations of the optical intensity enhancement $\eta = < \left|\vec{E}\right|^2 > / E_0^2$ averaged over all (except metal substrate) metal interfaces in plasmonic DCF metasurfaces. (a) η for x-polarized (solid) and y-polarized (dashed lines) incident light for weak-coupled ($s_y = 0.32\ \mu m$), intermediately coupled ($s_y = 0.72 \mu m$), and strongly coupled ($s_y = 1.12 \mu m$) regimes. Insets: near field profiles. (b) The dependence of η_{max} on the incident light chirality parametrized by the phase shift ϕ (see text) for the $s_y = 0.72\ \mu m$ metasurface. Insets: near-field intensities for $\phi = 30^o$ (left) and $\phi = 210^o$ (right). Closed directional loops indicate the polarization state of incident light as a function for $-90^o < \phi < 270^o$.

The two key features of the experimentally measured $R_{xx(yy)} \equiv \left|r_{xx(yy)}\right|^2$ reflectivity spectra can now be understood by examining the dependence of the Fano feature's magnitude $r_{xx(yy)}^{Fano}$ on s_y. It is given by the third term in the right-hand side of equations B.2-2 and B.2-3 evaluated at $\omega = \omega_Q'$:

$$r_{xx}^{Fano} \propto \frac{\alpha_x^2 s_y^2}{\frac{1}{\tau_Q^{Ohm}} + \beta s_y^2 + \gamma s_y^4}, \qquad \text{B.2-6}$$

$$r_{yy}^{Fano} \propto \frac{\alpha_y^2 s_y^4}{\frac{1}{\tau_Q^{Ohm}} + \beta s_y^2 + \gamma s_y^4},$$

where β and γ follow from equation B.2-5.

We observe that the decay rate of the DCF resonance given by the denominators of equation B.2-6 can be broken up into three contributions: (a) the Ohmic (nonradiative) contribution, (b) the contribution $\propto s_y^2$ corresponding to the radiative decay into the x-polarized continuum, and (c) the contribution $\propto s_y^4$ corresponding to the radiative decay into the y-polarized continuum. Depending on the relative dominance of these three mechanisms controlled by s_y, the three respective coupling regimes can be identified as the (i) weak coupling regime ($s_y < L_y/4$), (ii) intermediate coupling regime ($L_y/4 < s_y \ll L_y/2$), and (iii) strong coupling regime ($s_y \sim L_y/2$). The transition from weak to strong coupling regimes with increasing s_y explains the decrease of the quality factor of the Fano resonance with s_y evident from Figure B.2-2(b). The experimentally estimated quality factors of the DQ mode drop from its Ohmic loss limited value[49] of $Q = 13$ to $Q = 7$ (strong y-polarized radiative loss) as s_y increases from $s_y = 0.22$ to $s_y = 1.12\mu m$.

The slower emergence of the Fano feature in the R_{yy} spectrum compared with the R_{xx} (first observation) can be understood from the scaling of $r_{yy}^{Fano} \propto s_y^4$ versus $r_{xx}^{Fano} \propto s_y^2$ in the weak coupling regime. The situation changes dramatically for $s_y \geq L_y/2$ and

the Fano feature in R_{yy} becomes stronger than in R_{xx} because of the $\alpha_y > \alpha_x$ relationship which is the consequence of $L_y > L_x$. The second observation is also explained by the nonmonotonic dependence of r_{xx}^{Fano} on s_y due to the transition to strong coupling regime, where the continuum state competition in DCF is responsible for the weakening of the Fano feature in R_{xx} for large s_y.

B.2.4 CIRCULARLY DICHROIC OPTICAL ENERGY CONCENTRATION BY DCF METASURFACES

It has been long recognized that one of the attractions of Fano-resonant structures is strong optical field enhancement due to the excitation of dark plasmonic resonances. Below we demonstrate that coherent (phase) control of optical field concentration can be accomplished through interference by engineering a general elliptic polarization state of the incident light. First, we calculate the amplitude D_Q of the dark resonance in the proximity of the DQ mode in response to the incident light with complex-valued amplitudes $(E_x, E_y) = E_0(1, \exp i\phi)/\sqrt{2}$. Here, φ is the relative phase between the x and y polarizations that determines the state of elliptic polarization as illustrated in Figure B.2-4(b). At the Fano resonance, the amplitude of the dark mode is expressed from equation B.2-1 as $D_Q = \left(\frac{E_0}{\sqrt{2}}\right)\left[q_{xx} + \exp(i\phi)\, q_{yy}\right]/(\omega - \widetilde{\omega}_Q')$ where

$$q_{xx} = \frac{\alpha_x \kappa_{XQ}(s_y)}{\widetilde{\omega}_X - \widetilde{\omega}_Q} \qquad \text{B.2-7}$$

$$q_{yy} = \frac{\alpha_y \kappa_{XQ}(s_y)\kappa_{XY}(s_y)}{(\widetilde{\omega}_X - \widetilde{\omega}_Q)(\widetilde{\omega}_Y - \widetilde{\omega}_Q)}$$

are complex-valued field enhancement coefficients.

Because of the different scaling of q_{xx} and q_{yy} with s_y, it follows from equation B.2-7 that in the weak (strong) coupling regime the strongest field enhancement is achieved for the $x - (y-)$ polarized light. This is confirmed by electromagnetic COMSOL

simulations of the surface-averaged optical intensity enhancement $\eta \equiv < \left|\vec{E}\right|^2 > E_0^2$ shown in Figure B.2-4 (a) for the $x-$ and $y-$polarized light incident on DCF metasurfaces with different values of s_y. An even more remarkable conclusion derived from equation B.2-7 is the possibility of controlling the field enhancement using elliptically polarized light.

The resulting CD (i.e., the dependence of $\eta \propto \left|D_Q\right|^2$ on ϕ) is the consequence of the finite phase difference $\Delta\phi = \arg(\frac{q_{xx}}{q_{yy}})$: the field enhancement is maximized (minimized) for $\phi_{max} = \Delta\phi (\phi_{min} = \Delta\phi + \pi)$ due to the constructive (destructive) interference between the two excitation pathways. Moreover, symmetry properties of the coupling coefficients κ_{XQ} and κ_{XY} ensure the following property of the structure's enantiomeric partner produced by displacing of the HNC to the opposite side ($s_y \to -s_y$) of the symmetry plane: $\left|D_Q\right|(\phi, -s_y) = \left|D_Q\right|(\phi + \pi; s_y)$.

These qualitative results are confirmed by COMSOL simulations carried out for the $s_y = 0.52\mu m$ structure chosen because $|q_{xx}| \approx |q_{yy}|$ according to Figure B.2-5 (b). The peak enhancement factor $\eta_{max}(\phi) \equiv \eta(\lambda_Q', \phi)$ plotted in Figure B.2-4 (b) reveals strong CD. The ratio of the highest ($\phi_{max} \approx 210^o$) to lowest ($\phi_{min} \approx 30^o$) near-field intensities is ≈ 20, and the enhancement ratio for right-hand circularly polarized light ($\phi = -90°$) is ≈ 3 times higher than for the left-hand circularly polarized light ($\phi = 90°$).

Because $\eta_{max}(\phi)$ and peak Ohmic loss $A(\phi)$ are proportional to each other, ϕ emerges as a powerful tool for controlling the absorption using the interference of the polarization components of elliptically polarized light. For example, we find for the DCF metasurface shown in Figure B.2-4 (b) that $A(\phi_{min}) \approx 1.5\%$, i.e., the absorption is coherently suppressed. On the other hand, $A(\phi_{max}) = 41\%$, i.e., the absorption is

coherently enhanced almost to the absolute absorption limit ($A_{lim} = 50\%$) of a thin layer in vacuum[83]. Another important consequence of the related giant CD absorbance of the DCF metasurface ($A_{RCP} = 30\%$ versus $A_{LCP} = 13\%$) is that it exhibits circular conversion dichroism[46] due to the dissipation asymmetry between right-hand circularly polarized and left-hand circularly polarized light.

B.2.5 Conclusion and Outlook

We have demonstrated that a quantum mechanical phenomenon of double continuum Fano interference can be classically emulated using an asymmetric plasmonic metasurface. The relative coupling strength between the discrete and two continuum states, distinguished from each other by their polarization, were experimentally varied by changing the degree of symmetry breaking of the metasurface. The phenomenon of continuum state competition, by which one of the continuum states suppresses the Fano resonance for the orthogonal light polarization, was observed and analytically explained. This work opens new possibilities for controlling optical energy concentration on the nanoscale using the ellipticity state of the incident light, thereby providing a simple and powerful tool for developing novel nanophotonic applications such as sensors and detectors.

Chapter B.3: Circular Dichroism in FRAMM

B.3.1 INTRODUCTION

Optical activity (or optical rotation or polarization rotation) was first noted by passing light through so called `chiral' material[33]. It is an interesting physical phenomenon originating from the interaction of internal degrees of freedom of electromagnetic waves with chiral materials in which constituent molecules lack mirror or central symmetries in three-dimensional space. In natural materials, however, this effect is relatively weak. In engineered chiral materials (or chiral metamaterials), it can be significantly enhanced. In the unit cell of these metamaterials, the mirror symmetries are broken between left and right on a wavelength scale. Although originally discovered in structures with three dimensional chirality, optical activity is also possible in two-dimensional metasurface, where is emerges in the form of circular dichroism. While the origin of optical activity is well known, it has never been directly visualized on a chiral medium. In this work, by measuring amplitudes and phases of optical near fields we demonstrate for the first time the circular dichroism in a metasurface emerges as a result of Fano interference that leads to a polarization dependent Ohmic loss.

Due to their underlying three-dimensional structure, optical materials can possess handedness - a form of spatial symmetry breaking discriminating between "left" and "right" when the mirror image of the material constituents does not coincide with themselves. Among the most exemplary cases of such property, referred to as *chirality*, are probably those found in quartz, whose crystalline structure occurs in either left- or right-handed form, and organic molecules, such as proteins and nucleic acids, which mysteriously occur in nature predominantly in a homochiral form[75]. Similarly, due to its

vector nature, light waves also naturally possesses two forms of handedness and can exist as left and right circularly polarized wave. When interacting with chiral materials, light of opposite handedness perceives different refractive indices as is observed in circular birefringence or experiences unequal absorption rates, phenomenon referred to as circular dichroism.

Although typically quite weak in naturally occurring materials, optical activity plays an important role in crystalline and protein structure characterization, biosensing, biological and medical applications[75]. Thanks to recent advances in the field of metamaterials, it is now possible to engineer synthetic chirality by structuring media in a way reducing the left-right symmetry on a subwavelength scale and to create optical media with unprecedentedly strong optical activity. Moreover, the ability to engineer chiral resonances in metamaterials and to concentrate optical field in their proximity brings the possibility to strongly enhance weak responses of natural optically active materials[81,84–91].

One of the most promising approaches to strong optical activity is based on chiral Fano-resonant metasurfaces (FRMs)[8,35,46–49,76,92]. FRMs represent ultrathin two-dimensional metamaterials possessing two or more resonances with strongly disparate radiative lifetimes and quality factors. In analogy to their quantum mechanical counterparts[44], Fano resonances in metasurface emerge as a result of interaction between dark and bright modes, which, according to their naming convention, are weakly and strongly coupled to the radiative continuum, respectively. Provided such modes are engineered, the Fano resonance can be created by making these modes interact in the near field, when the spatial symmetry of the metamolecules is reduced. Moreover, it is also possible to have symmetry reduction that at the same time leads to both i) the formation

of the Fano resonance and ii) chirality of the metasurface. Such reduction of symmetry in general can be achieved by two means, “extrinsic” or “intrinsic”. In the first case, Fano resonances and optical activity emerge due to the oblique incidence of light, leading to the retardation and phase accumulation along the metasurface, which can be rendered to differ for two orthogonal components of electric field giving rise to the polarization conversion[81].

In the more interesting scenario of intrinsic chirality considered here, the optical activity emerges solely from the low spatial symmetry of metamolecules leading to the dissimilar scattering characteristics of circularly left and right polarized waves. However, it is important to mention that in the case of intrinsically chiral metasurfaces it can be rigorously proven that optical activity can only emerge in the form of optical dichroism due to Ohmic loss in constituting materials[81,89]. This fact makes chiral FRMs especially promising for engineering strong optical activity; thanks to significant field enhancement associated with the excitation of a Fano resonance, circular dichroism in these structures can be made gigantic. Nonetheless, no direct experimental evidence of the role of Ohmic loss, or even the manner in which such loss can bring about circular dichroism, exists at the moment. Facilitated by several complimentary techniques, this work for the first time provides experimental evidence on the role of Ohmic loss in inducing circular dichroism.

B.3.2 Experimental Results

As the first step, we fabricated a chiral plasmonic FRM shown in Figure B.3-1(a), which is designed to exhibit strong circular dichroism in the mid-infrared (mid-IR) spectral range[93]. The structure consists of a gold metasurface fabricated by the electron beam lithography on top of a mid-IR transparent CaF_2 substrate, and possesses two periodically arranged resonant elements: i) vertically oriented dipole antennas and ii)

horizontally oriented monopole antennas connected to wires running through the entire metasurface. When considered separately, these elements give rise to two resonances located at wavelengths λ_D and λ_M, where the subscripts stand for dipole and monopole, respectively, and which can be tuned to the same spectral position by adjusting the length of the antennas. However, because of different charge distribution of the two modes, the resonance of the monopole antenna appears to be weakly coupled to the radiative continuum leading to the higher value of its radiative lifetime $\tau_M^R \approx 3\tau_D^R$. To bring in the chirality, aiming to induce the Fano resonance and optical activity at the same time, we reduce the symmetry of the structure by placing the monopole and dipole antennas asymmetrically with respect to each other, as shown in Figure B.3-1(a). In the absence of Ohmic loss such interaction between the vertically polarized dipole and the horizontally polarized monopole results in the formation of the electromagnetically induced transparency-like (EIT-like) response accompanied by the enhanced transmission at the wavelength $\lambda_{\mathrm{EIT}} \approx 9\mu m$ illustrate in Figure B.3-1(d)[94–96]. However, in the case of Ohmic loss present in the metal (Figure B.3-1(e)), EIT regime mixes with that of Electromagnetically Induced Absorption (EIA)[97] leading to enhanced resistive loss and circular dichroism.

Interestingly, although the symmetry reduction endows the structure with chirality and leads to formation of new modes which can discriminate between left circularly polarized (LCP) and right circularly polarized (RCP) waves, it does not result in optical activity of the structure unless Ohmic loss is introduced. Indeed, we confirmed from first principle numerical simulation that, as shown in Figure B.3-1(b), despite the very distinct near field profiles of the lossless structure under RCP and LCP illumination, the far field transmission spectra, shown in Figure B.3-1(d), are identical in the absence of Ohmic

loss. This is in agreement with the theoretical predictions[81,89,93] and confirms that a non-dissipative planar metasurface cannot exhibit optical activity. Introduction of Ohmic loss drastically changes this situation and considerable circular dichroism develops, as illustrated by the far field transmission spectra shown in Figure B.3-1(d). The explanation rests with different field and current distributions induced by the RCP and LCP light: weak optical energy concentration on the vertical dipole antenna for incident RCP wave and high energy concentration on the horizontal monopole antenna for incident LCP wave (shown in Figure B.3-1(b)) leads to uneven Ohmic losses for the two cases giving rise to the difference in transmission $T_{\mathrm{LCP}} \neq T_{\mathrm{RCP}}$ and reflection $R_{\mathrm{LCP}} \neq R_{\mathrm{RCP}}$ (not shown). These observations can also be analytically demonstrated by a simple coupled mode theory involving a pair of lossy dark mode and bright mode, as detailed in the SI.

To understand the origin of the circular dichroism, it is instructive to look into the microscopic origin of the distinct field profiles emerging under LCP and RCP illumination. It appears that when the chirality of the structure is introduced by the symmetry reduction, the phase between previously independent dark and bright modes becomes locked due to their near field interaction. The structure can be optimized such that the horizontal monopole antennas and the vertical dipole antenna, depending on the handedness of the enantiomer, either lead or lag each other by $\sim \pi/2$ at certain frequency near the EIT-like resonance, (while being excited with the same strength). The resultant EIA mode can therefore be considered as circular and is expected to interact differently with light of opposite handedness. Indeed, when excited by the LCP wave, its phase portrait perfectly matches that of the mode for the enantiomer with left handedness, leading to an efficient excitation of the resonance and enhanced absorption. In contrast,

for the case of RCP illumination, disparate phase configuration of the incident wave and of the mode hinders its excitation, leading to weaker absorption of light.

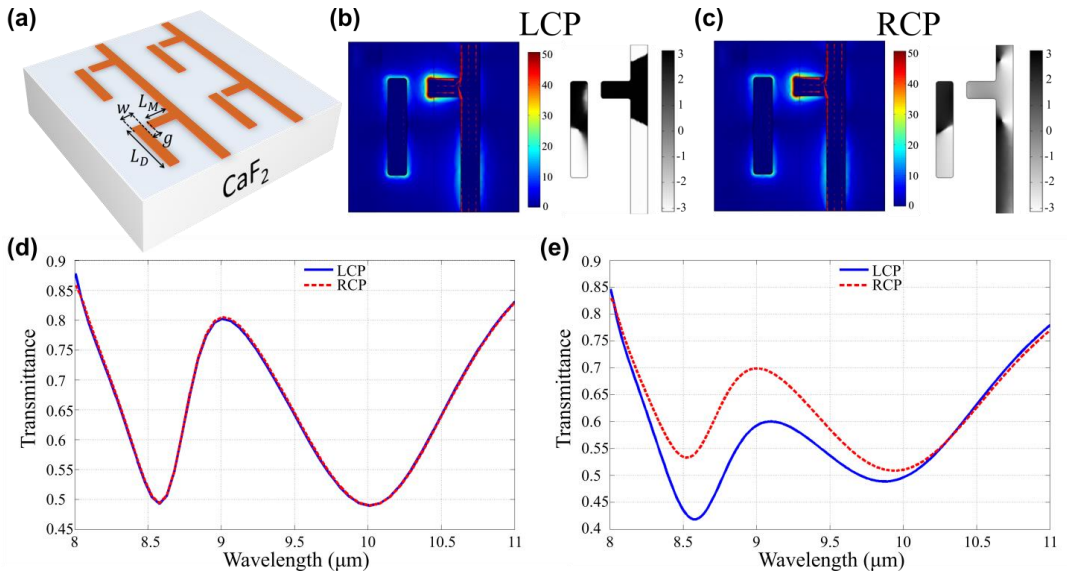

Figure B.3-1: Chiral plasmonic metasurface with electromagnetically induced absorption and circular dichroism. (a) Perspective view of a plasmonic chiral metasurface (2x2 unit cells) on top of CaF2 substrate. (b,c) Left panels: Electric field $|E|$ (shown by color) and surface current distribution (shown by arrows) calculated numerically at the EIA resonance for the cases of normal incidence of LCP (b) and RCP (c) waves. Right panels: corresponding phase portraits (d,e) Transmission spectra of the metasurface for the cases of left circular polarized (blue solid line) and the right circular polarized (red dashed line) excitations without Ohmic loss (d) and with Ohmic loss (e) in metal.

Two samples of enantiomers were fabricated on top of mid-IR transparent (CaF_2) substrate using e-beam lithography technique followed by gold deposition and the lift-off process (see Methods section for details). The nano-topography of the resultant structures obtained with the use of AFM is shown in Figure B.3-2 (a). In the first set of experiments (NSOM) the structure was illuminated through the CaF_2 substrate by circularly polarized wave generated by a tunable CO_2 laser at $\lambda = 9.3\,\mu m$ and passing through a quarter-

wave plate, and the near field 30 nm above the metasurface was measured using the standard NSOM approach[98]. Both amplitude and phase were retrieved and are shown in Figure B.3-2(b) and (c), respectively. This data should be compared with the results of numerical modeling in Figure B.3-1(b), which shows excellent agreement between the theory and experiment. The results of the near-field scan clearly indicate that the near-field distribution strongly depends on the handedness of the enantiomer for given light helicity (LCP incidence). This result thus confirms that optical field concentrated at the metasurface at the EIA resonance is chiral. Indeed, as expected from the discussion above, the vertical and horizontal antennas interfere either constructively or destructively for the two enantiomers under a given circularly polarized illumination, leading to strong enhancement of the near field and increased absorption only for one of the polarizations.

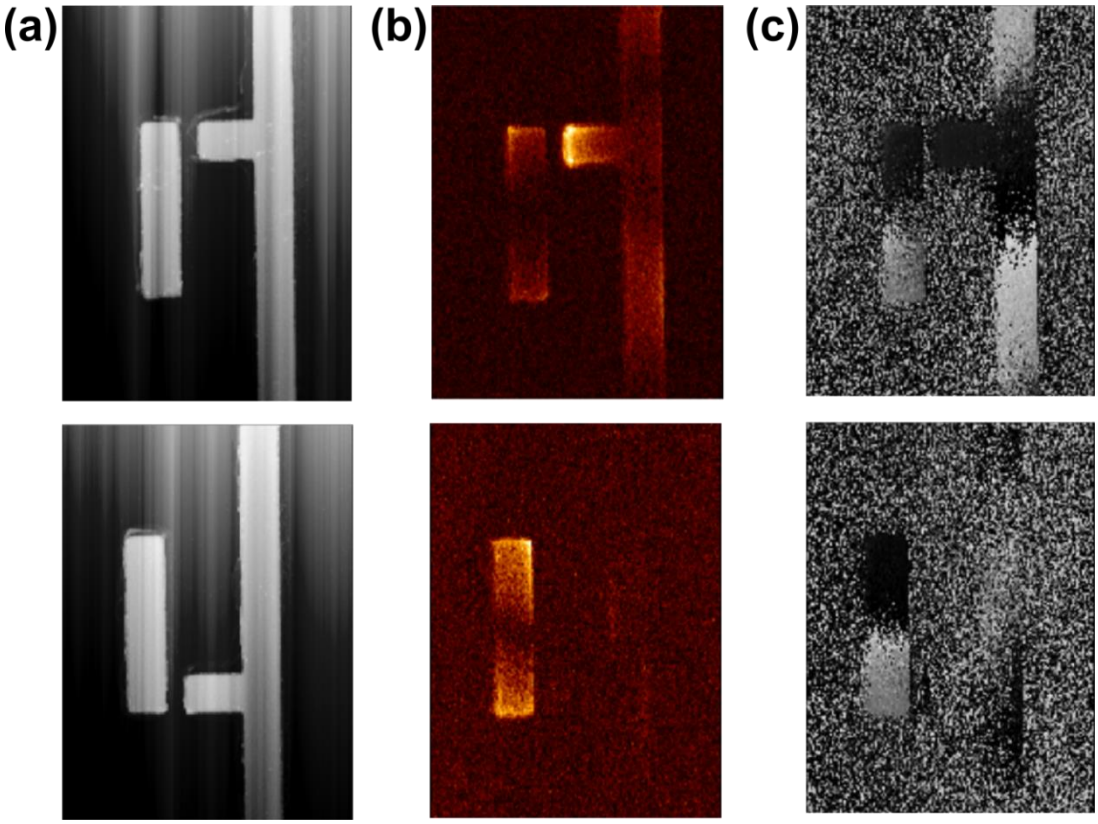

Figure B.3-2: Near-field measurements of the chiral optical field of the metasurface. (a) AFM image of two enantiomers fabricated on top of CaF_2 substrate (b) Field intensity distributions and (c) phase distributions measured by an NSOM for two enantiomers (top and bottom rows, respectively) illuminated by LCP light from a CO_2 laser at $\lambda = 9.3\mu m$.

As the next step, we have directly demonstrated that the circular dichroism in the metasurface originates from the disparate Ohmic loss stemming from distinct near-field distributions. This was accomplished by measuring the thermal expansion on the nanoscale[99,100] for *(i)* the metal constituting the metasurface itself and *(ii)* 100 nm-thick polymer (LOR ®– lift-off resist) coating of FRM. Circularly polarized 200ns pulses at 180 kHz repetition rate from the quantum cascade laser (QCL) were used to induce periodic force caused by the thermal sample expansion on the AFM tip. The force was applied in resonance with the cantilever second bending mode[99,100] and the resultant

cantilever oscillations were recorded[99,100]. The data for RCP and LCP light are shown in Figure B.3-3 for a given enantiomer. In the first set of data corresponding to the case of metal expansion, shown in Figure B.3-3(a), the results clearly indicate that the expansion pattern strongly depends on the handedness of the incident circularly polarized wave. In agreement with the theoretical predictions, the stronger field concentration and heating occurs for the LCP incidence, leading to a stronger absorption and a lower transmission in the far field (shown in Figure B.3-3 (c)).While this data does unambiguously proves that optical activity of the structure originates in the Ohmic losses in the metal, the maximal thermal expansion occurs in the regions with maximal values of currents in the metal rather than fields around it. To further prove that these currents leading to dichroic response of FRM are induced by the fields having profiles identical to those measured by NSOM technique, the second set of measurements was performed. In these measurements the structure was coated by a 100 nm-thick LOR® polymer capable of absorbing light at the wavelength of Fano resonance. Due to the fact that absorption in such lossy polymer takes place in the regions of maximal field concentration, this allows us to map the field distribution in the structure by measuring the thermal expansion of the polymer by an AFM tip. As can be seen from the measurements results presented in Figure B.3-3(b), the strongest expansion of the polymer takes place near the tips of the antennas, as opposed to the case of metal expansion. In agreement with both numerical results and the experimental NSOM data, the field distribution differs significantly for LCP and RCP incident waves. One can again notice that stronger polymer expansion occurs for the LCP incident light and the field concentration takes place near the tip of horizontal monopole antenna. At the same time, stronger amplitude of the AFM cantilever oscillations (indicated by the color-bars) confirms higher absorption rate of

LCP light leading to the circular dichroism and disparate far-field transmission spectra shown in Figure B.3-3(c).

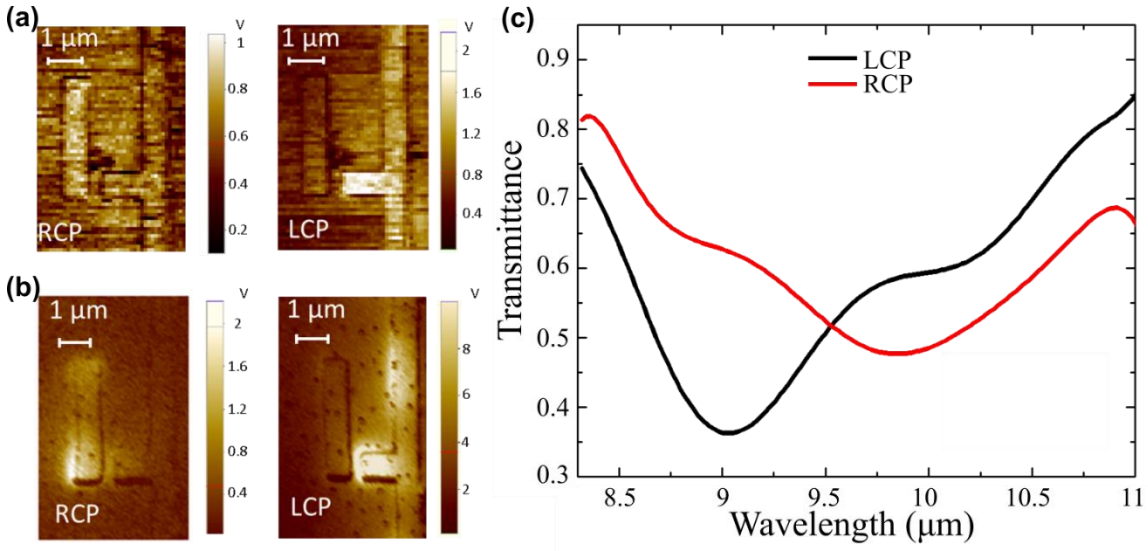

Figure B.3-3: AFM measurements of circularly dichroic thermal expansion of the metasurface that serves as a proxy for Ohmic loss and field distribution. Uneven thermal expansion of metal constituting FRM (a) and LOR polymer coating (b) at the wavelength of EIA. (c) Experimental far-field transmission for the enantiomers revealing the chiral dichroism in transmission caused by Ohmic loss due the excitation of Fano-resonance and EIA.

B.3.3 Conclusion and Outlook

In conclusion, by using three distinct experimental techniques, including two near-field and one far-field, we demonstrated that optical activity in Fano-resonant plasmonic metasurfaces possessing a planar chirality appears solely from circularly dichroism that emerges from the near-field Fano interference. It was experimentally proven by mapping fields and absorption rates on a subwavelength scale that the planar chirality results in concentration of chiral optical energy and promoting uneven absorption of light of left and right helicities. The present discovery envisions novel

avenues for the development of innovative detectors measuring the degree of circular polarization in mid-IR and visible domains, as well as ultrasensitive sensors capable resolving chirality of biomolecules.

SECTION C : BIOSENSING

In this section I will discuss the usage of metasurfaces for biosensing. Two specific applications will be discussed— detecting protein monolayer, and distinguishing cell types. First we shall discuss the use of FRAMM for the detection and characterization of protein monolayer. We shall then proceed to discuss the strategies and methods investigated for isolation and identification of cancer cells in patient blood sample in the last two chapters. I will conclude with ideas for future work.

Chapter C.1: Why Metamaterials are Good for Biosensing

Engineered optical metamaterials present a unique platform for biosensing applications owing to their ability to confine light to nanoscale regions and to their spectral selectivity. Infrared plasmonic metamaterials are especially attractive because their resonant response can be accurately tuned to that of the vibrational modes of the target bio-molecules. In this chapter we use the infrared plasmonic surface, Fano-resonant asymmetric metamaterial (FRAMM, discussed in detail in Chapter B.2) exhibiting sharp resonances caused by the interference between sub-radiant and super-radiant plasmonic resonances. Owing to metamaterial's asymmetry, the frequency of the sub-radiant resonance can be precisely determined and matched to the molecule's vibrational fingerprints. A multi-pixel array of FRAMMs is used as a platform for multi-spectral biosensing of nanometer-scale monolayers of recognition proteins and their surface orientation, as well as for detecting chemical binding of target antibodies to recognition proteins.

C.1.1 FRAMM FOR PROTEIN SENSING

Here we introduce a novel *structure-resolving label-free biosensing* technique based on plasmonic Fano-Resonant Asymmetric Metamaterials (FRAMMs) that can simultaneously probe structural and binding characteristics of biomolecular interactions by using the full information content of the bio-molecules' frequency-dependent infrared response.

While the concept of tuning metamaterial resonances to specific vibrational lines of a bio-molecule is straightforward[67], its actual implementation is complicated by dense spectral spacing of infrared-active vibrations. For example, selectively tuning resonant metamaterials to commonly used amide vibrations of the protein backbone (Amide-I at $\omega_I = 1620 - 1680 cm^{-1}$ and Amide-II at $\omega_{II} = 1510 - 1580 cm^{-1}$) requires the structures' quality factors $q \sim 10$. Even narrower resonances may be required to resolve the secondary protein structure. Such sharp resonant lines are difficult to obtain with most plasmonic metamaterials despite relatively low Ohmic losses at infrared frequencies[9,67]. Narrow linewidth is also requisite for obtaining large field enhancements over the surface of a planar plasmonic meta-molecule. For example, a half-wave antenna provides neither strong field enhancement nor spectrally-narrow response. By arranging meta-molecules into periodic arrays, it is possible to suppress radiative decay and boost field enhancement due to the formation of collective high quality resonances[83]. The drawback of such coherent metamaterials[9,101] is their reliance on long-range interactions between unit cells, making their performance sensitive to fabrication imperfections and angular spread of the IR beam.

Another recently emerged approach to achieving sharp spectral response and high field enhancement is based on Fano resonances[44,46–48,95,102–104]. The Fano resonance

approach relies on local resonances of the meta-molecules and therefore is free of the disadvantages of coherent metamaterials. Fano resonances originate from the interference between two electromagnetic eigenmodes, referred to as "super-radiant" and "sub-radiant"[103,104], of a multi-resonant meta-molecule. Such structures possessing high quality factors[46,49,105] could be used for quantitative biosensing, but suffer from lack of molecular specificity because of the reliance on the frequency-independent protein refractive index. The FRAMM-based platform introduced below enables quantitative biosensing and fingerprinting of nm-scale multi-molecular nano-assemblies, and potentially allows investigation of the underlying mechanisms of a wide class of bio-molecular interactions that are not accessible with current detection techniques. By tuning individual array elements toward (away from) protein's vibrational resonances, we investigate, respectively, structural/spectroscopic and binding properties of nm-scale protein monolayers. The latter enable, for example, accurate determination of the overall monolayer thickness, while the former provide highly specific information about the protein's orientation or conformational state. The asymmetry of the constitutive meta-molecules of the FRAMM enables precise experimental determination of the spectral positions of Fano resonances, while the resonant field enhancement dramatically boosts transduction of the protein's structural and binding properties into an infrared signal. We demonstrate the biosensing and fingerprinting capabilities of the FRAMM-based multi-pixel substrate by testing it on a well-defined ultra-thin multi-protein layer (a target protein monolayer deposited on top of a recognition monolayer). Specifically, we demonstrate: (i) vibrational fingerprinting and measurement of the thickness h_1 of the recognition protein's (Protein A/G); (ii) detection of antibody (anti-mouse IgG from goat) binding to protein-immobilized surfaces, and determination of the thickness h_2 of the

antibody monolayer using h_1 as a molecular yardstick; (iii) determination of spatial orientation of the proteins with respect to the metal surface normal. The last information is vital in determining their functional availability for bio-targeting[68,106,107]. The FRAMM array also opens exciting possibilities for rapid biosensing when standard techniques of parallel acquisition of multiple infrared spectra by focal plane array (FPA) detectors[108] are applied to multi-pixel FRAMM-based functionalized substrates. Potentially this platform will allow monitoring of a wide class of biomolecular interactions with characteristics that are not accessible with current detection techniques.

C.1.2 FRAMM SPECTROSCOPY FOR DISTINGUISHING CELLS

For diagnostic and research purposes it is very useful to be able to distinguish different types of cells. Cell diagnosis forms a critical part of a clinical treatment plan and in most cases an early stage accurate diagnosis improves significantly the efficacy and potential of treatment. However, a significant portion of diagnosis is limited by subjective interpretation by the clinical physician handling the patients sample (for eg. a biopsy sample). In this respect, Fourier Transform Infrared Spectroscopy (FTIR) is an useful tool to interrogate cells[109–113] for their molecular composition because many of the bio-molecules have fingerprint resonance in the infrared region (see Table C.4-2 or Bellisola et al.[109], Table 1). FTIR techniques allow acquisition of information about molecular composition of cells and other biological matter and makes the analysis more objective. It also has the potential of reducing the amount of sample volume necessary for diagnosis—down to, potentially, a single malignant cell.

Advances in the usage of FTIR have led to its use for cancer detection[113–117] incorporated in to various techniques such as ATR-FTIR, fiber-optics based detection. It

has been used for many cell lines [118], including blood cells[119,120], cervix[121], breast[115,122,123], prostrate[124], lung[113] colon[125], skin[114,115,126] and other cell types— healthy or cancerous.

A biomarker for a cell type is a measurable structural of functional attribute that is different between cell types[109]. Molecular composition counts among such markers, and it is this that is targeted by FTIR based methods. Such distinctions arise out of different functional requirements and divergent genomic expressions in the body of the same organism or person. Advances in FTIR techniques and computational ability have resulted in the production of an ever-increasing amount of data that may be used for such finger-printing applications. The demand is more on the data analysis approach[111,127] to identify the useful parts of data acquired rather than the computational load involved.

Vibrational modes of molecules in the IR are typically stretch modes (ν_s— symmetric stretching mode, or ν_{as}— asymmetric stretching mode), and bending modes (δ_s— symmetric bending and δ_{as}— asymmetric bending). There are other possible vibrations like twisting (γ_t), wagging (γ_w) etc. A molecule with N atoms has 3N-5 possible modes of vibrations. For a typical amide group (15 atoms), there are roughly 40 vibrational lines[128]. A protein with 1000 amino acid chain has nearly 45,000 vibrational lines! Many of these lines overlap, and are apparent in spectra as vibrational band rather than a vibrational line.

Additionally, water molecule has 3 major lines in the IR region, the ν_s at $1650\ cm^{-1}$, the ν_{as} at $3500\ cm^{-1}$, and δ at $600\ cm^{-1}$. The ν_s mode is extremely close to the amide I mode, and this makes it difficult to deconvolute the amide I and $\nu_s^{H_2O}$ without a-priory knowledge of water-to-amide group ratio.

While FTIR based fingerprinting methods hold enormous promise for identifying cell types, there are a few challenges that needs to be overcome. The most persistent problem has been taking data in vivo. This is due to the high absorption of water which makes it opaque in a certain IR spectral window (close to $1650\ cm^{-1}$). That water is opaque to infrared makes it harder to obtain spectrographs of live cells. In this work, we address this problem by taking data in a geometry where infrared light does not pass through water. Rather, the data is collected in reflection geometry so that evanescent waves collect information in the spectrometer set-up.

For the rest of this section (Section C), I will focus on planer metamaterials, or metasurfaces, which were discussed in detail in the previous section. In Chapter C.4 we discuss distinguishing different cell types in 'dry' condition. The term `dry sensing' needs to be clarified. These experiments are called `dry' to contrast them with the experiments in Appendix D.2— in vivo sensing with the cells immersed in Phosphate-buffered saline (PBS) solution (`wet sensing'). In `dry' experiments, the cells are placed on a dry sensor. The cells themselves are live and therefore have water in the cytoplasm. Also, during the experiment there is a thin layer of water that forms on the sensor surface.

C.1.3 CANCER PROGRESSION

The progression of cancer is not fully understood, and is the subject of a large number of ongoing studies[71,72,129,130]. However, it has several recognized stages. The first stage is the growth of a tumor made of mutated (cancerous) cells. Cancer at this stage is often not recognized as a threat by immune system, which is targeted at foreign bodies.

In the next stage, cancerous cells from tumor enter into the bloodstream. These circulating tumor cells (CTCs) spread through the patient body. The CTCs were theoretically predicted to be a possible signature to detect cancer by Liberti et al.[131],

because there were enough CTCs to be statistically detectable. One great advantage of detecting CTCs is that it is not necessarily specific to an organ. Many forms of cancer detection (e.g. biopsy) require the medical practitioner to form a hypothesis as to whether cancer may have formed and where. Checking for CTCs in blood, on the other hand may be used for both cancer screening and diagnostics. This is the end goal of this research- to be able to isolate and identify CTCs in patient blood stream.

In the third stage of the disease, the CTCs invade healthy tissue and form new tumors. This process is called metastasis. Once the metastasis process starts, the treatment options for cancer become much more difficult and the survival rate drops significantly. This process, however, does not usually begin as soon as CTCs begin circulating in bloodstream, because not all invasive CTCs succeed in metastasizing, allowing for patient recovery in case metastasis has not begun.

The process of invasion has been discussed in some detail by Paterlini-Brechot et al.[132]. It is known[130,132,133] that $\sim 1/40$ CTCs result in micrometastasis, and only about 0.01% proliferate into macrometastasis. Micrometastasis is defined[134] as a tumor that is smaller than $0.2\ cm$ in any direction. Macrometastasis is a tumor that is larger than $0.2\ cm$ in at least one direction. The invasion itself, however, is believed to onset as early as the CTCs are in circulation— even though most invasive CTCs do not succeed in metastasizing. The low success rate of CTCs resulting in metastasis allows patient to be cured if the cancer is found early enough that the malignant tumor may be removed before metastasis has begun in earnest.

As a result, detection of CTCs has become a matter of intense research (for a review see ref. [132]). The challenge is that any method for detection of CTCs has to be both very selective and sensitive. Proportion of CTCs to normal blood cells can range

from 10^{-6} to 10^{-9}. Which can mean that there is ~ 1 cell in $10\ ml$ of blood. A recent study showed that survival rate of patients with metastatic breast cancer go down significantly when there is more than 5 cells in $7.5\ ml$ of blood[135]. Any detection strategy has to incorporate a highly selective yet accurate method of separating the cancerous cells from blood sample. Losing just a few cells of CTCs in the separation process may result in a false negative diagnosis. Specificity is also important because a false positive could subject a patient to unnecessary treatment.

C.1.4 CTC Detection Strategies

As mentioned before, CTC detection is challenging[131,134]. In $10\ ml$ of blood there are only a few (~ 1) CTCs in 10^8 leukocytes (white blood cells, WBC), and about 50×10^9 erythrocytes (also known as red blood cell or RBC). Separation of the erythrocytes is relatively easy[132,136]. Separating the CTCs from the leukocytes can be challenging.

Approaches to separation and detection of CTCs may be classified broadly into two categories[132]:

1. Indirect methods: use physical or chemical characteristics of cancerous cells.
    a. Targeting a specific antibody/antigen expression. One of the methods that utilizes this strategy involves[131] magnetic beads coated with antibody specific to types of cancerous cells. A disadvantage with this method is that there is no antibody that is 100% tissue/tumor specific. That is, there is no universal marker for cancer. This limits such techniques to one or more specific type(s) of cancer. Antibodies are expensive— any cost effective method has to minimize the use of antibody.

b. Targeting to exploit different physical characteristics of CTCs— size, deformation, dielectric properties. For example, the fact that certain cancerous cells (CTCs) are bigger than leukocytes may be used for their separation[137,138]. Dielectrophoresis (DEP) is another technique[139–143] which distinguishes cells by their dielectric properties.

2. Direct methods: targeting a cancerous gene expression. For example, *reverse transcription polymerase chain reaction* (RT-PCR)[144] uses polymerase chain reaction to detect RNA expression. RT-PCR looks for specific gene mutations in DNA of the cells in blood. The steps are as follows: collection of blood sample, enrichment of possible CTCs (cells with nucleus in blood), isolation of cells, extraction of RNA, synthesis of complementary DNA, followed by marker gene amplification.

   This method is quite powerful when the specific gene mutation to look for is known. If the target gene mutation is present, then it can be identified through the corresponding RNA-s.

   The underlying assumption is that the marker RNA is exclusive to cancerous DNA. This may not always be true, increasing the chances of a false positive. Also, this technique is not very useful for general cancer screening because cancer results from many possible gene mutations. It is not possible to look for each and every marker without a full DNA sequencing which is expensive and time consuming. Also, in the process of RT-PCA, the sample cells are destroyed, which makes counting cells impossible, and repeating tests difficult. A CTC count helps quantify the progression of the disease, and form a hypothesis about the probability of metastasis.

With the advent of plasmonic metasurfaces, new uses for plasmonic material have been proposed— including the use of plasmonic nanoparticles for detection of cancer [122,145] and targeted photothermal therapy of cancer[146–149]. Plasmonic sensors have been used as biosensors[8,9,133] for disease detection. Here, we discuss the use of the plasmonic metasurfaces discussed in Chapter B.2 as a biosensor for cancer cell detection. This structure was chosen because of the relatively high quality factor of the structure, ease of fabrication, and our prior experience with the sensor as biosensor[8].

We used a combination of two indirect methods in our research— we targeted both molecular expression (with antibody) and physical characteristics (with DEP) to isolate a cancerous cell. On top of this, we perform spectroscopic analysis to confirm diagnosis. The combination of these three different methods is used to minimize the risk of a false positive which creates a huge emotional and financial cost for the patient. On the other hand, a false negative puts the patient life at risk, which is why the combination of cell concentration (to first remove the RBCs), microfluidic, and DEP methods will be optimized to minimize the risk of CTC loss. Two chapters (Chapter C.4 and Appendix D.2) of this dissertation focus on cell spectroscopy.

Chapter C.2: FRAMM for Protein Sensing[2]

C.2.1 Theoretical Background of the FRAMM-Based Biosensing

An example of an asymmetric metamaterial comprised of two plasmonic antennas along the y-axis and a perpendicular antenna coupler attached to one of them is shown in Figure C.2-1. Near-field interaction between the two antennas results in parallel (electric dipole) and anti-parallel (quadrupole/magnetic dipole) current excitations corresponding to super- and sub-radiant modes, as indicated in Figure C.2-1(a). If the two parallel antennas are identical, the sub-radiant mode is completely dark and decoupled from the normally incident light. The small horizontal coupler makes the meta-molecule asymmetric by breaking all spatial inversion/reflection symmetries in the plane of the structure. Such symmetry breaking not only directly couples the sub-radiant and super-radiant modes (thereby enabling Fano interference for the y-polarized incident light), but also couples the sub-radiant mode to the perpendicular (x) polarization. The resonant frequencies of the sub- and super-radiant modes are primarily determined by the length $L_1$of the two parallel antennas, while the length and position of the short horizontal segment determine the degree of symmetry breaking. Solid lines in Figure C.2-1(c) show the reflection spectra from one of the FRAMM samples for both y- and x-polarized incidence. The y-polarized reflection exhibits the typical Fano (i.e. asymmetric non-Lorentzian) resonance shape: it peaks at the frequency $\omega_D \approx 2000cm^{-1}$ of the dipole

[2] The work in this chapter is based on a collaboration with coauthors in— Chihhui Wu , Alexander B. Khanikaev, Ronen Adato, Nihal Arju, Ahmet Ali Yanik, Hatice Altug and Gennady Shvets, "Fano-resonant asymmetric metamaterials for ultrasensitive spectroscopy and identification of molecular monolayers," Nature Materials, 11 (69). Wu performed the simulations and contributed the most to data analysis. Wu, Khanikaev, Adato and Arju were involved in the data analysis. Adato, Arju and Yanik were involved in collecting data. Arju fabricated the structure and performed some simulations. Prof. Altug and Prof. Shvets supervised and guided the project. Prof. Shvets conceived the work.

resonance, and experiences a rapid dip-to-peak variation as the frequency decreases from $\omega_{dip} \approx 1600cm^{-1}$ to $\omega_{peak} \approx 1450cm^{-1}$. Such variation indicates the presence of a sub-radiant resonance in the frequency range $\omega_{dip} < \omega_Q < \omega_{peak}$, but does not exactly identify the frequency ω_Q which must be determined by other means.

On the other hand, the x-polarized spectrum in Figure C.2-1(c) shows a nearly Lorenzian lineshape peaking at ω_Q. This is because the FRAMM allows the sub-radiant mode to be excited alone with x-polarized light, in which case no interference with the y-polarized super-radiant mode occurs. Earlier work on Fano interferences[103,104,150] relied on numerical simulations of the charge distribution inside the plasmonic structures for identifying the exact spectral position of the sub-radiant resonances. Asymmetric structures enable direct experimental identification of the sub-radiant modes. Using orthogonally-polarized spectroscopy (E field parallel to the x-direction), the Lorenzian reflectivity peak accurately identifies the spectral location of the sub-radiant mode.

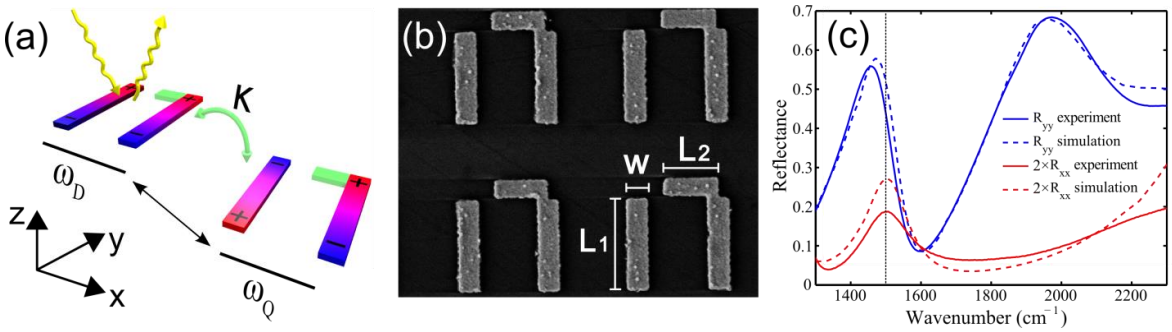

Figure C.2-1: Geometry and electromagnetic properties of a Fano-resonant asymmetric metamaterial (FRAMM). (a) Schematic of sub-radiant (Q) and supper-radiant (D) modes of the FRAMM coupled to incident infrared light. (b) SEM image of a typical fabricated FRAMM and geometric sizes: L_1=1.8μm, L_2=0.9μm, w=0.36μm, metal thickness=70 nm, and periodicities in x- and y-direction are P_x=2.7μm and P_y=3.15 μm. (c) Experimental (solid) and theoretical (dashed: COMSOL simulations) polarized reflectivity spectra: Fano (Lorentzian) lineshaps for vertical (horizontal) polarizations.

Optical response of FRAMMs can be described by temporal coupled mode theory (TCMT)[82], modeling two weakly-coupled super-radiant (D) and sub-radiant (Q) modes with the eigenfrequencies ω_D and $\omega_Q = \omega_D - \delta$, respectively. Using a small number of fitting parameters (see Supplements A, B), TCMT predicts polarized reflectance spectra and field enhancements well matched to the experimental data and finite element simulations, and gives a clear physical understanding of the FRAMMs' response. The 2-by-2 reflection tensor $r_{\gamma\beta}$ (relating the reflected and incident electric fields according to $E_\gamma^{(r)} = r_{\gamma\beta}E_\beta^{(i)}$ with $\gamma, \beta = x$ or y) predicted by TCMT for a bare FRAMM is estimated as:

$$r_{\gamma\beta}^{(bare)} \approx \frac{\alpha_{Q\gamma}\alpha_{Q\beta}(\omega)}{j(\omega-\omega_Q)+\frac{1}{\tau_Q}} + \frac{\alpha_{D\gamma}\alpha_{D\beta}}{j(\omega-\omega_D)+\frac{1}{\tau_D}} \qquad \text{C.2-1}$$

where $\alpha_{Dy}, \alpha_{Qy} \approx (\kappa/\delta)\alpha_{Dy}$ and $\alpha_{Qx} \sim \alpha_{Dx} \ll \alpha_{Dy}$ are the coupling efficiencies of the super-radiant and sub-radiant resonances to the two light polarizations, $\kappa(L_2) \ll \delta$

is the weak near-field coupling rate between the two resonances due to the short horizontal antenna, and $\tau_D \sim 1/|\alpha_{Dy}|^2$, $\tau_Q \sim (\delta^2/\kappa^2)\tau_D$ are the lifetimes of the corresponding eigenmodes (details in Supplement B). According to equation C.2-1, polarized reflectivities $R_{\gamma\gamma}(\omega) = |r_{\gamma\gamma}|^2$ have either Fano or Lorenzian lineshapes because of disparate lifetimes of the modes and their different coupling efficiencies to y- and x-polarizations.

According to TCMT, the difference in lifetimes and polarization-dependent radiative coupling efficiencies determines the near-field enhancement at the FRAMM's surface that is crucial for plasmon-enhanced sensing techniques[9,35,67]. Specifically, it can be shown (see Appendix D.4) that field intensities corresponding to y-polarized excitation of sub-radiant (Fano) and super-radiant modes scale with their lifetimes as: $\left(\frac{|E_{Qy}/\,E_{inc}|}{|E_{Dy}/\,E_{inc}|}\right)^2 = \frac{\tau_Q}{\tau_D} = \frac{q_Q}{q_D}$, where $q_{Q(D)}$ are the quality factors ($q_Q \approx 8.4, q_D \approx 2.7$ for the structures in Figure C.2-1). Excitation of the Fano resonance using x-polarized radiation yields a much smaller field enhancement: $\left(\frac{|E_{Qy}/\,E_{inc}|}{|E_{Dy}/\,E_{inc}|}\right)^2 = \left(|\alpha_{Qy}/\alpha_{Qx}|\right)^2$. These analytic predictions of TCMT were confirmed using COMSOL simulations shown in Figure C.2-2(a,b), where the near-field enhancement around the FRAMM is computed for the three possibilities of exciting FRAMM's resonances: (i/iii) narrow-band Fano resonance excited by *y*/*x*-polarized radiation, and (ii) broad-band super-radiant resonance excited by *y*-polarized radiation. Only the Case (i) corresponding to Fano interference leads to large spectrally-selective enhancement of the near field and holds promise for sensing applications as demonstrated below.

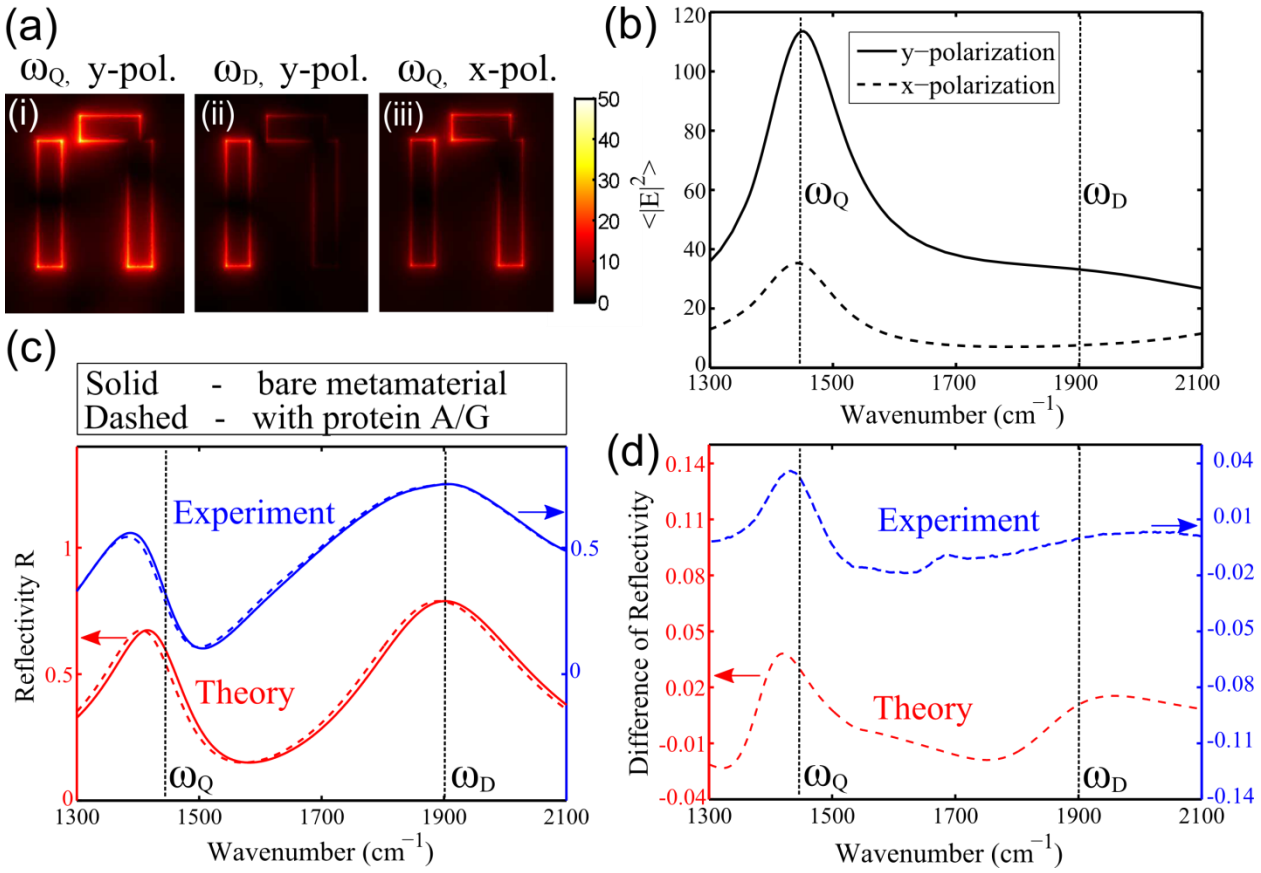

Figure C.2-2: Near fields of the FRAMMs for different frequencies and incident polarizations and their manifestations in IR reflectance spectroscopy. (a) Field profiles and enhancement of $|E|$ (color bar). (b) Enhancement of $|E|^2$ averaged over a hypothetical 10nm thick monolayer is highest for Fano resonance (i). (c) Analytic and measured reflectivity from FRAMMs before (solid lines) and after (dashed lines) functionalization with a 3nm thick Protein A/G monolayer. (d) Analytic and experimental reflectivity difference $\Delta R(\omega)$ caused by the Protein A/G monolayer.

Detection and characterization of protein monolayers with FRAMMs are accomplished by measuring difference-reflectivity, $\Delta R(\omega) = |r_{yy}^{(bare)}(\omega)|^2 - |r_{yy}^{(func)}(\omega)|^2$, between the bare and functionalized substrates. Presence of protein monolayers of thickness h changes the dielectric environment of the FRAMM and results in frequency shifts $\Delta\omega_{Q(D)}$ given by[151]:

$$\Delta\omega_{Q(D)}/\omega_{Q(D)} = -\frac{1}{2}\frac{\int_0^h \boldsymbol{E}_{Q(D)}(\boldsymbol{r}) \cdot (\hat{\epsilon} - 1) \cdot \boldsymbol{E}_{Q(D)}(\boldsymbol{r}) d\boldsymbol{r}}{\int_0^\infty \left|E_{Q(D)}(\boldsymbol{r})\right|^2 d\boldsymbol{r}}, \quad \text{C.2-2}$$

where $\boldsymbol{E}_{Q(D)}(\boldsymbol{r})$ is the near field of the $Q(D)$ mode, and $\hat{\epsilon}$ is the permittivity tensor of the protein. The complex-valued $\Delta\omega_{Q(D)}$ affects both the spectral position (index-induced shift) and lifetime (surface-enhanced absorption) of the FRAMM's resonances. The modified reflectivity tensor, $r_{\gamma\beta}^{(func)}$, of the functionalized FRAMM is obtained from C.2-1 by substituting $\omega_{Q(D)} \to \omega_{Q(D)} + \Delta\omega_{Q(D)}$, resulting in the change, $\Delta R(\omega)$, as shown in Figure C.2-2(c,d).

Because the electric field is predominantly normal to the metal surface, the frequency shift scales with h according to $\Delta\omega_{Q(D)}/\omega_{Q(D)} \propto (\epsilon_n - 1)h/l_{Q(D)}$. Here we assume that the modes' surface-averaged localization length $l_{Q(D)} \gg h$. According to numerical simulations, $l_Q \sim 50\, nm$ for the sub-radiant mode. The direction-dependent permittivity, $\epsilon_n \equiv \boldsymbol{n} \cdot \hat{\epsilon} \cdot \boldsymbol{n}$, is assumed to be approximated by a multi-resonant series:

$$\epsilon_n(\omega) = n_\infty^2 + \sum_m \frac{A_m < cos^2\,\theta_m >}{(\omega - \omega_m) - j\gamma_m} \quad \text{C.2-3}$$

where the summation is over all infrared-active vibrational modes with natural frequencies ω_m, damping rates $\gamma_m \equiv 1/\tau_m$, and dipole strengths A_m, and $n_\infty \equiv \epsilon_\infty^{1/2} \approx 1.55$ is the non-specific refractive index. The surface selection rule[152] rescales the dipole strength: $\tilde{A}_m \equiv A_m < \cos^2\theta_m >$ according to the averaged orientation of the m'th vibration mode with respect to the metal surface normal $\boldsymbol{n}$. S*tructure-resolving biosensing* is accomplished by an array of FRAMM pixels that are spectrally-tuned either *to* various vibrational resonances (spectroscopic characterization of conformational states and orientations of bio-molecules) or *away* from them (determination of the nano-layer thickness h using the non-specific n_∞).

C.2.2 APPLICATIONS OF FRAMMS TO FINGERPRINTING AND CHARACTERIZATION OF PROTEIN MONOLAYERS

Several arrays of gold FRAMMs were fabricated on a quartz substrate, as shown in Figure C.2-1(b), with their reflectivity spectra measured using a Fourier-transform infrared (FTIR) microscope (see Methods). $150\,\mu m \times 150\,\mu m$ FRAMM pixels were designed to resonate at different frequencies $1340cm^{-1} < \omega_Q < 1860cm^{-1}$ by uniformly scaling their dimensions. Measured reflectivity spectra from a typical pixel shown in Figure C.2-1(c) are used to determine the Fano resonance frequency ω_Q from the peak of $R_{xx}(\omega)$, and are accurately fitted with numerical (COMSOL) and analytic (TCMT) calculations. The structure-specific biosensing was demonstrated by immobilizing two protein nano-layers on the FRAMM's surface: (a) monolayer of a single recognition protein A/G of thickness h_1 , and (b) multi-protein bi-layer of thickness $H = h_1 + h_2$consisting of a monolayer of goat antibody IgG of thickness h_2 on top of the protein A/G as shown schematically in Figure C.2-3(b). Optical transduction of protein binding to gold is done by measuring normalized differential reflectivity $D^{(\omega_Q)}(\omega) \equiv \Delta R^{(\omega_Q)}(\omega)/R_Q^{(\omega_Q)}(\omega = \omega_Q)$ for each FRAMM pixel uniquely labeled by its ω_Q.

To illustrate the concept of structure-specific biosensing, we note that the spectral maximum $D^{(\omega_Q)} \equiv D^{(\omega_Q)}(\omega = \omega_Q)$ depends on the frequencies' mismatch between ω_Q and those (ω_m's) of the protein vibrational modes (e.g., Amide-I/II), as well as the specific (and *a priori* unknown) properties of the modes: their dipole strengths, lifetimes, and bond orientation. The strongest interaction between the proteins and the FRAMMs corresponding to the largest $D^{(\omega_Q)}$ occurs when the frequency/lifetime (ω_Q, τ_Q) of the FRAMM coincides with those (ω_m, τ_m) of one of the vibrational modes of the molecules[153]. Although the lifetime matching is beyond the scope of this work, frequency

matching of $\omega_Q$to ω_I(green line) yields the largest $\Delta R/R_Q$ among the three FRAMMs shown in Figure C.2-3(a,c). However, if the Fano resonance is tuned *away* from the Amide vibrations, i.e. $|\omega_Q - \omega_m| \gg 1/\tau_Q$, then the value of $D^{(\omega_Q)} \sim h(\epsilon_\infty - 1)$ yields the non-specific protein's thickness h. By comparing theoretically and experimentally obtained difference spectra, we found that $h_1 \approx 2.7nm$, which is in good agreement with $h_1 \approx 2.8nm$ obtained by ellipsometry. Protein A/G monolayer changes the reflectivity by easily detectable $\Delta R^{(mono)}(\omega = \omega_Q) = 4\%$ (see Figure C.2-2(d) and blue/red spectra in Figs.3a,c), indicating that molecular monolayer thickness can be reliably measured with nm-scale accuracy.

Similarly, binding of the IgG antibody monolayer to the protein-immobilized FRAMMs is detected by measuring the $\Delta R^{(bi)}(\omega)$ (solid lines) spectra of the resulting protein bi-layer with the thickness $H^{(el)} = h_1 + h_2 \approx 7.9nm$ (ellipsometric value) and comparing it with $\Delta R^{(mono)}(\omega)$ (dashed lines) in Figure C.2-3 (c). Larger overall thickness of the bi-layer clearly manifests in the peak reflectivity ratios $T(\omega_Q) \equiv \frac{\Delta R_{max}^{(bi)}}{\Delta R_{max}^{(mono)}} > 1$ for all three FRAMMs in Figure C.2-3(c). The expected $T(\omega_Q) \approx H/h_1$ for the FRAMMs satisfying $|\omega_Q - \omega_m| \gg 1/\tau_Q$ provides an accurate measurement of the thickness h_2 of the IgG monolayer by using h_1 as a *molecular yardstick*. By comparing the experimental data to the analytical model, $T(\omega_Q) \approx 2.9$ was estimated, or $H \approx 7.8nm$ and $h_2 \approx 5.1nm$. For antibodies, h_2 provides indirect information[106,154] about their orientation on the surface and the availability of antigen binding. Specifically, h_2 is a lower bound of the actual height of the IgG layer (which has a high void fraction due to its multi-fragmented structure). Because the height of the lying-on IgG is only about 4 nm, we conclude that the IgGs are mostly end-on oriented.

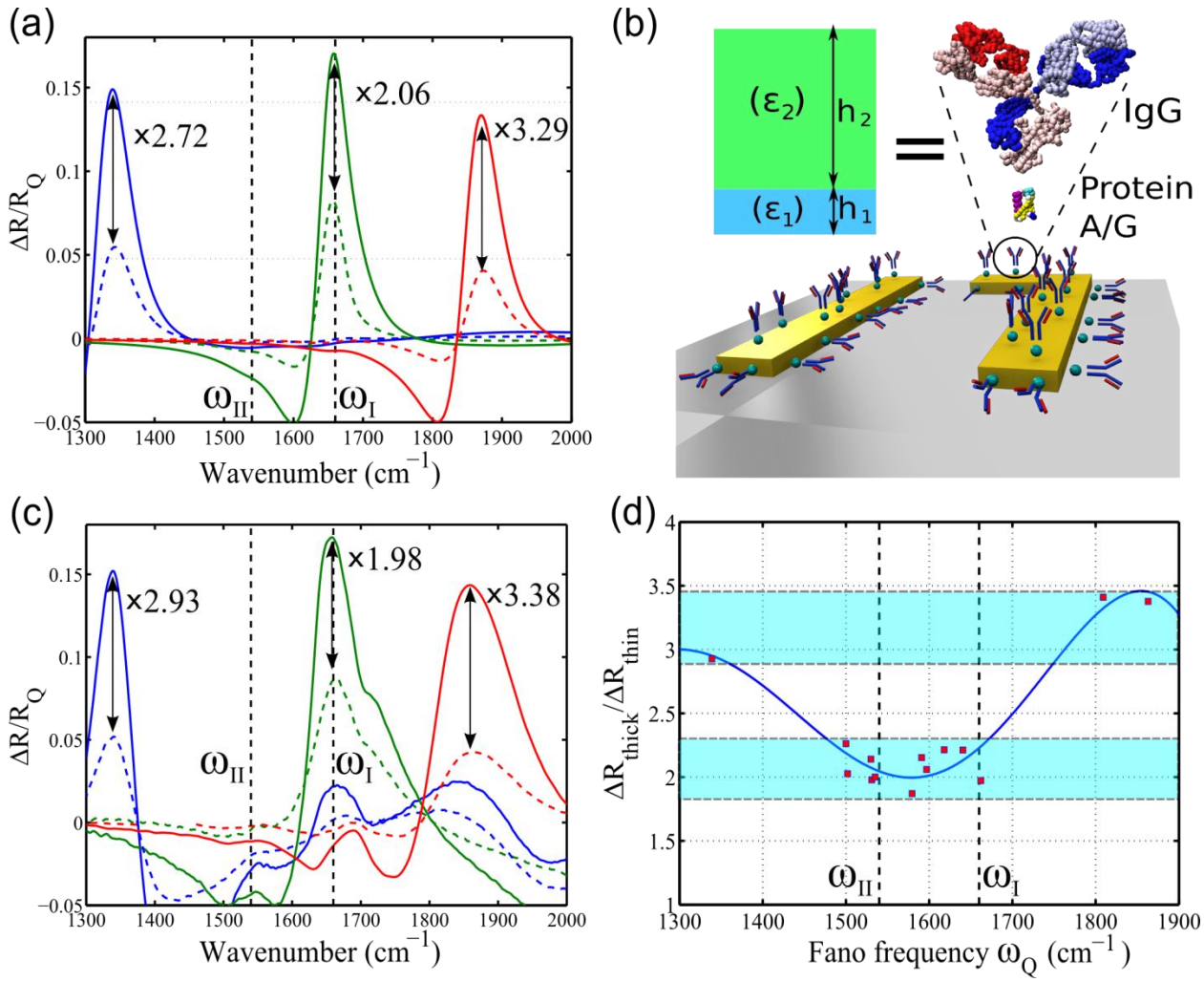

Figure C.2-3: Application of FRAMM-based substrates to reflectivity-difference spectroscopy of protein mono- and bi-layers. Protein A/G serves as a recognition moiety; IgG antibodies are the target molecules binding to Protein A/G. The plotted quantity is the normalized reflectivity $D^{(\omega_Q)}(\omega) \equiv \Delta R^{(\omega_Q)}(\omega)/R_Q^{(\omega_Q)}(\omega = \omega_Q)$ (a) Theoretical and (c) experimental spectra before (dashed lines) and after (solid lines) binding of IgG antibodies to three different FRAMM substrates immobilized by the Protein A/G. Indicated reflectivity ratios vary with the spectral position of the FRAMMs' resonant frequencies. (b) Schematics of proteins' mono- and bi-layers binding to the metal surface (not to scale) and the equivalent dielectric model. (d) Experimental peak reflectivity ratios (markers: 14 FRAMM arrays on 3 separate wafers). Dashed vertical lines: frequencies of the Amide-I and Amide-II vibrational modes.

While the above thickness measurement is not structure-specific, we demonstrate below that an array of FRAMM pixels (labeled by their ω_Q) can be used for *vibrational fingerprinting* of proteins. The non-specific contribution to $\Delta R/R_Q$ due to ϵ_∞ is effectively eliminated by calculating the first frequency derivative of the reflectivity spectrum $G^{(\omega_Q)}(\omega) \equiv -\frac{\mathrm{d}(\Delta R^{(\omega_Q)})}{d\omega} / \frac{\mathrm{d}(R^{(\omega_Q)})}{d\omega}(\omega = \omega_Q)$. Specifically, $G^{(\omega_Q)}(\omega = \omega_Q)$ exhibits a local maximum when the Fano resonance frequency $\omega_Q$is matched to that of a vibrational mode (e.g., $\omega_{I,II}$). This occurs because of the reduction of the sub-radiant mode's lifetime due to the energy exchange between the FRAMM's electromagnetic mode and the protein's vibrational mode. Specifically, the magnitude of the spectral peak $G^{(\omega_Q)}(\omega = \omega_Q) \sim (h/l_Q) \times (A_m < cos^2\,\theta_m > /\gamma_m^2)$ yields information about spatial orientation of the vibrational modes.

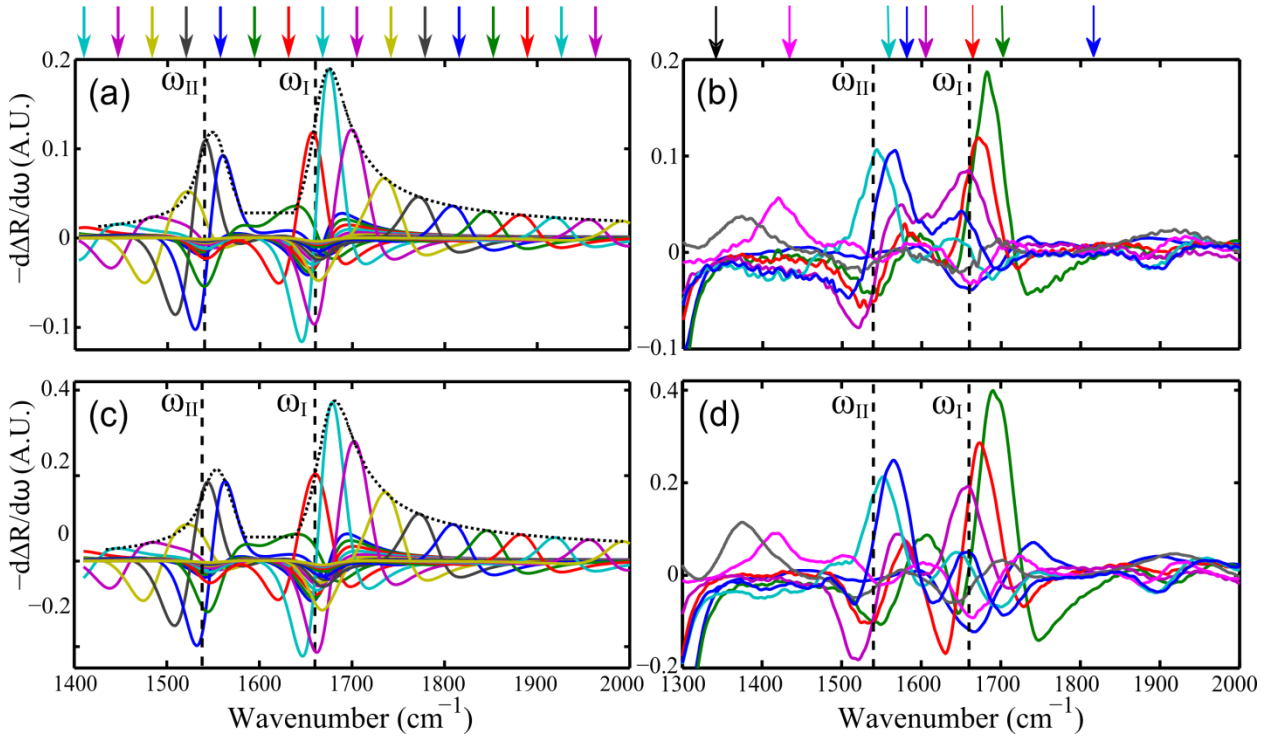

Figure C.2-4 : Visualization and identification of vibrational resonances of proteins using the normalized first frequency derivative spectra $G^{(\omega_Q)}(\omega)$ from an array of FRAMM-based pixels. (a,c) theoretical and (b,d) experimental data for (a,b) Protein A/G monolayer (recognition moiety) and (c,d) Protein A/G + IgG antibody bi-layer. Different FRAMM pixels are color-coded and their resonant frequencies ω_Q are indicated by arrows. Vertical dashed lines: frequencies of protein backbone vibrations (Amide I/II) strongly coupled to the resonantly-tuned FRAMMs. Smaller peaks in (b,d) around $\approx 1400 cm^{-1}$: CH_3 bending modes of the proteins' side chains. Dotted curves in (a,c): envelopes of the maxima of $G^{(\omega_Q)}$.

Theoretical plots of $G^{(\omega_Q)}(\omega)$ are shown in Figs. 4(a,c) for an array of 16 different FRAMM pixels coupled to a Protein A/G (recognition moiety) monolayer and a combined Protein A/G + IgG (recognition moiety + target) bi-layer, respectively, where both proteins are described by the two-resonance model of $\epsilon^{(1,2)}$ given by Eq. C.2-3 (see Appendix D.4). Experimental measurements shown in Figure C.2-4(b,d) confirm that the maxima of $G^{(\omega_Q)}(\omega)$ are spectrally co-located with vibrational resonances of the

monolayer and bi-layer. The data in Figs. 4(b,d) indicate that there is strong coupling of the FRAMM with the strongest conformation-sensitive protein backbone vibrations (Amide I-II) that are frequently used for studying proteins' secondary structure[68–70]. They can also be used for estimating surface orientation of small highly anisotropic proteins such as A/G. One qualitative feature of Figure C.2-4(b,d) is that the effective dipolar strength of Amide I (C=O stretch) is stronger than that of Amide II (C-N and C-C stretch, and N-H bend). This has been attributed[152] to stronger alignment of Amide I with the axes of protein's alpha-helices, which are normal to the metal surface for oriented proteins.

Although our experiment involved single-detector *sequential* measurement of the FTIR spectra from eight FRAMM pixels, an FPA of infrared detectors would enable *parallel* [108] acquisition of the spectra from a large number of FRAMM pixels. Such parallelization of data acquisition from multiple pixels, each producing a resonantly-enhanced spectrum, results in enormous speed-up of label-free structure-sensitive optical bio-sensing.

Finally, we illustrate how FRAMM-based biosensing enables distinguishing between multi-protein nanolayers by comparing $\Delta R^{(mono)}(\omega = \omega_Q)$for single-protein and $\Delta R^{(bi)}(\omega = \omega_Q)$ for two-protein layers. If proteins A/G and IgG were identical, then $T(\omega_Q) \approx H/h_1$would be expected for all FRAMMs. However, Figure C.2-3(c,d) reveal a considerably smaller $T(\omega_Q) < H/h_1$ for the resonantly-tuned FRAMMs. This implies a stronger contribution of Protein A/G's C=O vibration to $\epsilon_n(\omega)$ relative to that of IgG, i.e. $\tilde{A}_I^{(A/G)} > \tilde{A}_I^{(IgG)}$. The analytical model predicts (Supplement C) a similar trend for $T(\omega_Q)$ when $\omega_Q \approx \omega_I, \omega_{II}$. To interpret this result, we have used the Protein Data Bank (PDB) to extract and diagonalize the C=O directional tensors of IgG (PDB code 1IGY) and

Protein A/G (67% of Protein A, PDB codes 1EDI and 1BDC, and 33% of Protein G, PDB codes 1GB1 and 2IGD). By assuming that the alpha-helices of Protein A/G and the Fc region of IgG are parallel to the surface normal, we obtained $< cos^2\,\theta_I^{(IgG)} >_{kk} = (0.29; 0.32; 0.39)$ (almost isotropic) and $< cos^2\,\theta_I^{(A/G)} >_{kk} = (0.14; 0.22; 0.63)$ (highly anisotropic: strong Amide I contribution), where $k = x, y, z$. These estimates are consistent with the resonant absorption data $G^{(\omega_Q)}(\omega)$ shown in Figure C.2-4(b,d) by indicating that a bi-layer, which is $H/h_1 \approx 2.9$ times thicker than a monolayer, produces only twice the absorption: $G^{(\omega_Q)}(\omega = \omega_Q) = 1 + (h_2/h_1) \times (< cos^2\,\theta_I^{(IgG)} >_{zz} / < cos^2\,\theta_I^{(A/G)} >_{zz}) \approx 2.2$. Note that this result is not sensitive to IgG's binding orientation, but is highly sensitive to Protein A/G's surface binding. Therefore, the multi-pixel FRAMM provides valuable information about the thickness and surface binding of small anisotropic proteins, as well as the target antibodies on protein-functionalized substrates.

C.2.3 Conclusions and Outlook

The concept of a Fano-resonant asymmetric metamaterial (FRAMM) enables novel plasmonic substrates that combine strong near-field enhancement, sharp spectral features, and easy identification of the resonance frequency via polarized reflection spectroscopy. Designed to operate in mid-infrared part of the electromagnetic spectrum, such substrates can be used for implementing structure-resolving label-free biosensing. Tremendous improvements in sensitivity, speed, and time-resolution of biosensing can be achieved by parallel acquisition of the FTIR spectra from large functionalized arrays of narrow-band FRAMM pixels covering a significant portion of the fingerprint spectral region. By using infrared-transparent substrates, one can envision unlocking the

mysteries of the conformational dynamics of biomolecules in their natural aqueous environment responsible for life-sustaining molecular binding processes.

Chapter C.3 : Fano Resonance Vs Fluorescence for Protein Detection

One of the prominent approaches to biosensing involves using fluorescent labels[155,156]. In all studies where fluorescent dye is used, the question arises about the possible interference by the dye with the processes under study[155,156]. Also, fluorescence is known[157,158] to quench in the presence of gold nanoparticles, which is often used[124,146,148,149,159] in therapeutic and diagnostic purposes. Choi et al. discuss the problem of quenching and introduce one approach to alleviate this problem— to enhance the fluorescence in order to overcome quenching.[160] In another recently developed method, Fano Resonant Asymmetric Metamaterials (FRAMMs) have been demonstrated[161] to be a sensitive and specific method of detecting proteins. In this chapter we are interested in comparing the detection capability of our FRAMM sensors to the standard fluorescence assays. We use both fluorescence and FRAMM based sensing techniques to form a comparative understanding of the two methods and how they work together.

For the purpose of biosensing the infrared region is especially interesting because many molecular vibrational lines happen to be in this region. Amide, phosphate and lipid molecules have their characteristic lines in the $900 - 1800\ cm^{-1}$. For example, two of the lines frequently[9,63,162,163] used to fingerprint protein are backbone amide-I at $\omega_I = 1620 - 1680\ cm^{-1}$ and amide-II at $\omega_{II} = 1510 - 1580\ cm^{-1}$. To clearly resolve these two resonances requires the probing sensor to have[8] a quality factor ~ 10 or even higher for resolving secondary structures, which is achievable in a Fano resonant asymmetric metamaterial (FRAMM).

FRAMM has been introduced in detail in Chapter B.2. The unit cell of these metasurfaces are illustrated in Figure B.2-1 and Figure C.2-1. Note that the unit cell has three notable resonances— the x-dipole resonance, the y-dipole resonance and the quadrupole resonance— which give rise to a double continuum Fano resonance. This results in a Fano-type spectrum in y-polarized light (R_{yy}) and a Lorenzian in x-polarized light (R_{xx}). The advantages of using such a sensor structure has been described in detail in Chapter C.2. Its use for monolayer protein detection using FRAMMs has been demonstrated[8] to go beyond index sensing, to be ultra-sensitive, and specific.

A family of FRAMMs were investigated in a previous work[164]. From this study a structure with $s_y = 0.52\ \mu m$ (labeled[3] P6 here) was picked because the P6 structure has higher Q, and yet significant Fano feature in y-polarized light. This structure also has significant x-polarized reflectivity at peak ($R_{xx}^{peak} \sim 20\%$), so that x-polarized spectra are also usable if necessary. In this work we shall focus on the y-polarized spectra.

C.3.1 EXPERIMENTAL PROCEDURE

It is possible to estimate orientation of protein molecules using the FRAMM sensors with very small sample volume. In the previous report[8], an intermediary linker was used (protein A/G) to create a bilayer with the target (IgG) exposed. The linker protein A/G attaches to the gold surfaces because of electrostatic attraction. In water, or other polar medium the attraction is weaker. As a result, when working with a mixed analyte, there is a risk of the linker protein A/G to be replaced. Here we[4] directionally bind the antibody through a dithiol linker. This linker provides stronger, almost covalent-

[3] The first structure to be investigated had $s_y^{Pi} = 1.12\ \mu m$. The P6 unit cell has the horizontal antenna moved down by $.6\ \mu m$, to $s_y^{P6} = 0.52 \mu m$. Hence the label P6.

[4] This work was performed in collaboration with Albert Lee, Department of Biomedical Engineering, Univ. of Tx. Austin and Prof. Konstantin Sokolov, MD Anderson Cancer Center, Houston.

like, bonding to the gold as opposed to the electrostatic interactions of protein A/G which will prevent the replacement of the antibody by other molecules in biological samples. Additionally the linker, which binds to the Fragment crystallization (Fc) region of the antibody, orients the antibody such that the Fragment antigen-binding (Fab) portion is directed away from the substrate. Another major advantage of this new protocol is that the captured antibodies are attached directly to the sensor surface without an intermediate antibody layer. This makes the protocol for binding antibody a one step process.

The antibody used is clone 29.1 from Sigma-Aldrich, it is a monoclonal Anti-EGFR antibody. It has a mass of $170\,kDa$ compared to $22\,kDa$ of protein A/G and $150\,kDa$ of protein IgG. In other words, the anti-EGFR protein has atomic weight comparable to the IgG used before (Chapter C.2). The linker, used for attaching the antibody to the gold surface is a group that is attached to the antibody. It consists of an amide-bonded hydrazide and an alkane terminating in a dithiol functional group which attaches to gold. The antibody is mixed with $NaIO_4$ which oxidizes the carboxyl to an aldehyde on the Fc region of the antibody. The aldehyde will undergo condensation with the hydrazide covalently binding the linker to the Fc region of the antibody. This antibody can now be taken to gold as the dithiol linker will associate strongly with gold.

Fluorescent Dye

To make the antibody fluorescent, a dye molecule was attached[5] to the antibody. For the dye attachment, Alexa Fluor 647 dyes from Invitrogen were used. These are dyes

[5] Dye attachment procedure:
1. Prepare a 1 M sodium bicarbonate by adding 1mL DI water to the provided vial of sodium bicarbonate (Component B). Vortex or pipet up and down until fully dissolved. It will have a pH ~8.3 (Double check with a pH paper) and can be stored at 4C for up to two weeks
2. To 1mg/mL antibody, add 1/10 volume of 1 M sodium bicarbonate buffer
Note. Bicarbonate, pH ~8.3, is added to raise the pH of the rxn mixture since succinimidyl esters react efficiently at pH 7.5-8.5

terminated with succinimidyl esters which react with amines, making them ideal labels for antibodies. Fluorescently labeled antibodys were used to independently confirm attachment of the antibodies to the sensors. These dyes fluoresce at a wavelength of 647nm.

To compare the traditional fluorescence detection technique and the FRAMM based sensing, we first prepared a sample with thin layer (monolayer) of antibody deposited on the FRAMM array.

Sensor Fabrication

The sensor array consisted of a row of 11 'pixels'. Each pixel was a $\sim 150\ \mu m \times 150\ \mu m$ array of the P6 unit cells uniformly scaled in plane. Each of the pixels were tuned to slightly different frequencies in the range of $1450 - 1900\ cm^{-1}$ (see Table C.3-1). The sensors were fabricated using electron beam lithography with a JEOL 7000 e-beam aligner. 950 PMMA C2 was spun on $2cm \times 2cm$ and $0.5\ mm$ thick pieces of CaF_2 at $1700\ rpm$ for $60\ s$ and then pre-baked at $180°C$ for $2\ min$. A $5\ nm$ thick layer of Cr was deposited to promote conduction on the sample. The exposed samples were developed in 1:3 IPA:MIBK for 60s after etching away the Cr layer. After which a 70nm layer of gold was deposited on the developed samples and liftoff performed in acetone.

The quadrupole resonance frequency of the sensor pixels were tuned across the amide-I and II region. The values of quadrupole resonance are tabulated below:

---

3. Transfer the protein soln to the vial of reactive dye (Component A). Cap the vial and invert a few times to fully dissolve the dye. Stir the reaction mixture for 1 h at room temperature; vial has a magnetic stir bar; EVERY 15 MINS gently invert the vial in order to mix the two reactants and increase the labeling efficiency

Pixel no.	Scaling factor (s)	$k_Q^{dry}(cm^{-1}) \pm 5\%$	$k_y^{dry}(cm^{-1}) \pm 5\%$
1	0.77	1875	2325
2	0.81	1795	2200
3	0.85	1695	2080
4	0.87	1665	2030
5	0.89	1635	1990
6	0.91	1600	1960
7	0.92	1570	1910
8	0.94	1545	1885
9	0.97	1515	1850
10	0.98	1490	1820
11	1.00	1450	1770

Table C.3-1: Numeric labels, scaling factor and resonance frequencies of P6 pixels ($s_y = 0.52\ \mu m$; for a definition of s_y see Chapter B.2) used for the work presented in this chapter. The scaling factor was used to scale all in-plane dimensions of the unit cell described in Figure B.2-1. The scaling tunes the resonance frequencies of the individual 'pixels' or arrays to specific value. Random fabrication errors lead to some fluctuation in the resulting frequency leading to the $\pm 5\%$ change in the resonance frequencies.

The CaF_2 substrates are very brittle, which require very careful handling. CaF_2 has lower thermal conductivity and larger thermal expansion coefficient than, say, quartz. Rapid changes in temperature leads to non-uniform temperature in the substrate. This creates uneven thermal expansion in the substrate which, in turn, creates large enough strain to break the substrate. As a result in all the steps that expose the CaF_2 to temperature change need to be carefully managed so that the substrate is not heated too fast.

Antibody (anti-Epidermal growth factor receptor, or anti-EGFR) Deposition Method[6]

Before the deposition of antibody, the sample was cleaned using RCA I clean with H_2O_2:NH_4OH:H_2O = 1:1:5 at $70°C$ for 5 minutes. Adhesion of the metasurface to the CaF_2 substrate was inferior when compared to quartz substrate, longer RCA clean permanently damaged the sensor pixels.

A drop of diluted antibody anti-EGFR was left on the cleaned sample for 8 hours on a shaker. After 8 hours the sample was washed thrice with distilled water and allowed to dry in air. Since the antibodies attach through a thiol linker, all the excess antibody was washed away, and we obtained a monolayer. To obtain a thick layer of antibody, washing was performed only once after antibody deposition. The resulting antibody layer was thick and non-uniform.

Data Collection

Reflection spectra of the sensor pixels were collected with a $4\ cm^{-1}$ resolution using a Thermo Scientific Continuum microscope coupled to a Nicolet 6700 FTIR spectrometer with 128 averaging cycles. Reflection spectra in both x- and y-polarized light were collected from a gold mirror, and then the pixel. The ratio of these two spectra as percentage gives the reflectance (R_{yy}). Reflection spectra R_{yy}^{bare} and R_{yy}^{ab} were collected before and after the antibody deposition.

C.3.2 Results and Discussions

For analyzing data a procedure similar to that discussed in Chapter C.2 was adopted. First the spectra before (R_{yy}^{bare}) and after the antibody deposition R_{yy}^{ab} were

[6] Albert Lee, dept. biomedical engineering, Univ. Tx. Austin prepared the protein and deposited the protein layers and collected the fluorescent images. I fabricated the samples, took the data and performed the data analysis.

collected. The dipole peaks of the spectra were normalized to 100%. Then the difference spectra $\Delta R_{yy}/R_Q = (R_{yy}^{ab} - R_{yy}^{bare})/R_Q$ was calculated[7]. Here R_Q is the reflectivity at quadrupole frequency of the bare pixel. To find the value of R_Q first we need to identify the quadrupole resonance frequency, which corresponds to the peak in the x-polarized reflectivity spectra (R_{xx}). In the difference spectra, there were a clear signal from the deposited antibody (see Figure C.3-1).

In the difference spectrum, the step-like feature characteristic of an index shift is clear (Figure C.3-1) when the pixel is tuned away from amide I and amide II resonances. When the pixel resonance is closer to the amide I resonance at 1660 cm^{-1}, the feature is enhanced. Subsequently as the pixel resonance moves away from amide I the difference signal diminishes.

[7] R_{yy}^{ab} was not shifted in k in this case because I wanted to retain the effects of index change.

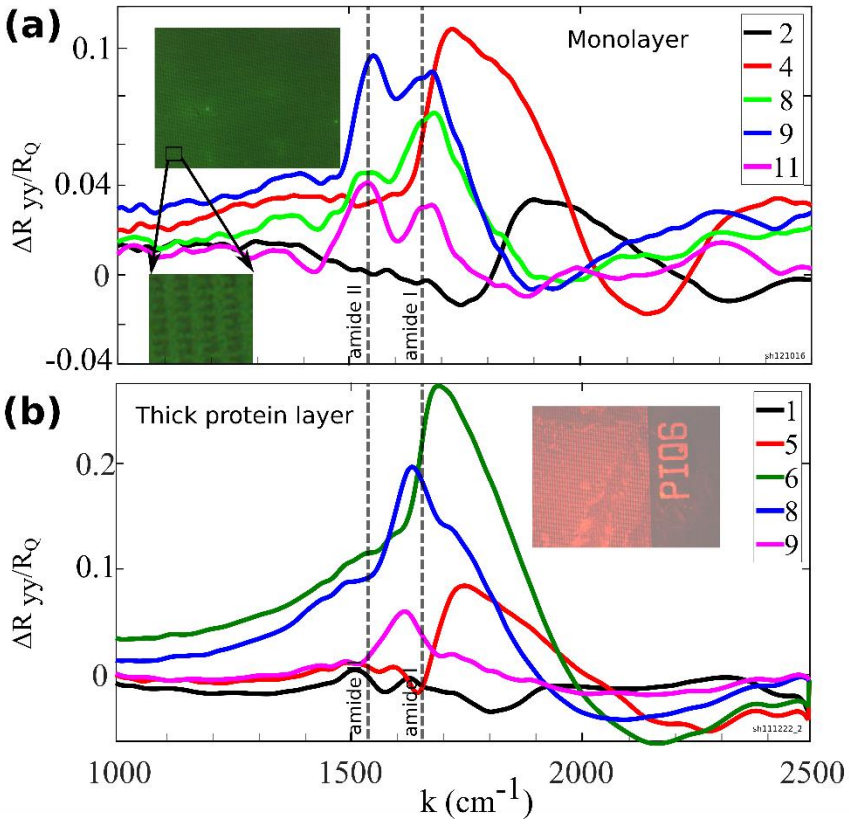

Figure C.3-1: Compares spectra from thick and thin (monolayer) antibody layer on sensor (P6 pixels, see Table C.3-1). (a) and (b) show normalized reflectivity difference spectra ($\Delta R_{yy}/R_Q = (R_{yy}^{bare} - R_{yy}^{ab})/R_Q$) Selected pixels were plotted in either case to illustrate the evolution of Fano resonance-antibody resonance interaction. In both cases the signal is clear. For both cases the two amide lines are discernible (amide I at $1660\ cm^{-1}$ and amide II at $1540\ cm^{-1}$). In the case of thick antibody the signal strength is higher. Insets show fluorescence images of the pixels. In (a) the image is obtained with 0.5s exposure, compared with 60s for (b). One can discern the metasurface in the first case where the antibody predominantly binds. For the monolayer there is no fluorescence where there are gold structures- it is believed to be quenched by the gold. The origin of change in the thin layer (in panel a) to greenish tint is possibly photobleaching due to the extremely long exposure.

The thick layer was obtained as described before. This resulted in pile-up (i.e. antibody layer thicker than a monolayer) of antibody in certain locations of sample, but

there was antibody everywhere on the metallic surfaces as may be seen from the fluorescent images (see Figure C.3-1). In the case of the thick antibody, the signal strength is considerably higher. Ellipsometric study revealed that the thick layer is on average about an order of magnitude thicker than the monolayer. However, because of the exponential nature of the field interacting with the antibody layer, the field exponentially diminishes in the length scale of $100\ nm$, and therefore thicker layers do not necessarily give much higher signal.

It is also important to note that for the thick layer a faint fluorescence signal from the antibody is visible away from the gold structures, but the antibody on the gold structures do not fluoresce. This is probably due to quenching by gold.

In addition to the difference spectra, the derivative spectra (Figure C.3-2) is calculated for accurate determination of the features and vibrational fingerprinting. The amide I and amide II features are clearly visible in the derivative spectrum ($\frac{dR_{yy}}{dk}$) . In the derivative spectra, however, the amide I line is overwhelming the amide II probably because of broadening due to the non-uniformity of the layer, which in effect tunes the Fano resonance differently in relatively thicker and thinner regions. This effect masks the weaker amide II resonance.

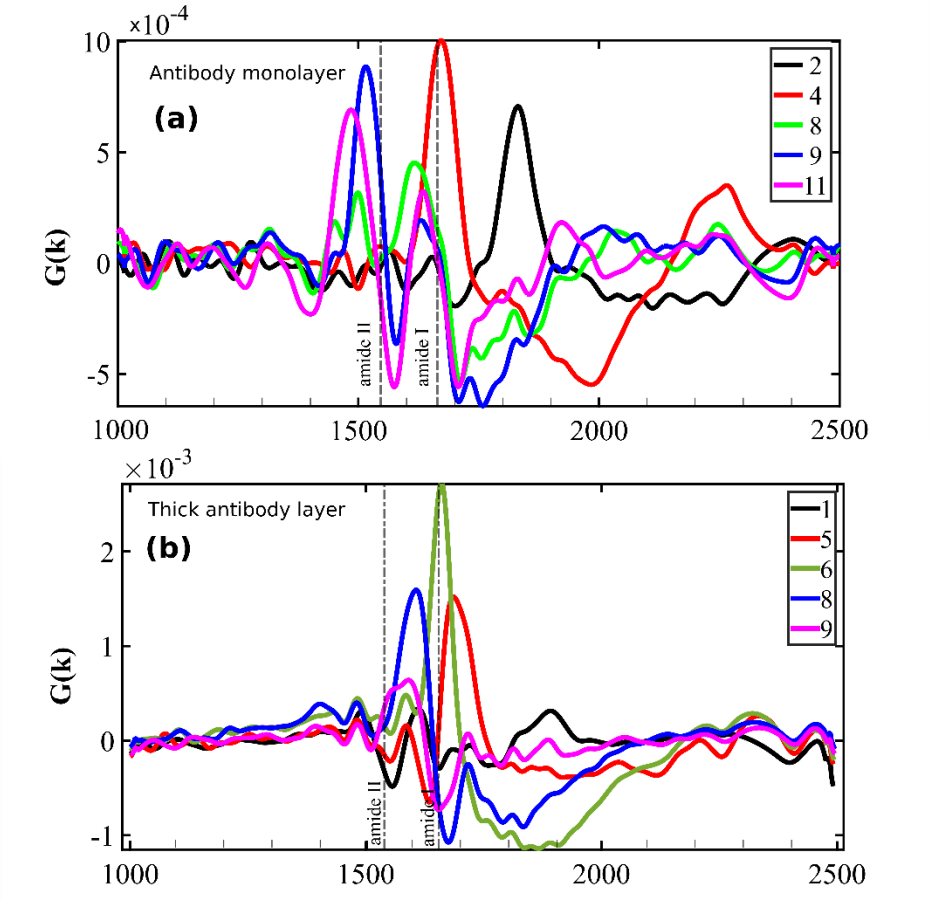

Figure C.3-2: Shows derivative spectra of the obtained signal ($G(k) = \frac{d}{dk}\Delta R_{yy}/R_Q$). The evolution of G(k) for the different pixels reveals the fingerprint amide I and amide II resonances at 1660 cm^{-1} and 1540 cm^{-1}. This behavior is similar to that seen previously[8] (Chapter C.2). a) Shows evolution of

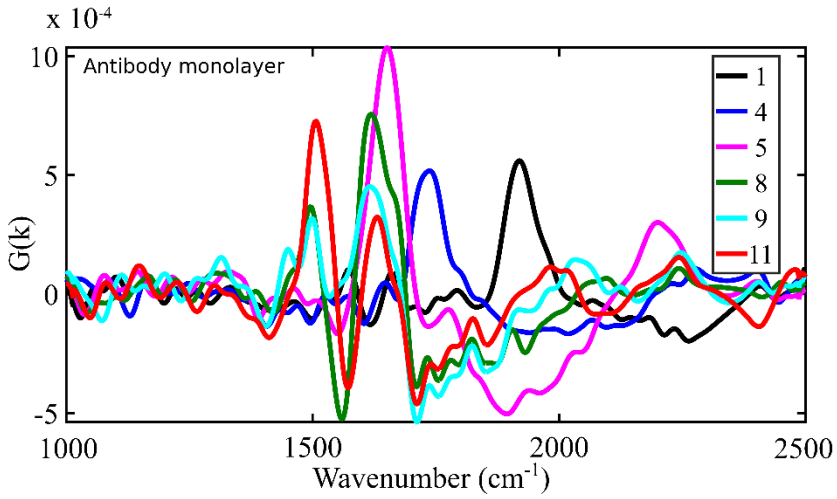

Figure C.3-3: Repeat of the thin protein layer experiment. Figure shows derivative spectra of the obtained signal ($G(k) = \frac{d}{dk}\Delta R_{yy}/R_Q$) from sensor pixels using the P6 structures.

To verify that the results are reproducible, a second experiment was performed (Figure C.3-3) and the derivative spectrum was plotted. Peak intensities are seen in pixels 4 and 5, respectively. The reason for this apparent discrepancy is that there is slight change in resonance frequencies between samples. Pixel 4 in experiment 1 has very similar resonance frequency as pixel 5 for the second experiment.

C.3.3 Conclusions and Outlook

We therefore conclude that the FRAMM is a powerful tool for specific detection of antibody (or indeed, any material with fingerprint in the IR region), and it is label free which makes it more versatile compared to fluorescent labeling. In the case of fluorescent monolayer, there was no fluorescence from the gold covered areas. Since FRAMM sensors detected presence of antibody, we conclude that the fluorescence was quenched. In the case of the thick layer of antibody, since fluorescence was visible from the areas covered with gold, and very little from the exposed substrate. This indicates that there

was little non-specific attachment of protein to the substrate, as desired. It is also clear that in the case of thick protein, there was protein-protein attachment which led to the thick layer of protein. This also allowed the protein molecules not directly attached to the gold surfaces to fluoresce.

Later in this dissertation we shall discuss the use of these sensors for cell characterization. Especially in the presence of gold structures or nanoparticles, which is frequently the case for bio-sensing, a FRAMM based sensor is better suited for sensing applications compared to traditional fluorescent dye. It also has the added advantage of being label-free.

Chapter C.4: Distinguishing Cell Types: Dry[8] Experiments

Spectroscopic methods for distinction of cell types include Fourier Transform Infrared (FTIR) spectroscopy[165–169], attenuated total reflection (ATR) FTIR spectroscopy[170], Raman spectroscopy[171,172], photothermal spectroscopy[173]. All of these methods rely on light-matter interaction and absorption of light by the analyte. The detection method of these interactions set these methods apart. These methods make room for detection and quantification of cellular biomarkers including DNA, RNA, lipid etc[168,173,174]. The FTIR spectra give a biochemical fingerprint that in turn depends on the type of a cell clinical state of a cell.

FTIR signal from a biological system is the sum of contributions from biomolecules present [175]. Major advantage of the FTIR spectroscopy are that it is fast, and require relatively little sample preparation. The FTIR signal arises out of absorption of IR signal by vibrational transitions in covalent bonds. Intensities and spectral locations of the peaks provide important information about the quantity, structure and molecular environment of the analyte. Although overlapping bands from different molecules make identification difficult[175] The FTIR has been used for characterizing blood[176], urine[177], plasma[178]. The partial least squares method allows the determination of 8-10 molecular concentrations in plasma with good accuracy[178].

Microspectroscopy with FTIR is potentially an inexpensive and automated tool for distinction of different types of cells[179,180] including identification of cancer biomarkers in de-waxed tissue sections cut from paraffin blocks[170]. Advanced

[8] The term 'dry' in this chapter refers to the experimental setup in which the cells on sensor pixels are not immersed in water. No chamber is used nor are the cells surrounded by water.

computational methods allow for interrogation of molecular fingerprints in data obtained using FTIR microspectroscopy. Large scale studies would need to be undertaken to validate the viability of these methods [121].

The relatively new technique of FTIR imaging spectroscopy combines spectra from several points on a sample to an image[181]. The spectra are acquired in parallel through the use of a multi-channel detector and a (typically mirror-based to avoid dispersion) imaging optics. Spatial resolution of $5-10\,\mu m$ are common for these systems, which is comparable to the wavelength of operation. This high resolution allows for interrogation of single human cells with typical diameters in similar range. However, multiple images need to be collected to query a large area, which takes long and generate a very large amount of data. It is possible to use an IR macroscopic image at the cost of lesser resolution. The Fano resonant asymmetric metamaterial (FRAMMs, Chapter B.2) is used for spectroscopic distinguishing of cell types, as we discussed before (Chapter C.1).

C.4.1 Enhancement of Cell Signal with a Metasurface

Enhanced Field and Light Matter Interaction

Metasurfaces enable strong enhanced local electric field[182,183]. The local electric field drops exponentially away from the metal surfaces. High field enhancement is useful for sensing as stronger fields improve light-matter interaction, increasing signal from sensing target.

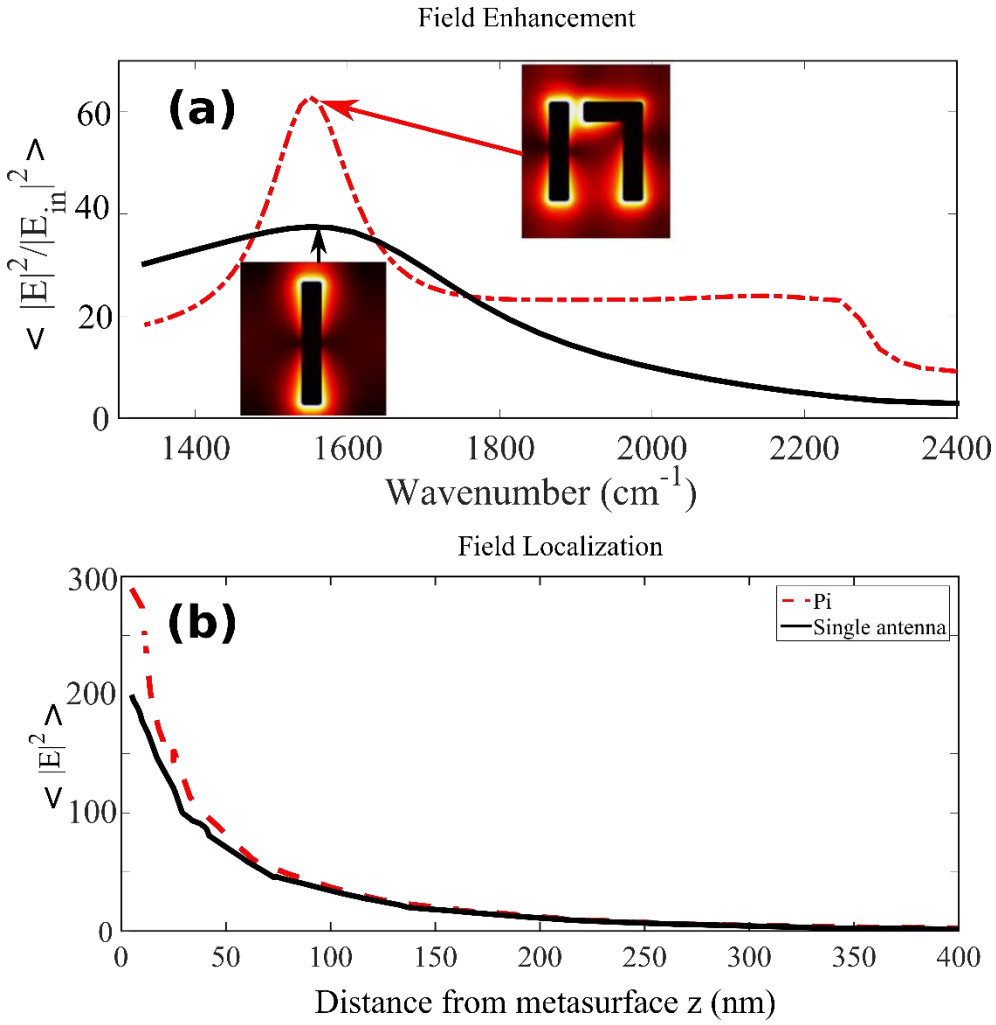

Figure C.4-1: (a) Field enhancement achieved by the FRAMM (P4 pixels) and antenna array. Field enhancement has been averaged over the all the surfaces of gold, except for the gold-substrate interface. Note the long flat shoulder in the curve for FRAMM. This allows for broadband sensing. The insets show field portraits of the two types of unit cells at resonance. The antenna length was adjusted so that its dipole resonance coincides with the quadrupolar resonance of the FRAMM structure. (b) Shows that in the vertical direction the field drops off within 100 nm of the surface.

Field enhancement (Figure C.4-1) of the FRAMM has three distinct characteristics— i) the Fano resonance peak for field enhancement is much sharper (dashed red curve, quality factor ~10) than the dipole (solid black curve, quality factor

~3), ii) the field enhancement of the FRAMM is about a factor two higher at resonance when compared to an antenna array (see refs[184,185]), and iii) There is a broad shoulder in the field enhancement curve that allows for relatively broadband sensing using a single pixel.

Sensor and Pixels

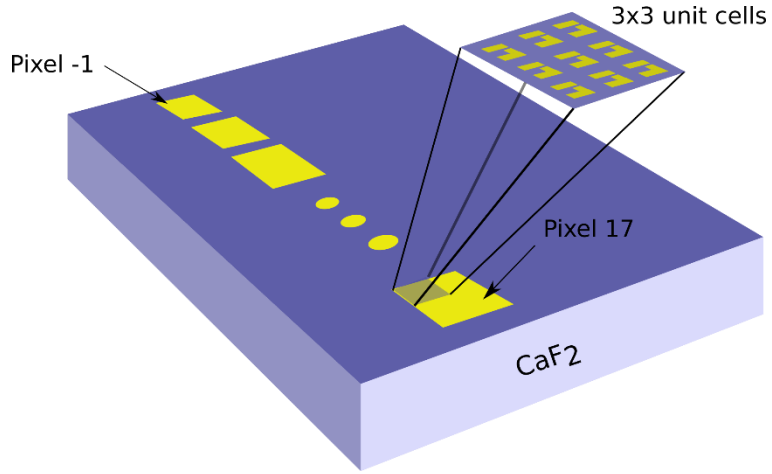

Figure C.4-2: Schematic of the sensor.

Sensor arrays were fabricated on CaF_2 substrate. The unit cell of the designed structure is shown in Figure C.4-2. A two dimensional (2D) array of these unit cells formed one individual sensor `pixel'. Fabricated sensor array on substrate had 14 or 19 pixels with different resonance frequencies. This tuning was achieved by scaling all the in plane dimensions, including the periods P_x and P_y of the unit cell. The pixel numbers and corresponding scaling factors and Fano resonance frequencies are tabulated below. A large number of pixels helps suppress statistical noise.

Pixel no.	Scaling factor (s)	$k_Q^{dry}(cm^{-1}) \pm 5\%$	$k_y^{dry}(cm^{-1}) \pm 5\%$	$k_Q^{H_2O}(cm^{-1}) \pm 5\%$
-1	0.40	3460	4540	2850
0	0.50	2830	3630	2410
1	0.65	2235	2840	1935
2	0.71	2060	2620	1810
3	0.73	2010	2510	1770
4	0.75	1965	2490	1745
5	0.77	1915	2425	1720
6	0.80	1845	2340	1685
7	0.84	1770	2250	1520
8	0.85	1745	2200	1500
9	0.86	1735	2185	1495
10	0.89	1670	2120	1460
11	0.92	1630	2055	1415
12	0.93	1615	2045	1400
13	0.95	1585	1995	1380
14	1.00	1510	1905	1325
15	1.20	1280	1600	1145
16	1.40	1115	1400	1020

Table C.4-1 continued on the next page

Pixel no.	Scaling factor (s)	$k_Q^{dry}(cm^{-1}) \pm 5\%$	$k_y^{dry}(cm^{-1}) \pm 5\%$	$k_Q^{H_2O}(cm^{-1}) \pm 5\%$
17	1.60	1000	1240	930

Table C.4-1: Pixels used in the cell sensing experiments ($s_y = 0.72\ \mu m$, the unit cell is defined in Figure B.2-1) were scaled uniformly in plane to achieve tuning of the metasurface sensor pixels. The columns refer to (i) The numeric label of pixels (ii) the scaling factor (iii) frequency of Fano resonance (k_Q^{dry}) (iv) frequency of the y-dipole resonance. (v) Shows the modified quadrupole resonance frequency ($k_Q^{H_2O}$) when the metasurface is submerged in water.

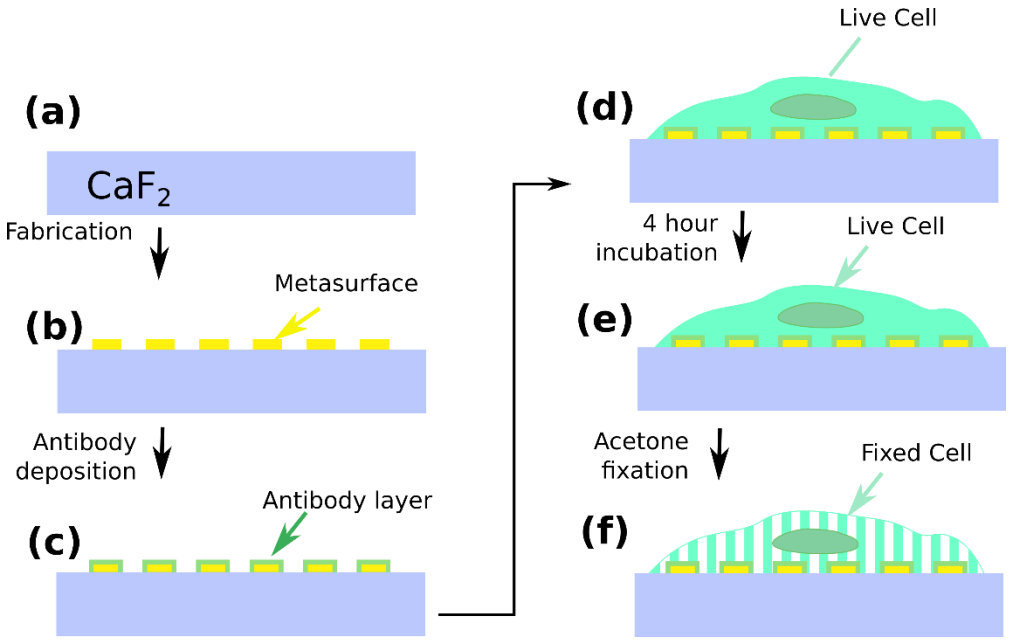

Figure C.4-3: Schematic of the sample preparation steps. (a)-(b) After fabricating the metasurface pixels, (c) an antibody layer is deposited for the capture of cells. (d) In the next step the live[9] cells are allowed to attach onto the sample and (e) incubated at $37°C$ for 4 hours. In the final step (f) the cell is fixed and left for a day before taking the fixed cell data.

[9] 'Live' experiments are performed with cultured cells that are still alive, but not immersed in media or even water. These cells, even though alive, will survive only for 2-3 hours in this condition. The cells are 'fixed' in chilled acetone before the cells die.

The cells under investigation were placed on the sensor (see Figure C.4-3), but the cells are not immersed in water. This is why we refer to this set of experiments as `dry sensing'.

When a cell is near such a metasurface, the field penetrates a small distance (~100 nm) into the cell, probing only peripheral region of the cell. This allows us to avoid complicated sample preparation steps. In a typical IR absorption measurements transmission of samples are obtained. For this the samples need to be carefully fixed and cross sections need to be prepared. In contrast, probing cells using reflection from the metasurface makes it greatly insensitive to the thickness of the cell layer. In particular, we can get accurate measurements even in the case of cell pile up. The metasurface allows us to probe a small cross section of the sample from the substrate side, provided the substrate is transparent to infrared light.

The metasurface enhances the reflected signal by an order of magnitude (Figure C.4-4). To demonstrate how effective this is, measurements were made on cells collected on bare substrate and on the metasurface covered with cells. Reflection from the cell on substrate was very small ($R \sim 1 - 2\%$) across the spectrum ($400\ cm^{-1} < k < 4000\ cm^{-1}$, where k is the wavenumber). Signal from the areas covered by the sensor arrays were significantly larger.

Example: Signal Enhancement

To illustrate the enhancement of signal, reflection spectra from a bare cell as well as that from a sensor (with cells on) are plotted in Figure C.4-4. When compared with spectroscopy from a region of cells deposited on the substrate, signal from cells deposited on a sensor pixel demonstrate much stronger signal strength and more prominent

features. (The data collection methods and the analysis procedure are described in detail later in Experimental Procedure.)

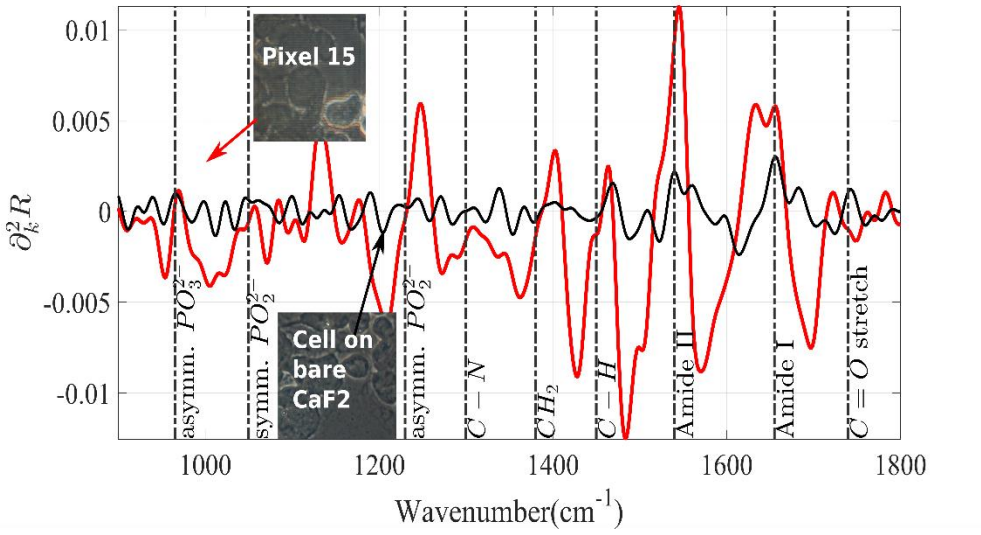

Figure C.4-4: Comparison of signal strength from cell covered areas with metasurface (red) and without metasurface (black). The features with metasurface is flipped with respect to bare substrate because features are π out of phase for the two surfaces. The metasurface used in this case is P4 pixel 15 (refer to Table C.4-1). It is clear that the metasurface significantly enhances signal from the cells. The signal from bare substrate is difficult to discern from the noise, except for the vibrational lines with large signal strength (e.g. amide I and II).

C.4.3 Experimental Procedure

Cell Preparation:

All the cells are cultured in cell culture medium (Thermo Fisher Scientific MEM solution) supplemented with 10% fetal bovine serum (FBS) at 37^oC and 5% CO_2. Prior to the experiments, the adherent cells (i.e. cells requiring a surface to grow) are detached from the surface using trypin. The cell suspension is then centrifuged at 1300 rpm for 3 min to pellet the cells. The supernatant is discarded and the cell pellet is re-suspended in cell culture medium (without FBS). Number of cells in a pellet ranges from 1-5 million,

which corresponds to roughly ¼ to ½ of cells in a culture flask at moderate to high coverage (on the culture surface of the flask), between 50-80%. This procedure removes cellular debris as well as dead cells prior to incubation with the metamaterial samples.

Cell Deposition

The sensor surface was covered with antibody (anti-EGFR) solution and put in a shaker for 4 hours. Afterwards, it was gently washed thrice with deionized water to remove excess antibody. This way, the sensor surface is covered with antibody to capture cells. The concentrated cell solution was drop cast on the surface, and about 10 minutes were allowed for the cells to settle at the surface (Figure C.4-5(a) and (b)). The sample was then incubated at 37^oC for four hours. We found that incubation enhances the molecular vibrational lines. Two different sets of measurements were performed. In the first kind of experiments, the cells were washed with PBS and the PBS was allowed to run off the sample by tilting it. Reflection spectra of the sample were obtained. This is the `live cell' data. The cell coverage was roughly 20-30 cells per pixel. In the second set of experiments, after the measurements of the live cells, the cells were fixed by incubating them in ice cold acetone for 15 min. The cells were washed in distilled water thrice to remove any residual acetone. After the fixation, the IR spectra were measured again. No water was added for the fixed measurements.

The cells are not in their optimal condition because they are not in growth medium. The cells live about 2-3 hours[10]. Collecting FTIR spectra from all pixels normally took between 1-2 hours. We verified that the cells were able to survive this duration by incubating cells in cell culture medium after taking data. After data collection, the sample surface with cells was immersed in cell culture medium and put in

[10] Private communication with Albert Lee, dept. of Biomedical Engineering, Univ. of Tx. at Austin.

incubation ($37°C$) for 4 hours. The cells were inspected under microscope, and were found to have grown. Therefore the cells could survive for the typical duration of data collection, or approximately 1.5 hours.

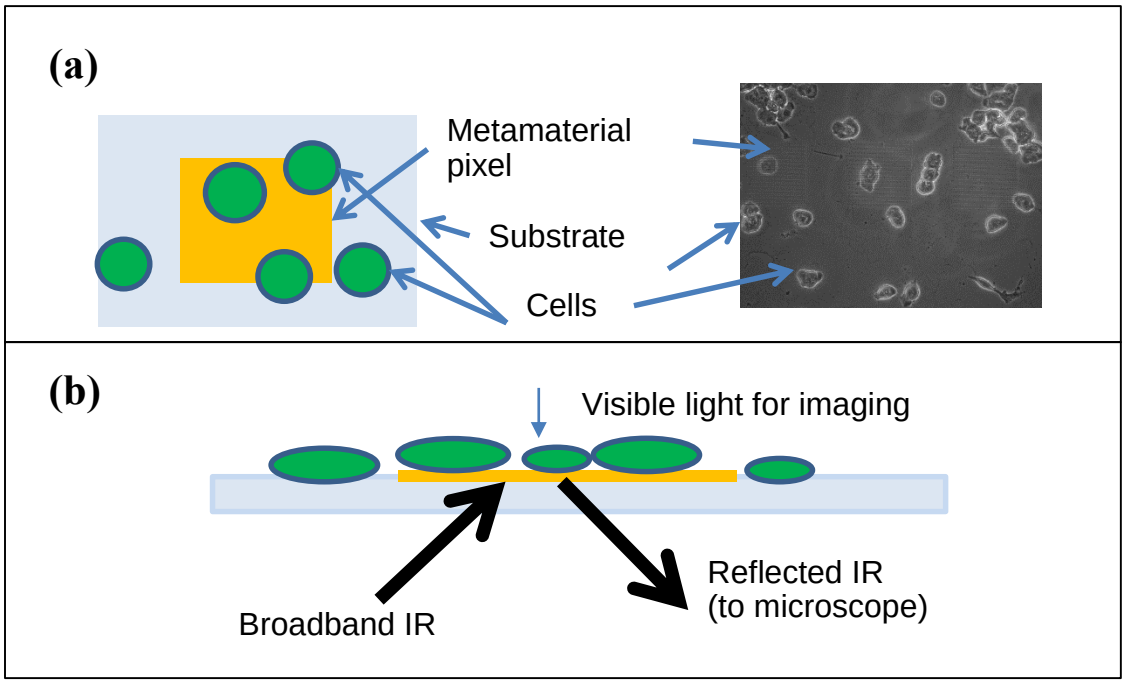

Figure C.4-5: (a) Schematic of the metasurface pixel (orange shaded region) with the deposited cells (green shaded region) from the top. The cells do not cover the whole metasurface. (b) Image acquired from the experimental sample clearly depicting the metamaterial pixel (bright square) and the cells (dark circular patches). The cells are imaged through the substrate and the metasurface. Illumination was from the top, and the objective was at the bottom. (c) Side view of the metamaterial pixel along with the illumination and collection geometry used in the measurement.

Data Collection

Reflection spectra from these live and fixed cells were taken through the substrate as illustrated in Figure C.4-5. Reflection spectra were collected with a 2 cm^{-1} resolution

by a Thermo Scientific Continuum microscope coupled to a Nicolet 6700 FTIR spectrometer. The collected spectra were then analyzed with Matlab. Reflection coefficient of the metamaterial as a function of frequency is shown in Table C.4-1.

Data Analysis

In bare spectra, the vibrational lines except for amide I and amide II are difficult to see with bare eye. In the first derivative spectra ($\partial_k R$), the vibrational lines become apparent (Figure C.4-6). We see 9-12 vibrational lines in the derivative spectra. Out of these, 9 lines that appear consistently were chosen for further analysis (Table C.4-2).

Data extraction was performed in two different ways. An exploratory analysis was performed with manually identifying the features in first derivative and calculating the height of the feature with respect to a local baseline[186]. This is described in more detail later in this chapter. In the other, more reproducible method, second derivative of the spectra ($\partial_k^2 R$) was used to quantify the features for automated extraction. We define a 'feature size' $\Delta_2 \equiv \Delta\partial_k^2 R$ (see Figure C.4-4) of a line as the difference between the peak and trough values in the $\partial_k^2 R$. The data extraction was performed by a Matlab script that looks for peaks and troughs in the defined neighborhood of where a vibrational line is expected. If a line is not detected, or too broad a line is detected (indicating that two or more features have convoluted) then the feature size is marked as zero.

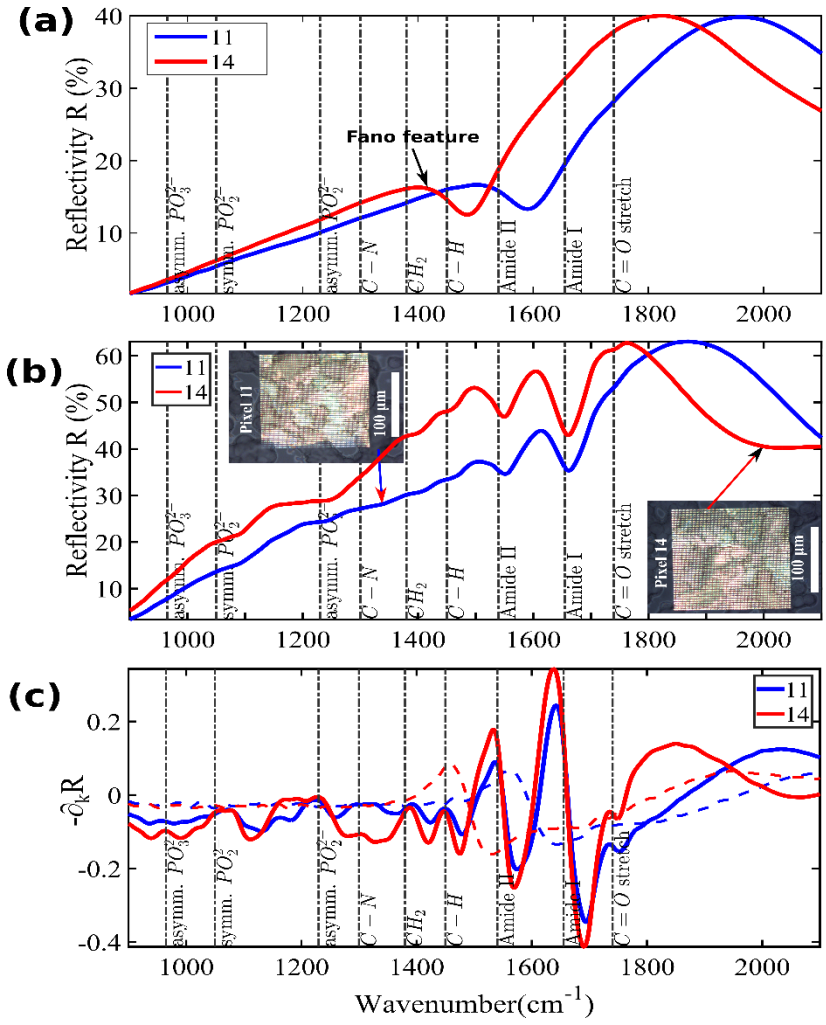

Figure C.4-6**:** (a) Reflectivity as a function of wavenumber for two metamaterial P4 pixels with different dimensions measured in the fixed state. Pixel 14 has larger in-plane dimensions than pixel 11 (see Table C.4-1). (b) Reflectivity for the pixels with fixed cells is shown as a function of wavenumber. Note that the Fano feature is difficult to discern once cells are deposited. The spectra is not as smooth as bare sensor pixels because molecular vibrational lines interfere with sensor reflectivity; only a few molecular vibrational lines are clearly discernible. (c) First derivative ($\partial_k R$) spectra of bare pixel and pixels with cells. The vibrational lines become much clearer in the first derivative spectra.

We note that when the cells are drop cast on the sample and the reflection measured in the dry state (`dry measurements'), the Fano feature disappears (Figure

C.4-6). This is due to the loss of homogeneity because of the addition of cells. Metamolecules under the cells experience a significantly higher refractive index and as a result experience a redshift, as opposed to those not covered by cells. This disparate behavior results in the disappearance of the sharper Fano feature, while preserving the broader dipole feature. We discuss this phenomena in more detail in section C.4.6.

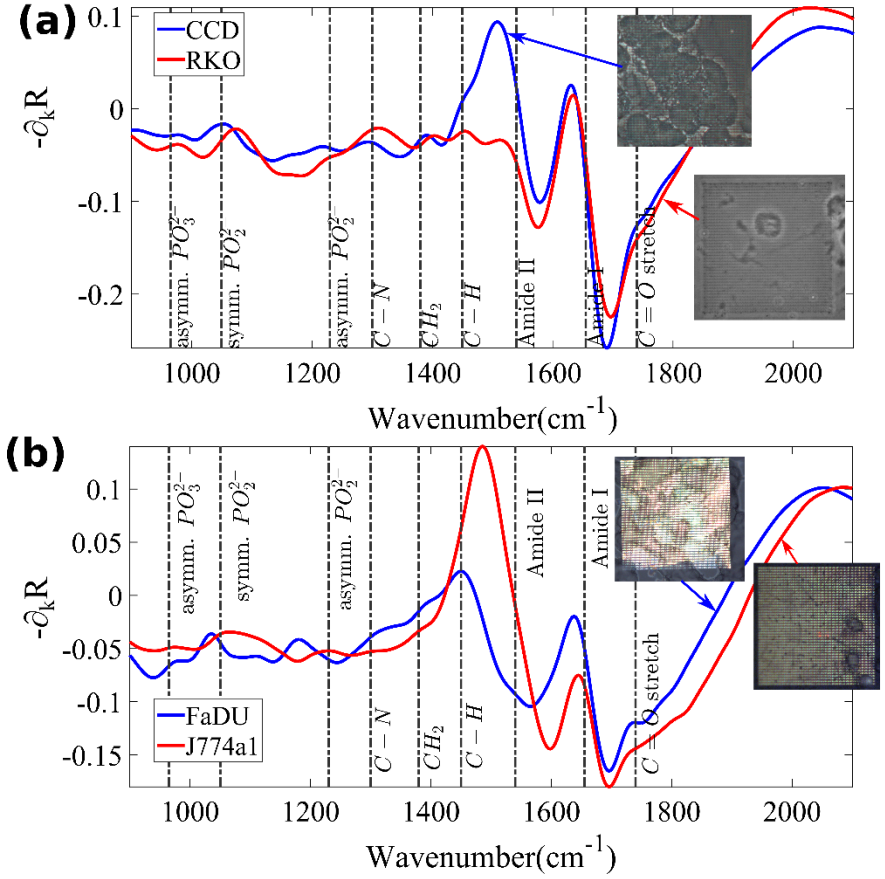

Figure C.4-7**:** (a) Comparison between spectra from fixed CCD 841 (human colon epithelial) and RKO (human colon epithelial carcinoma) cell lines for P4 pixel 11. (b) Shows the spectra for J774a1 (mouse macrophage) and FaDu (human pharynx cancer) cell lines for pixel 11. The differences between them may not be immediately obvious from visually examining the spectra, but a detailed analysis of the spectra reveal some clear distinctions.

Plot of derivative of the spectra ($-\partial_k R$) collected from the samples reveal several prominent features in the range of $900\ cm^{-1}$ to $1800\ cm^{-1}$. The most noticeable are roughly at the wavenumbers of $970\ cm^{-1}$, $1060\ cm^{-1}$, $1200\ cm^{-1}$, $1300\ cm^{-1}$, $1450\ cm^{-1}$, $1540 cm^{-1}$, $1660 cm^{-1}$, and $1740\ cm^{-1}$. These modes were identified using references[109–113,119,127] The amide I line at $1660\ cm^{-1}$ overlaps with water's vibration lines, and as a result is overshadowed by the H_2O line at $1670\ cm^{-1}$. To deconvolute these two lines require precise control of concentration of water, which we did not have in this set-up. It is therefore ignored in the rest of this study. The amide II line at $1540\ cm^{-1}$, however, is clear and undistorted by the H_2O vibrational line. Example derivative spectra ($\partial_k R$) of different cell types are shown in Figure C.4-7.

Below we tabulate the prominent vibrational lines seen in experiment:

k (cm^{-1})	Vibration mode[119,127]	Notes
965	Asymmetric phosphate $\nu(PO_3^{2-})$	Generally weak, but shows variation across cell types
1060	Symmetric phosphate	There are a few other lines in the close vicinity — glycogen ν(CC) (1078 cm^{-1}), ν(CO) (1060, 1050, 1015 cm^{-1}), ν(COP) (1050 cm^{-1})
1230-1245	Asymmetric phosphate $\nu(PO_2^-)$	DNA, RNA, phospholipid, phosphorylated protein
1300	Possibly ν(C-N)	Could be peptide, protein, collagen. Difficult to assign one vibrational line.
1380	CH_2 bending mode	
1450	$C-H$ vibration $\delta_{as}(CH_3)$, $\delta_s(CH_3)$ (and/or Amide III)	Lipid, protein
1510-1540	Amide II 60% $\gamma(NH)$, 30% $\nu(CN)$, 10% $\nu(CC)$	Prominent in most cell types
1660	Amide I 80% $\nu(CO)$, 20% $\nu(CN)$	Not used because it coincides with water. Difficult to deconvolute without a-priory knowledge of contribution from water. This line, however is useful for determining cell coverage on sensor.

Table C.4-2 continued on the next page

k (cm^{-1})	Vibration mode[119,127]	Notes
1740	$\nu(C=O)$ vibration	In literature this line is reported as lipid vibration [119,127]. Not visible for all pixels. The feature is prominent for CCD 841 and RKO for pixels 3-6.

Table C.4-2: Table of vibrational lines of interest. The lines correspond to the peaks in $-\partial_k^2 R\ vs\ k$ plot. In refs [119,127] these features are peaks in $\partial_k^2 R\ vs\ k$ plot. As we have seen in Figure C.4-4, the peaks in the bare cell spectra correspond to troughs in spectra collected from metamaterial sensors with cells.

C.4.2 Principal Component Analysis: Brief Introduction

From the experiments we obtain a large dataset from the experimental dataset. Moreover, since there are many different lines of interest (in our case we focus on 8-9), we essentially obtain a 9 dimensional dataset. It would be easier to handle the dataset if we could reduce the dimensionality of the dataset to only a few variables.

The aim of performing principal component analysis (PCA) is to reduce the dimensionality in a multivariate analysis. For a formal introduction to PCA, one may refer to Bro et al.[187] the relevant part of which has been quoted in Appendix D.5.

The best way to explain the idea behind principal component analysis is through a simple example. In this example we shall use fictitious data to illustrate the usage of PCA. We begin with the assumption that there are two major types of uses of the internet. For the purpose of this illustration we will ignore other uses. The first type of activity is what is called 'surfing' which is a pastime activity taken up usually in one's free time. The second type of activity is 'social interactions'.

Consider a group of people asked about the types of tasks they perform on the internet. They were asked how many minutes in a day were spent on an activity online.

Let us say that the survey asked users about five possible uses: i) reading news, ii) reading blogs, iii) watching videos iv) social networking sites v) sending and receiving emails.

All of these types of uses serve the two fundamental uses to a varying degree. A social network is mostly used for social interaction, but it may also be used for browsing. Watching a video is usually impersonal ('browsing'), except if the video is that of family or friends. Therefore none of the listed uses (columns in Table C.4-3), with the possible exception of reading the news, is purely 'surfing' or 'social interactions'.

Based on the country or region, the different types of usages are expected to vary. Social networking may be the predominant mode of internet usage in one country or region, and it may be sparingly used in others. We construct an artificial dataset to reveal the usefulness of PCA analysis. We assume that there are 3 countries where the usage patterns are different. We have picked 6 random respondents in each country for survey.

Here is how we construct the dataset:

1. Generate underlying vectors (browsing and social): construct two random arrays of 6 numbers[11]. The first array represents 'surfing' and the second 'social interactions'. We modeled that country 1 has a defined usages of (social, surfing) = (20m, 15m). Country 2 and country 3 have different 'social' to 'surfing' usages of (80m, 7m), and (10m, 60m).
2. Generate the 5 columns for each country: Now, the five columns were defined as
    a. News: surfing

[11] The number of "respondents" were picked so that the dataset could fit in one page. 5 or 6 "respondents" are enough to reveal the underlying statistics.

b. Blogs: 0.2 social + 1.5 surfing

c. Videos: 0.1 social + 0.9 surfing

d. Social networking: social + 0.05 surfing

e. Email: 0.2 social + 0.03 surfing

This gave us the country specific numbers for each column. A small amount of noise (~5%) was added to each column and then the numbers were rounded to the nearest minute.

We tabulate the constructed dataset for activities and the user responses below (Table C.4-3) :

Respondent number	Time spent on activities $\boldsymbol{v}_i(minutes)$				
	Read news	Read blogs	Watch videos	Social networking	Email
1	22	14	21	3	3
2	3	5	5	18	3
3	22	18	23	22	5
4	17	19	18	42	8
5	9	5	6	16	3
6	20	16	16	28	7
7	16	32	23	130	27
8	8	23	16	85	18
9	10	22	16	90	19
10	5	19	13	81	17
11	11	37	26	153	31
12	9	31	18	145	29
13	34	24	29	25	6
14	64	40	53	5	3
15	80	53	72	14	6
16	55	34	45	6	4
17	13	11	13	20	5
18	85	61	81	23	7

Table C.4-3: Sample data for PCA. The columns are different quantities measured, and the rows are 'instances' which in this case refers to one specific respondent. We will use the shaded area as a matrix in Matlab to calculate the principal components (see Appendix D.5). The instances are from six respondents each from the country 1(gray), country 2 (orange), and country 3 (green).

Our challenge now is to 'discover' using PCA that there are only two underlying variables, and using that fact, to 'discover' that there are 3 different subsets (one for each country) in the data.

The principal component is a linear transformation into a new basis. We know that each column in Table C.4-3 is a vector. Each 'principal component'($\boldsymbol{v}_i^{pc}$) is a linear combination of the column vectors ($\boldsymbol{v}_j$) i.e.

$$\boldsymbol{v}_i^{pc} = \sum_j \boldsymbol{c}_{ij}\boldsymbol{v}_j$$

such that the first principal component $\boldsymbol{v}_1^{pc}$ has the largest variation possible. The second principal component captures as much of the rest of the variation as possible and so on. Additionally, each principal component is linearly uncorrelated.

We find the principal component after normalizing each column vector to a length of 1, and then finding the principal components using Matlab. Normalizing the data is not always necessary. It depends on whether every vector is equally important or not. The procedure for the calculations are noted in Appendix D.5.

We find that the first principal component captures roughly 61% of the variation in the data, and the first two capture approximately 99.8% of the variation in data. This indicates that rather than five independent variables (types of uses for the internet), there are only two major classes of variable present in the dataset.

With that in mind, let's look at the principal component matrix $\boldsymbol{c}$. The rows of the matrix are used to construct the principal components. For example, the first principal component is given by $\boldsymbol{v}_1^{pc} = 0.57\boldsymbol{v}_1 + 0.3\,\boldsymbol{v}_2 + 0.74\,\boldsymbol{v}_3 - 0.12\,\boldsymbol{v}_4 - 0.13\boldsymbol{v}_5$.

	C_{1j}	C_{2j}	C_{3j}	C_{4j}	C_{5j}	%
1st principal component	0.57	0.3	0.74	-0.12	-0.13	0.615
2nd principal component	0.24	0.48	-0.29	-0.24	0.76	0.998
3rd principal component	0.45	0.39	-0.55	0.27	-0.52	0.999
4th principal component	-0.48	0.51	0.01	-0.61	-0.36	1
5th principal component	-0.42	0.52	0.25	0.7	0.12	1

Table C.4-4: Principal component of dataset (after column normalization) in Table C.4-3. The last column shows how much of the variation in the dataset is captured cumulatively. The first two principal components capture 99.8%, and the first three capture 99.9% of the variation. Ie. Keeping track of the third principal component does not add much value.

Now we transform[12] the dataset to the principal component basis. The first two and last two principal components are scatter plotted in Figure C.4-8. We can see that in the first plot, the different subsets are clearly distinguished, and in the last they are not. The PCA analysis allowed us to transform the 5 dimensional dataset into a new rotated axis, and project the dataset into a 2 dimensional space where more than 99% of the variation in the data is captured. In this way, it helped us reduce a difficult to manage and visualize 5D dataset into a 2D dataset that is much more manageable.

[12] See sec. D.5.1 for a mathematical description of the process. See sec. D.5.3 for instructions on how to do this using Matlab.

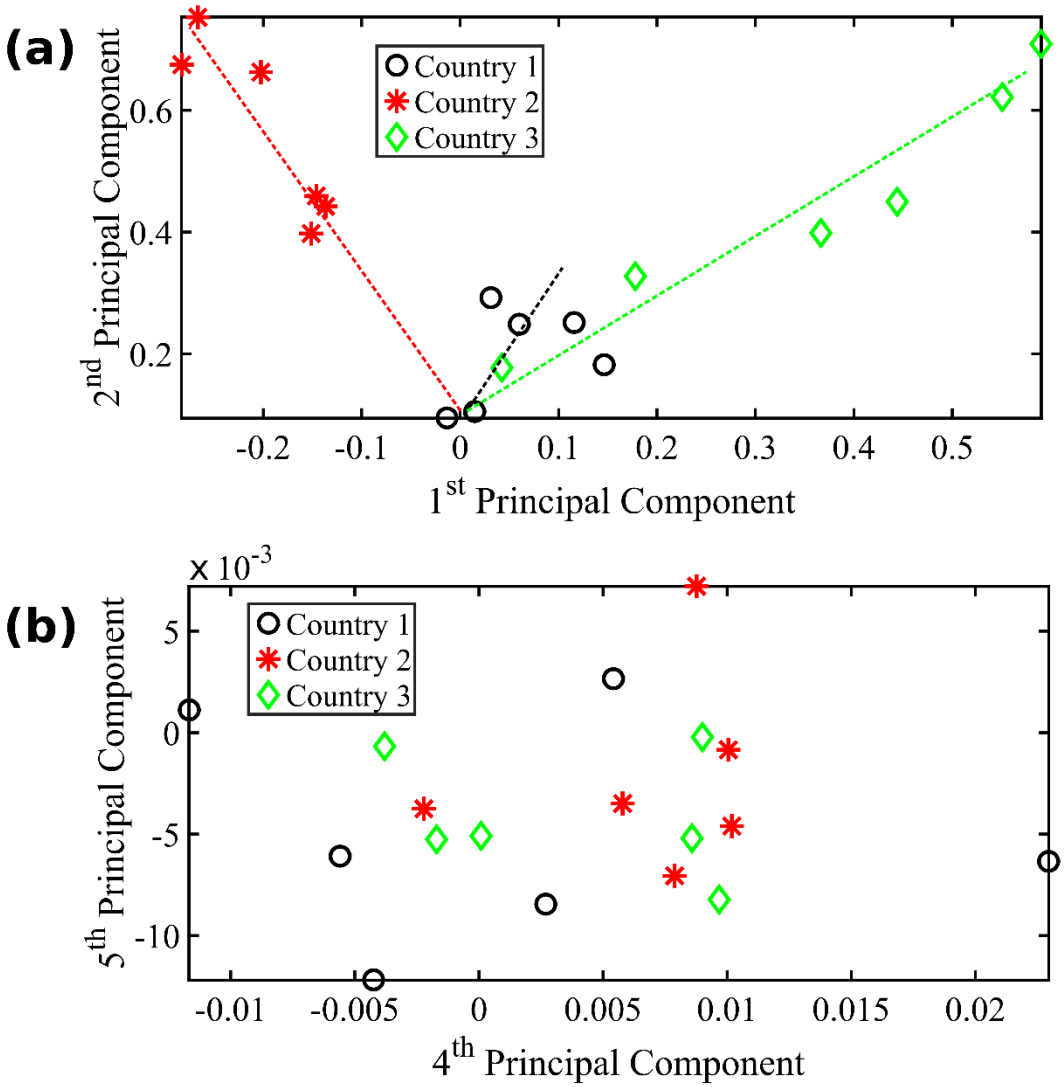

Figure C.4-8: Illustrates the usefulness of PCA analysis. (a) When the data is scatter plotted along the 1st and 2nd principal components, the variation between datasets is discernible. A line, which characterizes a country, can be drawn along data points. The lines drawn in graph are there to guide the eye. Note the 3 different distributions for the 3 different countries. (b) However, in the 4th and 5th principal components no such information is available. Note the difference in axis ranges.

Now, let us imagine that after a year universities have started to move heavily to online video streaming classes. This is a use that is not related to 'browsing' or 'social

interaction', but rather to 'education.' If such a new variable were to be added to the dataset, then we will find that we will need to keep 3 variables to capture 99% of the variation in the dataset. Thus principal component analysis allows us to infer the effective dimensionality of the dataset.

Principal components are relatively easy to find, but the underlying variables or groupings are not easy to interpret. Since the PCA procedure maximizes the amount of variation captured in each principal component, small variation (noise) in the dataset can alter how the weightages are distributed. Therefore the principal components may not necessarily follow the most 'logical' grouping, as is apparent in this example.

How many instances (rows) of data are necessary depend on the noise level. In the case under consideration, the principal component values fluctuate very significantly if dataset used has less than 10 rows.

While performing PCA on a noisy data, one has to keep in mind that the PCA does not distinguish between systematic variation and noise. In cases like those discussed later in this chapter, there needs to be precautions taken to minimize the effects of noise on the analysis.

C.4.4 Experimental Results: Live Cells

Here the goal is to identify different types of cells from their spectroscopic signature. Preparation of metasurface and its characteristics have been described in detail elsewhere (Chapter B.2). Here we only note that samples are made with standard electron beam lithography followed by a metal deposition and liftoff.

We used several different cell lines to perform spectroscopy on. The cell types are tabulated below:

Cell Type	Source
CCD 841	Homo sapiens colon normal (ATCC CRL-1790)
RKO	Homo sapiens colon carcinoma (ATCC CRL-2577)
FaDu	Homo sapiens hypopharynx squamous cell carcinoma (ATCC HTB-43)
A431	Homo sapiens skin/epidermis carcinoma (ATCC CRL-1555)
J774a1	Mus musculus macrophage (ATCC TIB-67

Table C.4-5: List of the cell types used and their sources.

To investigate spectroscopic differences between different cell types, we used different cell lines from humans as well as one from mouse. Two of these cells (CCD 841 and RKO) are from the same organ— colon. The FaDu and A431 cells are from throat and lung tissue, respectively. This allows us to look at the differences between different tissues.

There have been few FTIR studies on these cell lines. Thin tissue section of FaDu has been investigated [188] and compared with HT-29 (human colon adenocarcinoma) cell type using FTIR and positron emission tomography.

We have used anti-EGFR antibody to immobilize these cells on the pixels. The antibody was first deposited using the standard monolayer deposition method described in Chapter C.3. The A431 cell type strongly expresses[189] the EGF receptor. All the other cells used also bind to the anti-EGFR antibody.

Preliminary (Qualitative) Analysis

In the cell spectra (see Figure C.4-6), we note that there are two features (amide I at $1660\ cm^{-1}$ and amide II at $1540\ cm^{-1}$) visible to the naked eye. However, on closer examination a number of other features are revealed. To make the finer features in the

reflectivity spectra clear, we plot the derivative spectra of the pixels in the range of interest (900-1800 cm^{-1}). This makes the signatures of the molecules visible. Next we look at the features appearing for the same cell type consistently across pixels. Some of the features do not appear in all pixels, presumably because of inter-cell (intra-cell-type) variation. The features that appear consistently are noted in table below. We note the features that appear for different cell types and what these resonance frequencies correspond to. This may be used to fingerprint a cell type.

Cell Type	Symm. Phosphate	Asymm. Phosphate	Strained Symm. Phosphate	Asymm. Phosphate	CH_2 Vibr.	C-H Scissor	Amide II	C=O
CCD 841		1060	1200		1365	1450	1525	1740
RKO		1075	1220		1375	1460	1530	1760
FaDu		1040	1180		1385			1750
A431		1035	1205	1295	1380	1445	1530	
J774a1	970	1070			1385	1450	1530	

Table C.4-6: Resonance peaks (in cm^{-1}) observed for various cell lines.

It is easier to distinguish cells of very different types as opposed to cells of similar types, as may be expected. CCD 841 and RKO have almost identical vibrational fingerprint, except some frequency shifts and differences in strengths of peaks.

By examining occurrence of resonance features and their positions, we may interpret the type of cell. For example, the J744a1 cells show a stronger feature around 970 cm^{-1} compared to other cell types. At 1205 cm^{-1} or 1285 cm^{-1} the feature is generally weaker compared to feature for other cell types in the same spectral position. In A431 we see a strong feature around 1280-1290 cm^{-1} which is not usually present in the other types of cells examined. These interpretations are statistical in nature, so in some cells the features may arise, but we only note features that arise consistently for majority

of the pixels. Also, the frequencies noted are from pixels that have their Fano resonance far from these resonances. When the two frequencies are near, the feature tends to move because of mode interaction.

Quantitative[13] Analysis

To analyze how the spectral signatures of different cell species vary quantitatively, we quantified the peak positions, spectral widths, and feature sizes for the dominant eight vibrational lines in our regional of interest. Since different pixels are tuned to different frequencies, field enhancement peaks of bare sensors for different pixels do not coincide in frequency. Only signal from the pixels with very close resonance frequencies are considered for quantitative comparisons between species.

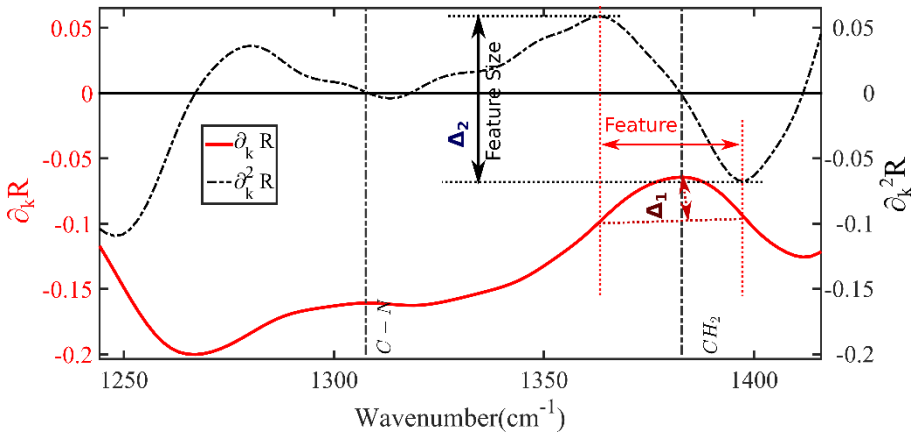

Figure C.4-9: Plot defines 'features' in the measured spectra. The plot shows two figures, a weak feature at 1300 cm^{-1} (C-N bond vibration) and a stronger feature at 1380 cm^{-1} (CH_2 vibration). The derivative spectra (red) and its derivative (black) are shown in arbitrary units. The two 'feature sizes' $\Delta_2 = \Delta\partial_k^2 R$, and $\Delta_1 = \Delta\partial_k R$ are defined in the figure.

[13] The word quantitative here refers to the fact that the feature sizes (Δ_1 and Δ_2) were quantified for further analysis.

For the rest of the analysis I shall focus on the cell types CCD 841, RKO, FaDu and J774a1. Contrasting CCD 841 and RKO is especially interesting because they are both human epithelial cells found in colon, with one (CCD 841) being normal (i.e. non-cancerous), and the other (RKO) being cancerous. Being able to distinguish these two cell types is a key test for the detection method discussed here.

To analyze the large amount of data, we first performed an exploratory analysis where feature sizes (Δ_1) were quantified in $-\partial_k R$ plot (defined in Figure C.4-9), by manually identifying the limits (in k) of the feature. The goal of this analysis was to identify the features that showed (Figure C.4-10) the largest amount of variation, and to this end we employed the method of principal component analysis (PCA) to identify the features or linear combination of features that show the largest variation.

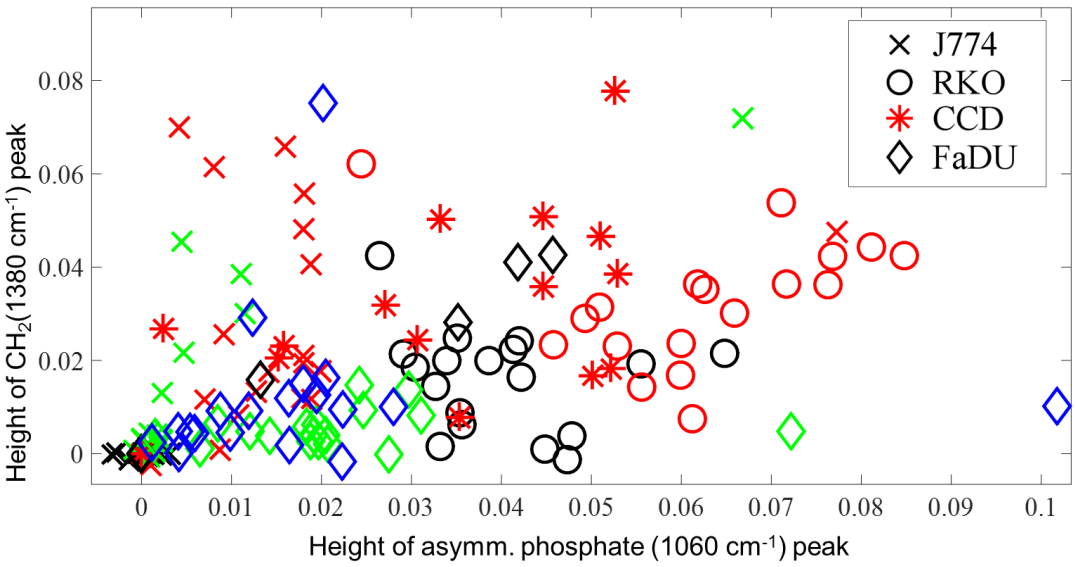

Figure C.4-10: Scatter plot of feature size (Δ_1) of lines 1060 cm^{-1} and 1380 cm^{-1} for different cell types. This is for live experiments. P4 pixels used. The feature sizes were extracted manually. We note that different cell types occupy different areas of the plot.

For the case of the live cells, the largest difference was seen when we scatter plotted the feature sizes of the $1060\ cm^{-1}$ line vs the $1380\ cm^{-1}$ line.

Principal Component Analysis

In order to perform PCA on the manually extracted Δ_1 dataset, we picked one specific pixel, so that all the data from different cell types are taken with sensors of the same resonance frequency. This ensures that the feature sizes are safe to compare between experiments and different cell types. Because the sensors have a Fano-type resonance, the interaction between the cell resonances, and the metamolecules resonance can be quite complicated to analyze, especially without prior knowledge of the position of strength of cell resonances, which we seek. Pixel no. 5 (see Table C.4-1) was picked for this purpose because for pixel 5 the elusive peak at $1740\ cm^{-1}$ is clearly visible but distinct in both RKO and CCD 841. For this pixel signal strengths in the $1200 - 1800\ cm^{-1}$ range is very good.

A matrix consisting of feature sizes (normalized to Amide II) with different rows representing different experimental runs (for the same or different cell types) and columns represent lines of interest. Matlab computes the principal components of the matrix which are the rows. The first few principal components capture most of the variation in the data.

The table below shows values of peak sizes in $(-\partial_k R)$ measured in units of cm for pixel 5.

Peak posn. (cm^{-1})	Peak strength Δ_1 (cm) 970	1060	1220	1300	1380	1450	1540	1740
CCD 841	0.0100	0.0501	0.0336	0.0133	0.0167	0.0146	0.0717	0.130
RKO	0.0067	0.0386	0.0160	0.0030	0.0199	0.0078	0.0371	0.063
FaDu	0.0053	0.0245	0.0234	0.0059	0.0176	0.0059	0.0466	0.076
J774a1	0.0013	0.0073	0.0087	0.0101	0.0070	0.0151	0.0159	0.0336

Table C.4-7: Table of average peak size extracted manually. Experiment performed with P4 pixels.

Peak posn. (cm^{-1})	Peak strength Δ_1 (cm) 970	1060	1220	1300	1380	1450	1540	1740
CCD 841	0.139	0.699	0.469	0.185	0.233	0.204	1.000	1.813
RKO	0.181	1.040	0.431	0.081	0.536	0.210	1.000	1.698
FaDu	0.114	0.526	0.502	0.127	0.378	0.127	1.000	1.631
J774a1	0.0838	0.4606	0.5470	0.6348	0.4412	0.9468	1.0000	2.1107

Table C.4-8: Table of average peak sizes normalized to the peak size at 1540 cm^{-1} (amide II) line. Experiment performed with P4 pixels.

We normalize the data to the peak at 1540 cm^{-1} in order to account for the different coverages for the different cell types. PCA indicates (Table C.4-1) that the 1st eigenmode is dominated by 1380 cm^{-1}, and the second eigenmode is dominated by 1060.

Note that between CCD 841 and RKO Δ_1^{1450} at 1450 cm^{-1} is identical once compensated for Δ_1^{1540}. However, the $\Delta_1^{1300}/\Delta_1^{1380}$ ratio is drastically different between

CCD 841 and RKO. Ratio between $\Delta_1^{1300}/\Delta_1^{1380}$ for pixel 5 is comparable for all 4 experimental runs (Table C.4-8).

We do not see strong correlation between the Amide II and the 1450 cm^{-1} line, which leads us to believe that this line is dominated by the C-H scissor and not Amide III. This is seen in both the correlation coefficient calculated both for an individual sample, and between different types of cells. This is consistent with that the principal components that are dominated by the lines at 1450 cm^{-1} and that at 1540 cm^{-1} are orthogonal in the principal component space.

This, however, includes both intra- and inter- cell type variations. To identify inter-cell type variation, various combinations of these identified vibrational lines are tried. There is a line at 1100 cm^{-1} only for FaDu.

Table below shows principal components calculated from the heights of features at the eight identified spectral locations.

	970	**1060**	**1220**	**1300**	**1380**	**1450**	**1545**	**1740**	%
1st prin. comp.	-0.06	0.10	-0.06	0.11	0.76	-0.62	0	0.07	94
2nd prin. comp.	-0.31	0.84	-0.32	-0.25	-0.01	0.15	0	0.04	98

Table C.4-9: The first two principal components of the data in Table C.4-8. Experiment performed with P4 pixels.

We find that the first 2 principal components account for most variations in the results, which means that these three are enough to distinguish between the four types of cells we investigate in this report.

It is possible to do similar analysis for all the different pixels. Notably, however, since different pixels are tuned to different frequencies, they are sensitive differently to

the different lines. It is therefore not trivial to compare the results from different pixels. Additionally, different batches of samples have some variation in their resonance frequencies. These factors combine to make it difficult to cross-compare results from different pixels, unless the pixels are very closely tuned.

PCA on Automatically Extracted Feature Sizes (Δ_2)

Since the data extraction was manual in this case which is somewhat subjective, an alternative, more objective, strategy for extraction of feature sizes was developed. A feature that looks like a bump in the first derivative will have a more distinguishable signature in the second derivative, as shown in Figure C.4-9. Therefore, an algorithm was developed to look for the sets of peaks and troughs corresponding to a line. The algorithm is used on the second derivative of the reflectivity of sensors ($-\partial_k^2 R$) to identify feature size. The algorithm begins at the expected location of the feature and, looks for the nearest peak in its neighborhood. If the peak is too far ($> 35cm^{-1}$), the algorithm sets the feature size to 0. This is because the feature size may be too small or two convoluted for us to be able to positively identify it. If it does find a peak nearby, it searches for a trough in $-\partial_k^2 R$, and then calculates the difference $\Delta_2 \equiv \Delta\partial_k^2 R \equiv \partial_k^2 R|_{peak} - \partial_k^2 R|_{trough}$. This difference is used as the proxy for feature size. From literature, and manual cross check a largest feature width is checked for. If the reported feature is larger than this in k, then the extracted number is discarded.

We used a script to extract feature sizes (this time Δ_2) at the 9 spectral locations listed in Table C.4-6. The extracted values (shown in Table C.4-10) for pixels 5-8 were picked for further analysis. The reason for picking these specific pixels is that they are spectrally very close (Table C.4-1) . This allows us to increase the dataset and decrease noise. The Δ_2 values were normalized to the mean of all the 9 values.

$$\Delta_{2,norm}^{i} = \frac{9}{\sum_{lines\ of\ interest} \Delta_2^i} \Delta_2^i$$

Peak posn. (cm^{-1})	**970**	**1060**	**1220**	**1300**	**1380**	**1450**	**1540**	**1660**	**1740**
Pixel no.	$\Delta^{i}_{2,norm}$								
5	0.084	0.360	0.882	0.069	1.052	0.855	1.756	3.646	0.297
6	0.157	0.383	0.691	0.282	0.868	1.085	1.984	3.000	0.549
7	0.298	1.083	0.692	0.139	0.627	0.443	2.097	2.406	1.216
8	0.102	0.386	0.824	0.328	0.516	0.738	2.173	3.827	0.107
5	0.320	0.839	0.480	0.300	0.341	0.445	1.632	1.444	2.542
6	0.509	0.430	0.676	0.224	0.774	0.691	1.656	3.878	0.162
7	0.489	0.343	0.912	0.345	0.640	0.867	1.784	2.242	0.791
8	0.261	0.297	0.362	0.257	0.590	1.032	1.205	2.617	2.379
5	0.166	0.244	0.510	0.222	0.691	0.520	1.751	2.515	1.866
6	0.594	0.497	0.993	0.329	0.862	0.784	1.852	1.426	0.956
7	0.078	0.506	0.646	0.038	0.164	0.162	1.299	4.236	1.439
8	0.072	0.734	0.837	0.084	0.976	0.838	1.582	0.113	1.190
5	0.461	0.769	0.493	0.316	0.801	0.918	2.110	2.256	0.875
6	0.178	0.461	0.093	0.534	0.895	0.803	2.005	1.170	1.723
7	0.162	0.346	0.680	0.286	0.447	0.762	2.058	3.196	1.063
8	0.169	0.060	0.583	0.197	0.513	0.824	1.898	3.668	1.088
5	0.262	0.332	0.518	0.225	0.664	0.588	1.508	3.426	1.141
6	0.581	0.254	0.524	0.527	0.561	0.968	0.640	4.242	0.704
7	0.870	0.714	0.366	0.349	0.891	0.698	1.600	2.327	1.185
8	0.051	0.561	0.398	0.271	0.661	1.215	2.057	2.932	0.561
5	0.032	0.193	0.595	0.263	0.290	0.700	2.167	3.568	1.193
6	0.277	0.431	0.678	0.206	0.514	0.606	1.957	3.813	0.518
7	0.076	0.409	0.930	0.303	0.110	0.757	0.626	2.869	1.364
8	0.779	0.578	0.704	0.115	0.328	0.828	2.109	2.479	1.080
5	0.475	0.115	0.017	0.727	0.631	1.334	0.587	0.820	3.249
6	0.475	0.046	0.053	0.689	1.034	0.986	0.500	0.452	4.240
7	0.475	0.864	0.338	0.460	0.419	0.621	1.596	2.840	1.386
8	0.398	0.552	0.296	0.074	0.380	0.378	2.028	2.550	1.793
5	0.234	0.144	0.126	0.762	0.719	1.248	0.484	0.715	3.801
6	0.234	0.128	0.107	0.432	0.913	1.323	0.497	0.824	4.162
7	0.226	0.584	0.452	0.357	0.562	0.242	1.210	2.368	2.998
8	0.108	0.362	0.157	0.390	0.668	0.486	2.064	0.321	3.456
5	0.247	0.091	0.056	0.624	0.576	1.319	0.498	0.733	4.104

Table C.4-10 continued on the next page

Peak posn. (cm^{-1})	970	1060	1220	1300	1380	1450	1540	1660	1740
6	0.247	0.103	0.166	0.562	0.588	0.870	0.572	0.821	4.447
7	0.394	0.361	0.243	0.013	0.774	0.408	1.075	3.007	0.650
8	0.493	0.211	0.562	0.010	0.351	0.366	1.573	1.886	0.537
5	0.308	0.052	0.145	0.462	0.589	1.278	0.388	0.407	2.897
6	0.308	0.100	0.005	0.540	0.650	1.483	0.559	0.792	3.871
7	0.668	0.765	0.224	0.369	0.469	0.245	1.116	4.613	0.532
8	0.535	0.334	0.469	0.055	0.256	0.706	0.860	4.023	1.761
5	0.254	0.523	0.425	0.315	0.712	0.481	1.850	4.065	0.100
6	0.259	0.439	0.407	0.307	0.821	0.497	0.482	4.607	0.038
7	0.282	0.478	0.417	0.139	0.734	0.703	1.914	4.072	0.260
8	0.280	0.444	0.398	0.221	0.359	0.638	0.754	5.319	0.441
5	0.245	0.505	0.280	0.220	0.754	0.324	0.711	5.250	0.618
6	0.075	0.616	0.390	0.161	0.713	0.583	1.283	3.952	0.715
7	0.268	0.365	0.476	0.108	0.726	0.393	1.249	3.712	0.657
8	0.205	0.532	0.310	0.152	0.771	0.648	0.703	4.890	0.452

Table C.4-10: Table shows the extracted dataset ($\Delta^{i}_{2,norm}$) for live cells. The black pixel numbers indicate CCD-type cells. Red stands for RKO and green for FaDU type cells.

We noted earlier that the amide I peak strength is a good predictor of number of pixels in an experiment. However relying on one line to normalize was found to increase the noise level significantly. During data analysis both normalizing to just Δ_2^{1660} and the mean values of all Δ_2 were tried. Using mean Δ_2 for normalization was found to produce more consistent results. Normalization to amide I ($1660\, cm^{-1}$) alone is not the best because in some cases the value of Δ_2^{1660} for has some ambiguity. I checked this by selecting subsets of results and comparing extracted parameters. Also, the largest value of Δ_2 for a given line was removed from further analysis.

The resulting first four principal components capture 38, 61, 77, and 84% of the variation in the dataset. This indicates that the dataset is quite noisy. The principal component matrix is tabulated below

cm^{-1}	**970**	**1060**	**1220**	**1300**	**1380**	**1450**	**1540**	**1660**	**1740**	**%**
1	-0.060	-0.110	-0.016	0.047	-0.302	0.441	0.763	0.321	-0.105	38
2	-0.039	-0.052	-0.155	0.806	0.205	0.428	-0.276	0.070	-0.125	61
3	0.033	-0.152	-0.069	0.011	-0.016	-0.294	-0.215	0.902	0.158	77
4	-0.033	-0.070	-0.121	0.082	0.058	0.132	0.108	-0.119	0.962	84

Table C.4-11: The first four principal components of automatically extracted Δ_2 are shown as rows. Columns 2-10 show the column multipliers. The last column shows the percentage of the total variation of the dataset captured cumulatively.

The dataset was transformed to the principal component basis, and the first two principal components were scatter plotted (Figure C.4-11). In this case the different cell types are not very well distinguished. Possibly due to the large amount of variation in the state the cells are found in.

Note that in the manually extracted data the cell types are better separated (Figure C.4-10). The reason for this could be that the manual extraction of data benefits from a number of consideration by the analyst that the script (as is) does not benefit from. For example, the width of a feature is better resolved in some pixels than in others. When extracting data from a pixel where it is not very well resolved, I benefit from looking at a pixel where it is well resolved. The script on the other hand treats each pixel and each line separately and makes no refinement based on these consideration.

We shall find later that the fixed cells are better resolved in the automated data extraction procedure.

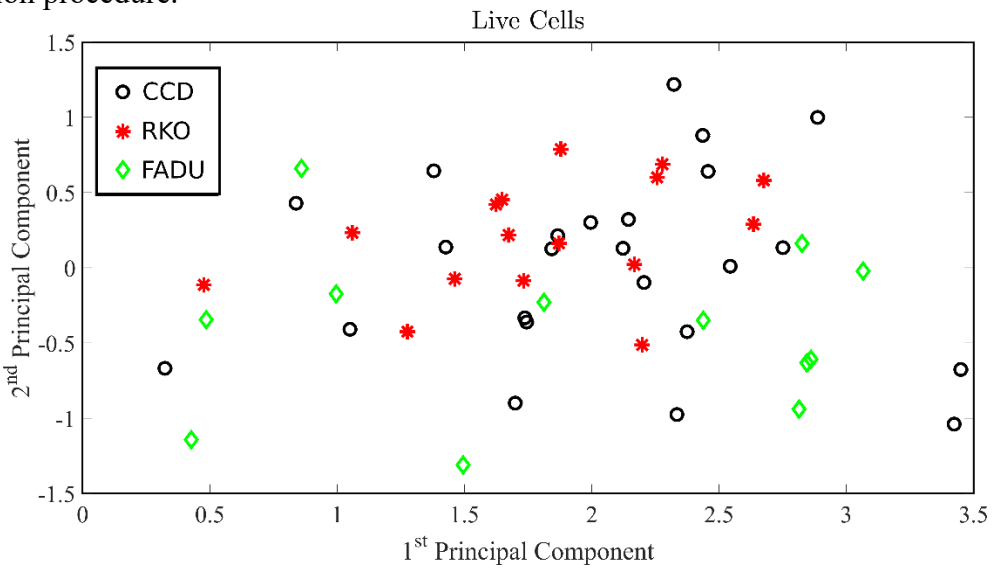

Figure C.4-11: Scatter plot of the 1st and 2nd principal components for the dataset in Table C.4-10. RKO cells show the smallest variation, and FaDU the largest. On the whole, however, the live cells are not very well distinguished in the automatically extracted data from P4 pixel experiments.

In summary, we deposited live cells on sensor pixels and took the spectra of the live cells. The spectra was then analyzed to identify and quantify the dominant absorption features in the cell. We performed a principal component analysis of results from one particular pixel (pixel 5). After finding that the principal components are dominated by individual lines, we scatter plotted the distribution of these lines and identified differences in different cell types. Note that to identify a cell type, one needs to perform a statistical analysis. We would prefer to have a spectral marker to identify a single cancerous cell. We are working towards that goal.

C.4.5 Experimental Results: Fixed Cells

The experiments were performed in similar geometry- with cells on sample array. The samples with fixed cells were prepared and deposited as described before.

Fixing a cell causes the cell components to be immobilized in its last state. This allows for a more controlled experiment as opposed to live cells where the cell condition changes with time. In our case, fixation had another benefit—it enhanced signal from vibrational lines. Presence of water dampens the signal from the vibrational lines of interest. Fixing the cell allows us to dry these cells so that these fingerprints become more prominent. There is some water molecules left even in dry fixed cells, however, as evidenced by their (albeit diminished) spectral signature at $1670\ cm^{-1}$. These are presumably water molecules that are hydrogen bonded with other molecules in the cell.

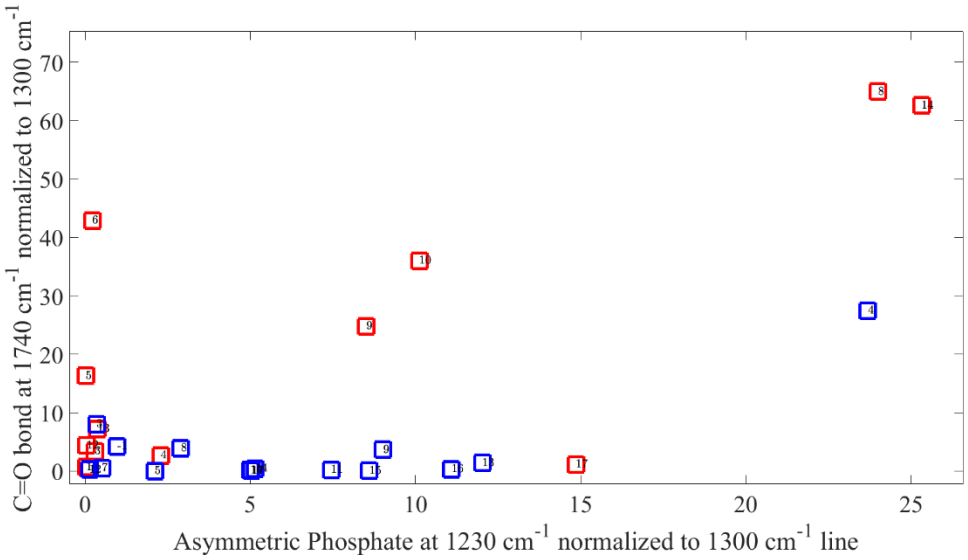

Figure C.4-12: Change of feature strength (Δ_2^i) for the vibrational lines at $1230\ cm^{-1}$ and $1740\ cm^{-1}$ after fixation. Red squares are for live cells, blue for fixed. Experiment performed with P4 pixels. We find that Δ_2^{1740} is weaker after fixation in acetone.

Similar analysis as before (for live cells) was performed for the fixed cell data. We would mainly focus on the automated analysis for this part. The script described above (in `Data Analysis') was used to extract cell parameters.

We found that there is one clear distinguishing feature between CCD 841 and RKO that is very well reproduced. The $C = O$ bod stretch mode ($1740\, cm^{-1}$) is consistently expressed in pixel 3 for CCD, but not for RKO (see Figure C.4-13 and Figure C.4-14). It is difficult however, to go through all the pixels and find markers like this manually. A better strategy is to automate the data analysis.

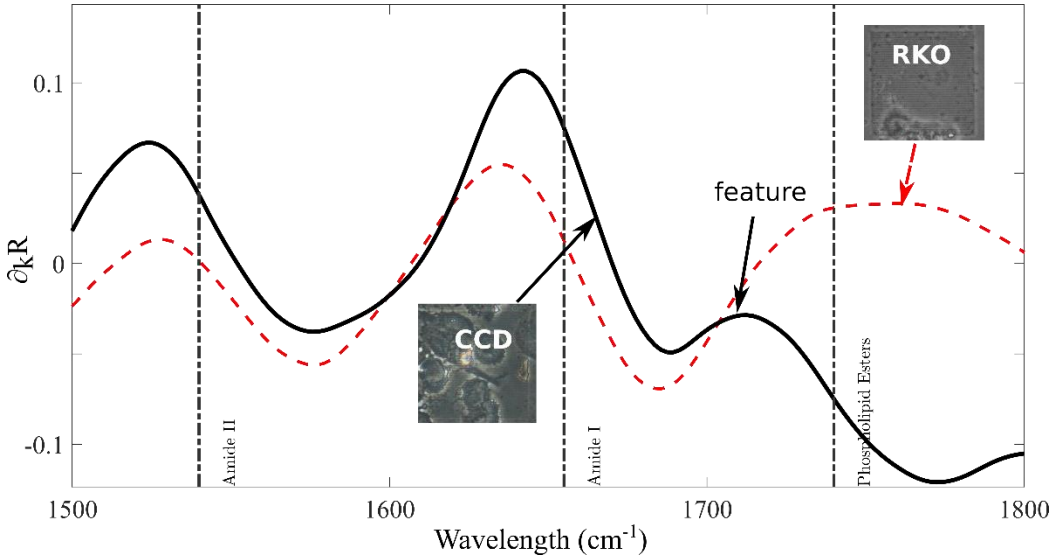

Figure C.4-13: Distinguishing feature between CCD 841 and RKO cell lines. For CCD, there is a feature visible for P4 pixel 3 at $1740\, cm^{-1}$ that's not seen in the case of RKO. This is repeatable in experiments (Figure C.4-14 has another example). This distinction is only clear for pixels 2 and 3. For other pixels, the distinction is not clear.

The spectra were analyzed with Matlab script to find the feature sizes (Δ_2) and then the dataset was normalized as explained before. Finally, a principal component analysis was performed on the data.

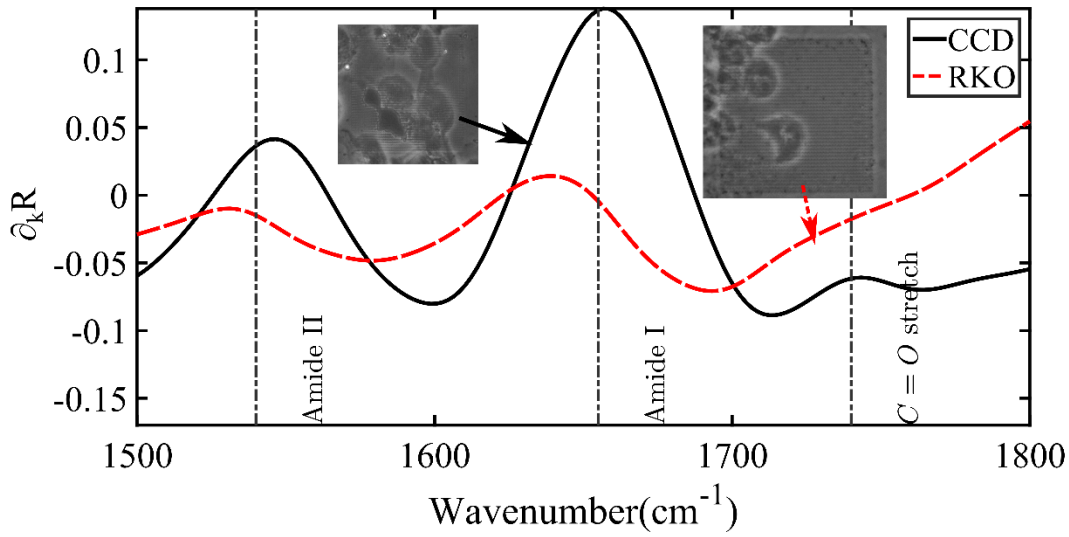

Figure C.4-14: Distinguishing feature between CCD 841 and RKO cell lines, second example. Experiment performed with P4 pixel 3.

To perform the PCA analysis, the pixels 5-8 were picked, as before because of their spectral proximity. The data was normalized with the average value of Δ_2 for all the lines for a given dataset of 9 molecular vibrational lines corresponding to each pixel.

Peak posn. (cm^{-1})	**970**	**1060**	**1220**	**1300**	**1380**	**1450**	**1540**	**1660**	**1740**
Pixel no.	$\Delta^{i}_{2,norm}$								
5	0.186	0.567	0.538	0.114	0.476	0.643	0.829	2.735	1.077
6	0.631	0.690	0.296	0.215	0.443	0.431	1.731	1.921	1.161
7	0.225	0.462	0.719	0.373	0.900	0.721	1.613	2.983	1.004
8	0.587	0.615	0.029	0.467	0.744	0.806	1.800	3.506	0.445
5	0.643	0.551	0.241	0.336	0.819	0.782	1.030	1.717	2.139
6	0.927	0.922	0.418	0.615	0.311	0.989	0.982	2.207	1.249
7	0.010	0.586	0.786	0.407	1.009	1.088	0.857	3.405	0.851
8	0.472	1.693	0.631	0.380	0.689	0.557	1.190	3.405	2.388
5	0.434	0.734	0.106	0.533	0.966	0.806	1.313	3.007	0.334
6	0.326	0.877	0.182	0.182	0.707	0.628	2.274	3.269	0.194
7	0.061	0.609	0.516	0.171	1.028	0.897	1.211	3.014	1.493
8	0.623	0.360	0.267	0.427	0.673	0.635	1.622	3.115	1.280
5	0.158	0.414	0.577	0.251	0.882	0.822	1.345	3.661	0.889
6	0.783	1.434	0.566	0.484	0.715	0.822	0.867	2.971	0.181
7	0.111	0.360	0.269	0.110	0.607	0.412	1.390	3.861	0.934
8	0.275	0.463	0.304	0.419	0.661	0.974	1.697	2.769	1.438
5	0.377	0.566	0.012	0.359	0.891	0.921	1.495	3.342	1.037
6	0.302	0.721	0.116	0.349	0.667	1.125	1.895	3.385	0.126
7	0.339	0.413	0.550	0.364	1.012	0.566	0.181	3.245	1.004
8	1.035	0.056	0.703	0.237	0.457	0.505	0.634	4.531	0.842
5	0.674	0.586	0.610	0.406	0.317	0.411	0.318	4.566	1.112
6	0.088	0.540	0.584	0.234	0.701	0.813	2.089	3.830	0.122
7	0.334	0.330	0.239	0.293	0.553	0.695	1.848	3.351	1.357
8	0.055	0.534	0.401	0.337	0.375	0.975	2.215	2.753	1.354
5	0.363	0.645	0.243	0.334	1.240	0.917	1.372	3.562	0.323
6	0.553	0.555	0.569	0.399	1.347	0.876	1.022	2.393	1.285
7	0.440	0.624	0.553	0.144	0.754	1.019	1.663	3.158	0.240

Table C.4-12 continued on the next page

Peak posn. (cm^{-1})	970	1060	1220	1300	1380	1450	1540	1660	1740
8	0.736	0.183	0.221	0.446	1.295	0.634	1.638	1.879	1.968
5	0.503	0.652	0.447	0.282	1.201	0.748	1.266	3.171	0.731
6	0.688	0.449	0.799	0.347	0.876	0.907	1.523	2.464	0.374
7	0.552	0.521	0.053	0.389	0.507	0.623	1.513	2.818	1.067
8	1.027	0.537	0.701	0.321	1.150	0.831	1.659	2.818	1.469
5	0.382	0.355	0.546	0.290	0.839	0.411	1.843	3.718	0.615
6	0.202	0.796	0.594	0.361	1.193	0.705	1.281	2.808	1.060
7	0.208	0.734	0.856	0.454	0.461	0.910	1.563	2.111	1.007
8	0.503	0.578	0.804	0.466	0.454	0.903	0.543	3.039	0.575
5	0.033	0.711	0.596	0.182	0.109	0.601	2.024	2.948	0.767
6	0.581	0.297	0.686	0.266	0.744	0.621	1.625	3.049	1.132
7	0.273	0.589	0.510	0.089	0.792	0.818	1.758	3.183	0.314
8	0.401	0.492	0.264	0.057	0.487	0.890	2.016	3.027	1.365
5	0.315	0.215	0.775	0.329	1.355	0.911	0.352	3.817	0.930
6	0.315	0.215	0.775	0.329	1.355	0.911	0.352	3.817	0.930
7	0.223	0.147	0.089	0.411	0.709	0.801	0.847	1.874	0.960
8	0.451	1.071	0.691	0.431	0.401	1.861	0.650	3.170	2.152
5	0.340	0.931	0.462	0.619	1.272	1.322	0.871	2.698	0.484
6	0.340	0.931	0.462	0.619	1.272	1.322	0.871	2.698	0.484
7	0.340	0.931	0.462	0.619	1.272	1.322	0.871	2.698	0.484
8	0.838	0.565	0.663	0.281	0.928	1.574	1.152	1.677	1.324
5	0.511	0.692	0.442	0.421	0.808	0.765	0.511	3.799	0.640
6	0.511	1.103	0.442	0.421	0.808	0.765	0.511	3.799	0.640
7	0.511	1.103	0.442	0.421	0.808	0.765	0.511	3.799	0.640
8	0.517	0.579	0.590	0.375	0.529	1.719	0.640	1.911	2.140
5	0.477	0.630	0.828	0.315	0.619	0.447	0.564	3.121	0.345
6	0.239	0.352	0.560	0.236	0.946	0.855	1.101	3.606	0.151
7	0.220	0.299	0.320	0.297	0.771	0.779	1.279	4.214	0.820
8	0.451	0.901	0.424	0.489	0.877	1.125	1.571	1.588	0.199

Table C.4-12: Table shows the extracted dataset ($\Delta^{i}_{2,norm}$) for fixed cells. The black pixel numbers indicate CCD-type cells. Red stands for RKO and green for FaDU type cells.

The resulting first two principal components capture over 90% in the variation in the data, which is drastically better than the case with live cells. The reason for this is possibly that the fixed cells are not undergoing compositional and chemical changes. The large fluctuation in the amount of water present in live cell experiments take a toll on reproducibility of data.

If we scatter plot the first two principal components, we observe that the cell types are better resolved than with the live cells.

cm^{-1}	**970**	**1060**	**1220**	**1300**	**1380**	**1450**	**1540**	**1660**	**1740**	**%**
1	0.00	0.01	-0.10	-0.20	-0.22	0.77	-0.21	0.49	-0.14	77
2	0.05	0.11	0.10	-0.43	-0.29	0.18	0.77	-0.28	-0.10	91
3	0.07	0.16	0.00	0.01	0.64	-0.03	0.45	0.57	0.17	95
4	-0.07	-0.06	-0.07	0.17	-0.20	0.21	0.08	-0.08	0.93	97

Table C.4-13: The first four principal components of automatically extracted Δ_2 are shown as rows. Columns 2-10 show the column multipliers. The last column shows the percentage of the total variation of the dataset captured cumulatively. Note that the first two principal components alone capture 91% of the variation in the data.

At a casual glance, it may appear that pixel 3 would be a good choice for cell distinction, and here I would remind the reader that the data analysis looks at several lines for several pixels for different cell types. One feature that is discovered by an observer will not be statistically significant enough to be picked up by the principal component analysis.

The procedure to distinguish cell types from experimental data, first a dataset of Δ_2 needs to be extracted for the 9 lines of interest. The data needs to be in a $n \times 9$ matrix

where each row corresponds to one individual pixel (on the same wafer or not). This data will need to be transformed with the principal component matrix with a simple matrix multiplication. By comparing the distribution of the dataset in the plot one may be able to infer the cell type.

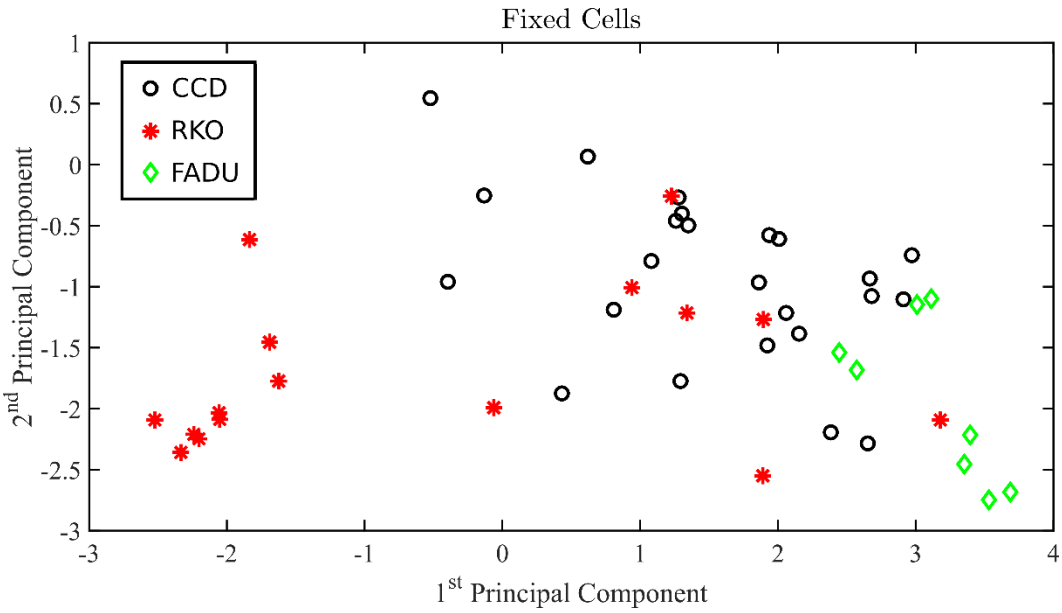

Figure C.4-15: Scatter plot of the 1st and 2nd principal components for the dataset. The different cell types occupy different parts of the plot, even though there is a large variation within a cell type. The CCD cells occuply the central area, whereas the FaDU and RKO cells occupy bottom right and left corners, respectively.

When the principal components of the dataset (Table C.4-12) is calculated and plotted, we find that the three different cell types in question are well distinguished (Figure C.4-15). The three different cell types occupy different regions in the two dimensional plot of the first two principal components as axes.

One question that lingers is whether a learning algorithm may be applied in this case that will be able to find a marker like that in Figure C.4-13 to easily distinguish two cell types.

C.4.6 Determining Cell Coverage

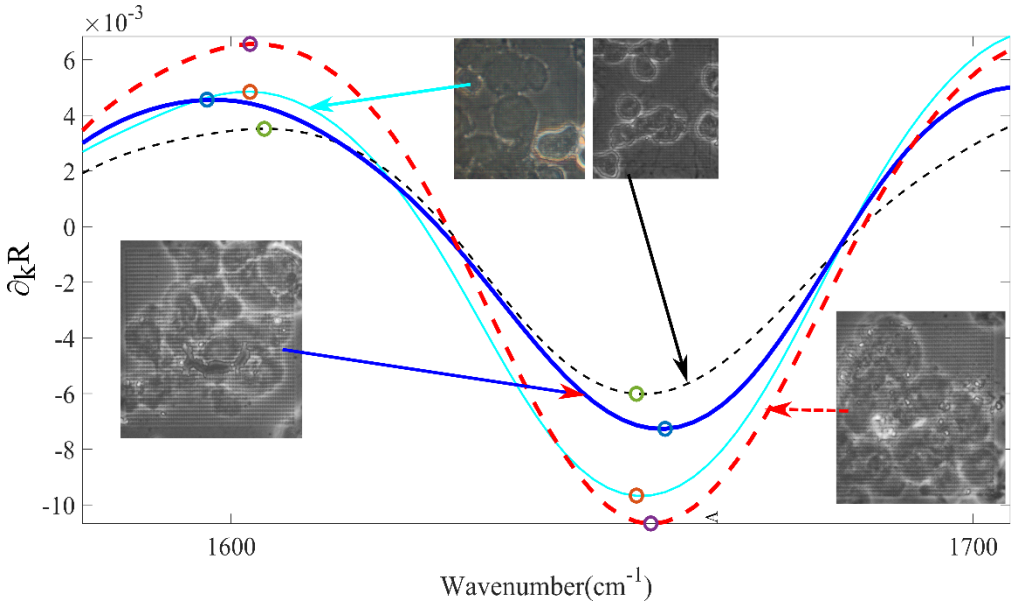

Figure C.4-16: Relation between cell coverage and signal strength (Δ_2^{1660}) at $1660\ cm^{-1}$ line for live (CCD 841) cells on pixel 7. Note that higher coverages generally lead to higher signal strength. Experiment performed with P4 pixels.

As the cell deposition process is a stochastic process, some pixels get more cell coverage and some get very few. To analyze the data reliably, we need to understand the effect of cell coverage on signal strength (Δ_1 or Δ_2) and normalize the data to compensate for such fluctuation in cell coverage.

Effect of Cell Coverage on Δ_2^{1660}

We can see from Figure C.4-16 that an increased coverage does in general lead to stronger signal strength at $1660\ cm^{-1}$, but it is not a foolproof predictor of number of

cells, at least in the case of live cells. The reason might be that there is weak control over the amount of water present near the cell. We will see that for fixed cell this relation to be stronger, as we expect due to the fact that the water content of a fixed cell does not fluctuate.

The cell deposition is a stochastic process. At the same time, the signal strength is a function of two factors: the sensitivity of the detector at the wavenumber of interest and the density of analyte (i.e. cell coverage). There are two ways to identify the cell coverage- the first involved taking image of each of the pixel and performing image analysis using a software. Even though this is simple in principle, it will add complexity to the final device, and is preferable to avoid. A better approach is to find a way to extract cell coverage from the spectra itself. It turns out that the feature near amide I is a very good indicator of cell coverage (see Figure C.4-17). For a given pixel (pixel 7 in Figure C.4-17), the signal strength at $1660\ cm^{-1}$ increases with cell coverage. This relationship is valid for live cells as well.

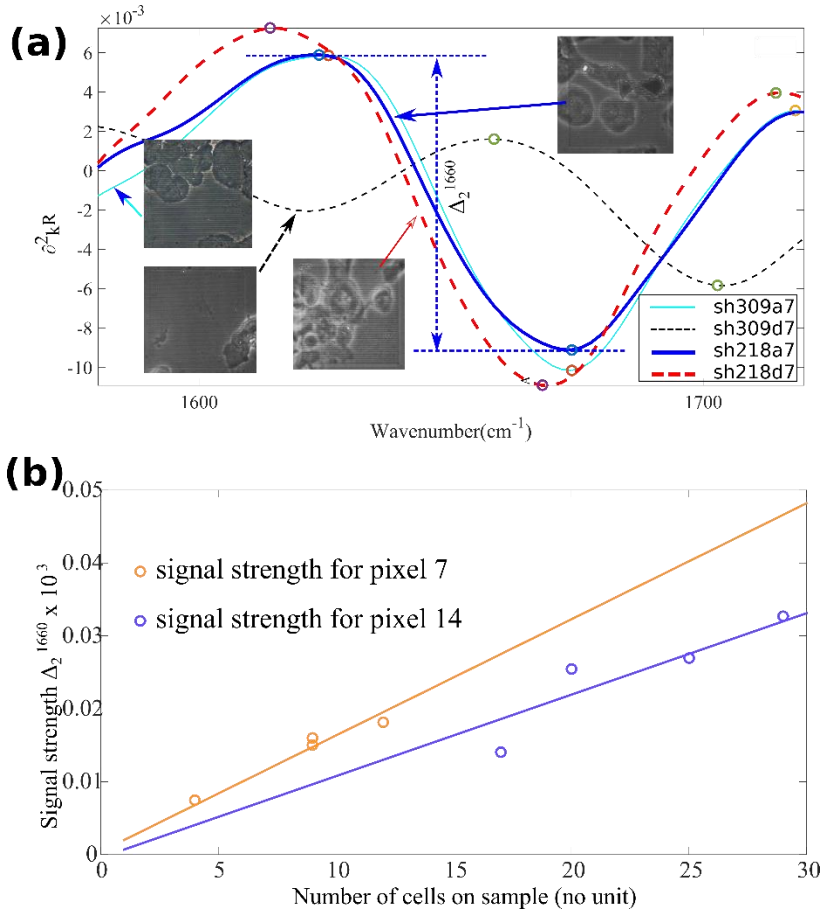

Figure C.4-17: Comparison between signal strength ($\Delta\partial_k^2 R$) at 1660 cm^{-1} and coverage[14] for fixed CCD841 cells on P4 pixel 7. (a) The signal strength increases with increase in number of cells. The pixel number 7 is used here as an example showing low and moderately high coverage. The figure shows the signal strength for one of the cases. Inset figures show the images of the pixels to illustrate the cell coverage. (b) Shows plots of signal strength against cell coverage. We call the slope of the fitted curves 'sensitivity' of the pixel. The point (0,0) was added to the data for the purpose of the fit because we expect the signal strength to be very small when there are no cells present.

This allows us to normalize data to compare different sets of experiment where coverage is very different. Presumably after a uniform coverage has been achieved, the

[14] Data from experiments sh160218 and sh160309.

signal strength will saturate— because the pixels are only sensitive to analytes within about a 100 nm of the metasurface.

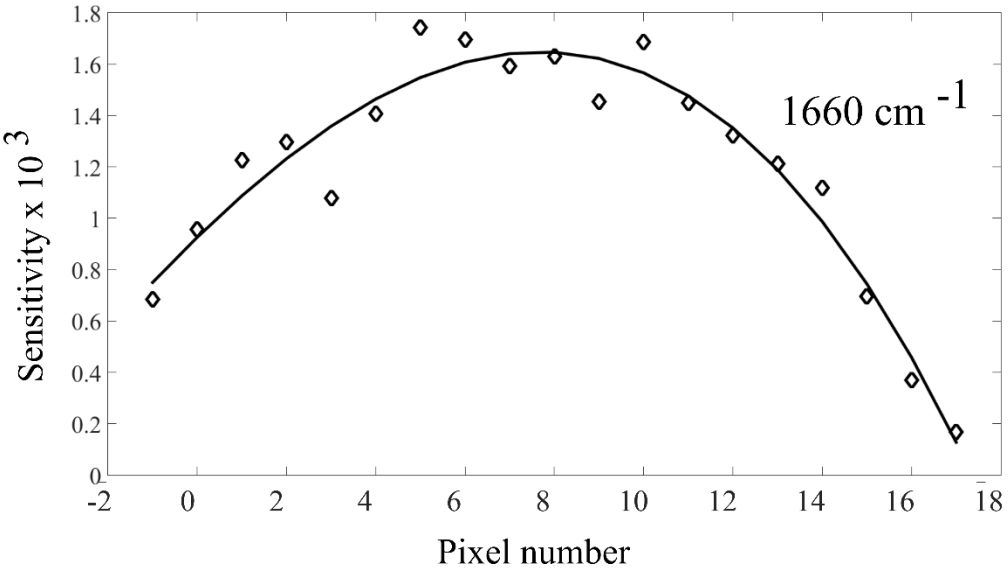

Figure C.4-18: Shows sensitivity($\psi = \frac{\Delta_2}{n}$) of a pixel for the 1660 cm^{-1} line as a function of the pixel number. This curve justifies our comparisons of data for the same pixel across different experiments with unequal number of cells.

Since each pixel is tuned to a different frequency, it is expected that in general, pixels tuned closer to the amide I resonance will have larger signal strength for the same number of cells. Indeed, when we plot (Figure C.4-18) the sensitivity ($\psi = \Delta_2/n$) where n is the number of cells on a pixel, we note that the sensitivity is the highest in the neighborhood of pixel 8.

Data Normalization

When normalizing data, we did not use Δ_2^{1660} alone (the feature size at 1660 cm^{-1}) to normalize other vibrational lines. The reason for this is that any error in extracted Δ_2^{1660} affects all lines (Δ_2^i).

Now, the logic behind normalizing to the Δ_2^{1660} is that all feature sizes (Δ_2^i) would be proportionally dependent on the cell coverage. By the same logic, it is reasonable to normalize Δ_2^i to the sum of all feature sizes, i.e.

$$\Delta_{2,norm}^i = \frac{9}{\sum_{lines\ of\ interest} \Delta_2^i} \Delta_2^i$$

The factor 9 in the numerator arises because there are 9 lines of interest. This normalization procedure was used in the data analysis above. The advantage of using this normalization procedure is that in this procedure is more robust against error in extracted Δ_2.

Effect of Cell Coverage on Fano feature

A metasurface resonance is a collective effect[150,190,191]. How many unit cells are important for a collective resonance to emerge depends on the unit cell structure. For antenna arrays, there is more in-plane interaction in the direction perpendicular to the antennas. For the dielectric pi structure[191] a 5×5 array of unit cells give rise to collective effects. For the metasurface we have used for this study, an array of 3×3 unit cells is thought to give rise to a collective Fano feature.

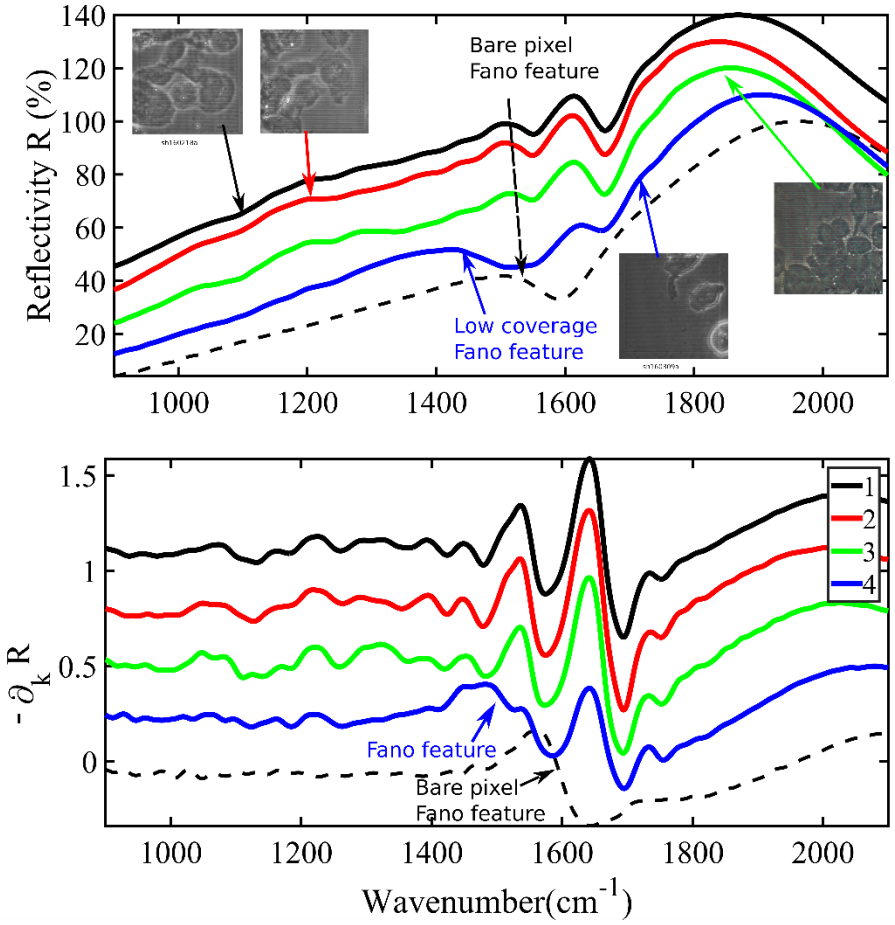

Figure C.4-19: Shows the evolution of prominence of Fano feature with cell coverage of pixels for a few experimental runs with P4 pixel 11 and fixed cells of type CCD 841. (a) The Fano feature weakens as the cell coverage increases, apart from an expected redshift. Here data for the same pixel (pixel 11) are collected for four different experiments. The dashed curve shows bare spectra. All spectra are normalized so the dipole peak is 100%. The spectra are also vertically shifted to make the plot readable. (b) In derivative spectra, the Fano feature is seen to be redshifted by about 100 cm^{-1}, which is less than expected redshift (200 cm^{-1}) seen when the pixel 11 is immersed in water (see Table C.4-1).

We noticed a weak dependence on the prominence of the Fano feature (see Figure C.4-19). As the cell coverage increases, the prominence of the Fano feature as seen in reflectivity diminishes. The Fano feature, in general, became weaker as cell coverage went from 1-2 cells to 20-30 cells in the analyzed region ($100\mu m \times 100\mu m$ area from

which spectra was collected). This is true for both reflectivity spectra and the derivative spectra. For small coverage the peak corresponding to the Fano resonance is redshifted. For moderate coverage, the prominence of Fano feature is not predictable solely from coverage. For large coverages the Fano feature is difficult to discern.

The reason for such behavior is that for the metasurface unit cells covered with cells the dipole and quadrupole frequencies (k_Q, and k_D) are redshifted (by δk_i, where $i = Q, D$). The dipole resonance is a broad ($\delta k_D \ll k_D/Q_D$, where $Q_D \sim 3$ is the quality factor of the dipole resonance) and as a result the spectra remain similar with an overall redshift. For the quadrupole resonance, however, the shift is comparable to the width ($\delta k_Q \sim k_Q/Q_Q$, where $Q_Q \sim 10$ is the quality factor of the quadrupole resonance) of the quadrupole resonance.

We take pixel 14 as an example. Note from Table C.4-1 that the Fano resonance (k_Q) shifts by $k_Q^{dry} - k_Q^{H_2O} \approx 190\, cm^{-1}$ when the pixel is immersed in water. From Chapter B.2 we know that pixel P4 has a quality factor of $Q \approx 10$, i.e. a linewidth $\frac{k_Q}{Q} = 150\, cm^{-1}$. Since cell has slightly greater refractive index than water, we expect that when portions of the metasurface is exposed and parts of it is covered by cells, that the Fano resonance will be 'washed out' for moderate high cell coverage.

C.4.7 Conclusions and Outlook

In this chapter we discussed spectroscopy of live and fixed cells and characteristics of the spectra, and the challenge of distinguish different cell types. We have demonstrated that it is possible to distinguish cell types using spectroscopy.

The algorithms in use in this section needs to be further refined to make the predictive model better than it is now to do spectroscopic distinction with fewer cells.

We have also successfully demonstrated (Appendix D.2) cell attachment to the DEP electrodes. We also acquired spectra from the cells on the sensor pixels.

It is harder than it might seem to compare cell spectra from different pixels with different resonance frequencies because different pixels interact with molecular lines differently. The number of pixels with different resonance frequencies is relatively large (~10) and they do not offer an easy way to cross-compare. Therefore, it may be worth exploring the possibility of using just a few (~2 or 3) resonance frequencies and repeat these pixels in experiments. This allows us to do more statistical analysis without modeling the effects of having differently tuned resonance frequencies.

The next logical step is to demonstrate separation of different cell types. The idea is to stain one or both types of cells with a dye so the type may be confirmed with microscope, and then introduce both types into the same suspension and use DEP to separate the two cell types. We can then move on to real blood sample. In the blood sample experiments, the RBCs will have to be removed first, so that the selection efficiency requirement for the DEP is lower. Also, DEP performs better with fewer particles in suspension because large number suspended particles modify and screen the DEP field.

One hopes that at the successful conclusion of this and other studies we have a working design which will save millions of lives.

SECTION D : APPENDICES

Appendix D.1: Dielectric Pi Structures[15]

Metasurfaces represent a versatile platform for light manipulation, sensing of both organic and inorganic matter, nonlinear optics, and various other applications. Metasurfaces generally rely on resonant structures to achieve engineered optical properties like high spectral selectivity, unlike photonic crystals which rely on periodicity.

Most metasurfaces are metal-based, and as a result their spectral selectivity is severely limited by plasmonic loss. Using dielectric material, however, leads to a significant reduction of the plasmonic loss. Here we present a Si based metamaterial that shows high spectral selectivity ($Q > 100$), and is CMOS compatible. These metasurfaces are shown to possess extreme planer chirality, opening exciting possibility for efficient ultrathin narrowband circularly polarized thermal light emitters.

Metasurfaces were the first to find practical applications at optical frequencies ranging from light manipulation[78,91,192–194] and sensing of minute analyte quantities [8,35,50] to nonlinear optics[195,196], spectrally selective thermal emission[197] and even low-threshold lasing[198]. Many of these applications require photonic structures characterized by their highly spectrally selective response (corresponding to high-quality factor Q), miniaturized format (preferably on the scale of no more than several wavelengths) and

[15] The work in this chapter is based on a collaboration with coauthors in [191]. Wu performed the simulations and the theoretical analysis. Arju, Fan, Dominguez, and Gonzalez performed the fabrication. Arju and Kelp acquired the spectra. Arju performed some of the simulations. Wu and Shvets wrote the paper. Tutuc, Brener and Shvets supervised the work. Shvets conceived the project.

the convenience and high efficiency of far-field light coupling. The coupling efficiency issue, while seemingly mundane, is particularly important for mid-infrared applications because of the lack of ultrasensitive optical detectors in that frequency range.

Simultaneously satisfying these requirements presents considerable challenge for most photonic structures. For example, the isolated high-Q microcavities reviewed in ref. [199] and suggested for biochemical sensing applications[10,200] suffer from poor far field coupling[201,202]. Planar photonic crystals are also known to possess extremely spectrally selective optical responses (for example, reflection and transmission amplitudes or phases)[92,203,204] that have been exploited for various sensing[7,92,205] and filtering[203] applications. The very high-quality factors[206] $Q > 1000$ of such photonic resonances are often caused by the so-called guided resonance modes (GRMs)[203,207]. The spectrally narrow linewidth of these modes originates from the suppression of their radiative losses through the long-range destructive interference between multiple unit cells of a photonic crystal and, therefore, is extremely sensitive to the light's incidence angle[92,203,204,206,208,209]. Such angular sensitivity prevents miniaturization of photonic crystal devices[203,205,210] and imposes severe restrictions on the angular divergence of the incident light beams. While highly collimated laser beams have been used for interrogating high-Q photonic crystal structures in the visible and telecommunication spectral ranges[7,205,209,211], the angular divergence of incoherent beams used for mid-infrared spectroscopy is typically prohibitively high for utilizing GRMs supported by photonic crystals. Note that high angular sensitivity is also typical for the frequency-selective surfaces[212] that can be thought of as microwave predecessors[1] of metasurfaces.

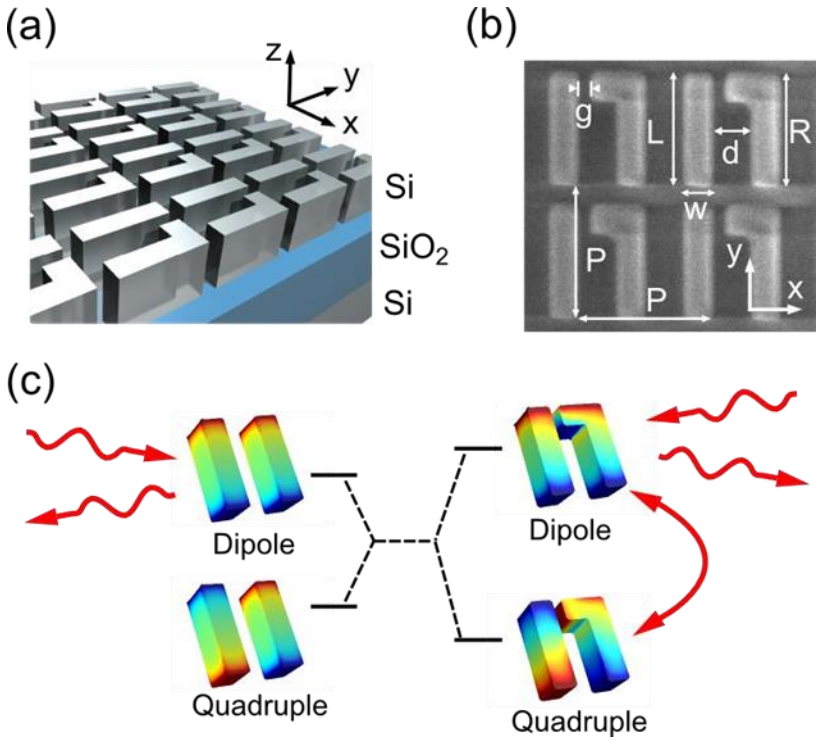

Figure D.1-1: Fano-resonant silicon metasurfaces. (a) A schematic of the silicon-based chiral metasurface supporting high-Q Fano resonances. (b) The SEM image of the fabricated sample and geometry definitions. Physical dimensions: $P = 2.4\mu m$, $w = 500nm$, $d = 700nm$, $g = 200nm$, $R = 2\mu m$, and $1.6\mu m < L < 2\mu m$ for the three samples that differ in L. (c) A schematic illustrating the Fano interference between electric dipolar (top left) and quadrupolar (bottom left) modes due to the symmetry-breaking small horizontal stub. The plotted color-coded surface charge distributions $4\pi\sigma = \left(\vec{\boldsymbol{E}}_{air} - \vec{\boldsymbol{E}}_{Si}\right).\vec{\boldsymbol{n}}$ at the Si/air interfaces are calculated from eigenvalue simulations of the fields supported by the metasurface. The modes approximately retain their spatial symmetry after hybridization.

Metasurfaces avoid these limitations by employing a conceptually different design approach: its unit cell and its neighboring interactions are engineered to reduce the combined radiative and non-radiative (i.e., Ohmic) losses of the sharp resonances. Here the radiative losses are reduced by engineering the detailed geometry of the metasurface unit cells, while the non-radiative losses are reduced by judiciously selecting the unit cell material. One promising approach to decreasing radiative losses while maintaining finite

coupling to free-space radiation is to utilize the phenomenon of Fano interference[44] originally introduced in atomic physics to describe asymmetrically shaped ionization spectral lines of atoms. More recently, the concept of Fano resonances was introduced to the field of photonics and metamaterials[46–48,104,206,207] in which a photonic structure possesses two resonances generally classified as 'bright' (that is, spectrally broad and strongly coupled to incident light) and 'dark' (spectrally sharp, with negligible radiative loss). The weak nearfield coupling between the bright and dark resonances leads to coupling of the incident light to the dark resonance that maintains its low radiative loss, thereby remaining high-Q.

Unfortunately, even for the most judicious engineering of the radiative loss, the total Q is limited[41,49,198,213] by the non-radiative loss of the underlying material. A notable exception is the special class of diffraction-coupled plasmonic arrays[190,204,214,215], which rely on the geometric resonance that arises when the wavelength of light is commensurate with the array's periodicity[215]. Such plasmonic arrays can possess a very high Q-factor, but suffer from the same limitations as GRM-based photonic crystals, affecting a number of important applications that involve ultra-small (several wavelengths in size) samples. A typical example of such application is an infrared absorption sensor capable of resolving proteins' secondary structure, which would require mid-infrared metamaterial resonances with $Q{\sim}100$ to distinguish between their alpha-helical and beta-sheet conformations[216] that fall inside the Amide I and II ($1{,}500\ cm^{-1} - \ 1{,}700\ cm^{-1}$) range. An Equally important practical consideration is that the noble metals used for making high-Q plasmonic metasurfaces cannot be processed at CMOS-compatible fabrication facilities, thus limiting their scalability and standardization.

One approach to reduce non-radiative losses without utilizing diffractive effects is to substitute metallic metamaterials by dielectric ones. Although the electromagnetic properties of dielectric resonators have been studied for decades[217–219], all dielectric infrared metamaterials have only recently been demonstrated[193,220–223], and other non-metallic materials are being considered[224]. Despite this body of work, experimentally demonstrating sharp metamaterial resonances ($Q{\sim}100$) has proven to be challenging, thus greatly impeding further progress in applying metamaterials to practical problems such as biochemical sensing.

Here we present an experimental realization of silicon-based infrared metasurfaces supporting Fano resonances with record high quality factors $Q > 400$. In addition, we experimentally demonstrate that high ($> 50\%$) linear-to-circular polarization conversion efficiency can be accomplished by making these silicon-based metasurfaces planar (2D) chiral[84] by design. Our supporting numerical simulations indicate that such metasurfaces can exhibit an extraordinary degree of planar chirality, thus opening exciting possibilities for developing narrow-band thermal emitters of circularly polarized radiation. Si-based metasurfaces are fabricated from standard commercially available silicon-in-insulator (SOI) wafers using standard CMOS-compatible semiconductor fabrication techniques, making them even more appealing for practical applications.

D.1.1 Results

Design of Si-based planar chiral metasurfaces

The conceptual schematic of the metasurface used here and an SEM image of a typical sample are shown in Figure D.1-1. The unit cell's geometry is based on the earlier

developed plasmonic metasurfaces that were utilized for plasmon-induced transparency[95], protein monolayer sensing[8] and infrared spectroscopy of single-layer graphene (SLG)[225]. Each unit cell comprises one straight and one bent Si nanorods, where the bend is responsible for breaking the two mirror inversion symmetries of the unit cell and coupling the bright (electric dipole) and dark (electric quadrupole/magnetic dipole) resonances as schematically shown in Figure D.1-1 (c), where the surface charge density at the air/Si interface is plotted for the eigenmodes of the metasurfaces with and without a symmetry breaking bend.

As collective interactions of each unit cell with its neighbors are important for imparting the metasurface with its optical properties, the eigenmodes of an infinite metasurface were calculated using finite element methods with the COMSOL software. Note[41] that the diffractive effects are unimportant in Fano-resonant metasurfaces, and the spectral position of the dark resonance is determined primarily by the unit cell's geometry (its physical dimensions R, L, g, d and w shown in Figure D.1-1) and not by the period P separating them. Hybridization of the two resonances is responsible for the very sharp Fano features in transmission and reflection spectra as the dark resonance acquires a small electric dipole moment and strongly couples to the incident electromagnetic wave.

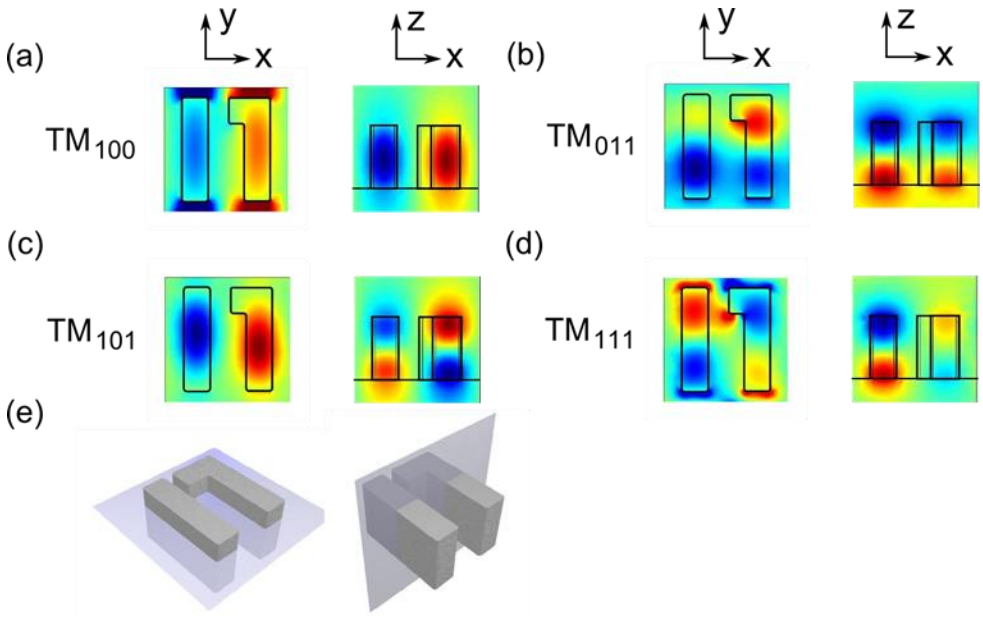

Figure D.1-2 Dark resonances supported by the silicon-based metasurface. (a-d): Color maps of in the $x-y$ plane (left) and $x-z$ plane (right). (e) Illustration of the cutting planes. The plane is at above the base of the silicon metasurface. The plane passes through the middle of the unit cell. The corresponding resonant wavelength are $\lambda_{100} = 4.72\mu m$, $\lambda_{011} = 4.21\mu m$, $\lambda_{101} = 4.12\mu m$, $\lambda_{111} = 4.07\mu m$, respectively. Physical dimensions of the metasurface: same as in Figure D.1-3, with $L = 2\mu m$.

The dark quadrupole resonance is not the only high-Q eigenmode supported by the metasurface. In fact, several strongly localized dark multipole resonances shown in Figure D.1-2 are supported. All resonances are computed for a metasurface with the period $P = 2.4\ \mu m$ and nanorods' cross-section of $0.5\mu m \times 1.2\mu m$ in the x–z plane, with remaining dimensions given in the caption. On the basis of their spatial symmetry, the resonant modes are designated as TM_{ijk}, with $i,j,k = 0$ or 1 corresponding to the $E_y(x,y,z)$ being, respectively, even or odd under the x,y,z inversions. All dark modes are coupled in the near-field to the bright TM_{000} mode, marked as 'dipole' in Figure D.1-1(c). However, because the coupling of the higher-order dark modes to the TM_{000} mode is even weaker than that of the lowest order TM_{100} mode (marked in Figure

D.1-1(c) as ‘quadrupole’), we expect, and experimentally confirm below, that these modes manifest in even sharper Fano resonances. Note that these modes are designated as dark because of their near-vanishing electric and magnetic dipole moments in the x–y plane and, consequently, weak coupling to the normally incident light. The degree of coupling is controlled by the design: a shorter symmetry-breaking bend of a nanorod would result in weaker coupling and higher quality factor Q. In contrast, the Q-factor of the bright modes possessing the in-plane electric/magnetic dipole moments cross-polarized transmission spectra $T_{ij}(\lambda)$ were acquired using polarized infrared spectroscopy, are plotted as a function of the wavelength λ. background reflectivity originates from the Fabry–Perot substrate resonances.

The most remarkable spectral features are observed in the cross-polarized transmission T_{xy} (λ). The baseline $T_{xy}(\lambda)$, small for all non-resonant wavelengths (l45 mm), is dramatically peaked at Fano resonances, as shown in Figure D.1-3(c,f), because of the coupling of the dark modes to both x and y polarizations of the incident light. The estimated quality factors $Q = \lambda/\Delta\lambda$ (where $\Delta\lambda$ is full-width half-maximum (FWHM) of each peak) of the Fano resonances, calculated by fitting the experimental cross-polarized spectra with Lorentzian curves, are listed in Table D.1-1for the three metasurfaces.

Nanorod length →	$\boldsymbol{L = 2\ \mu m}$	$\boldsymbol{L = 1.8\ \mu m}$	$\boldsymbol{L = 1.6\ \mu m}$
Dark mode ↓			
$\boldsymbol{TM_{100}}$	$Q = 75.7$	$Q = 94.3$	$Q = 73.9$
	$\lambda = 4.71\mu m$	$\lambda = 4.57\mu m$	$\lambda = 4.43\mu m$
$\boldsymbol{TM_{011}}$	$Q = 113.3$	$Q = 100$	$Q = 52.9$
	$\lambda = 4.21\mu m$	$\lambda = 4.2\mu m$	$\lambda = 4.21\mu m$
$\boldsymbol{TM_{101}}$	$Q = 113.7$	$Q = 111.7$	$Q = 76.1$
	$\lambda = 4.12\mu m$	$\lambda = 4.09\mu m$	$\lambda = 4.05\mu m$
$\boldsymbol{TM_{111}}$	$Q = 116.9$	$Q = 127.5$	$Q = 98.4$
	$\lambda = 4.07\mu m$	$\lambda = 4.03\mu m$	$\lambda = 3.97\mu m$

Table D.1-1: Comparison of dark modes supported by the silicon metasurfaces. Experimentally estimated quality factors $Q = \lambda/\Delta\lambda$ and spectral positions of the Fano resonances for the three fabricated silicon-based metasurfaces calculated from fitting the polarization conversion spectrum $T_{xy}(\lambda)$ to Lorenzian shape.

These are the narrowest optical resonances observed in collective mid-IR metasurfaces that do not rely on diffractive effects that become important when the wavelength of light becomes commensurate with the periodicity of the array[215]. Unlike

extremely angle-sensitive diffractive structures[92,203,204,206,215], Fano-resonant metasurfaces are ideally matched to far-field The polarizations of the incident/transmitted light ($i, j = x$ or y) are set by the polarizer/analyzer, respectively, as shown in Figure D.1-4. Spectral tunability of three representative metasurfaces was accomplished by varying the length $1.6\mu m < L < 2\mu m$ of the left (straight) nanorod. The $T_{yy}(\lambda)$ spectra provide clear evidence of the Fano interference consistent with Figure D.1-1(c): a broad dip at the frequency of the bright TM_{000} mode at $\lambda_{000} \approx 4.35\mu m$ is superimposed on a set of narrow features corresponding to the dark modes shown in Figure D.1-2. Similar Fano features are observed in the x-polarized transmission $Txx(\lambda)$, where the broadband background reflectivity originates from the Fabry–Perot substrate resonances.

Although achieving high-Q resonances depends on collective interactions40 between neighboring cells of the large area ($300\mu m \times 300\mu m$) metasurfaces used in our experiments, simulations have confirmed that samples as small as $25\mu m \times 12.5\mu m$ (or $6\lambda \times 3\lambda$) can be utilized without any noticeable deterioration of the spectral sharpness. That is because only several neighboring unit cells (two to three on each side horizontally, one on each side vertically according to simulations) effectively interact with each given unit cell. This short-range collective interaction contrasts with long range coherence required for achieving narrow spectral width in photonic structures that rely on diffractive effects[190,215]. The unique capability to combine these small area high-Q metasurfaces with thermal infrared radiation sources is absolutely crucial for the future sensing applications described below.

Experimental demonstration of linear-to-circular polarization conversion

The first application of the planar (2D) chiral metasurfaces[84] described in this Article, suggested by the high cross-polarized transmission T_{xy}, is efficient linear-to-

circular polarization (LP-to-CP) conversion. The conversion efficiency and the degree of circular polarization (DCP) was experimentally investigated using the standard rotating analyzer Stokes polarimetry setup[226] illustrated in Figure D.1-4 to characterize the transmitted polarization state of the y-polarized incident light, and to extract its Stokes parameters $S_0 = |E_x|^2 + \left|E_y\right|^2, S_1 = |E_x|^2 - \left|E_y\right|^2, S_2 = 2Re[E_x E_y^*]$, and $|S_3| = -2Im[E_x E_y^*]$. A nonzero S_3 corresponds to elliptically polarized light, and $S_3 = \pm S_0$ corresponds to right/left CP light. Alternatively, the principal dimensions of the transmitted light's polarization ellipse, its tilt angle β and the ratio a/b between its long and short axes defined in Figure D.1-4, can be expressed in terms of the Stokes parameters.

The measured Stokes parameters and polarization ellipse dimensions for the metasurface with $L = 1.8\mu m$ are plotted in Figure D.1-4(c,d) and are in good agreement with numerical simulations. Note that, away from the Fano resonances, the polarization of the transmitted light is essentially unchanged from its original linear y-polarization, as expressed by $\frac{S_1}{S_0} \approx -1$ in Figure D.1-4(d), and $\beta \approx 90^o$, $b/a \approx 0.1$ in Figure D.1-4(c) for $\lambda > 4.7\mu m$. However, at the Fano resonances the polarization becomes essentially circular, as evidenced by $\frac{|S_3|}{S_0} \approx 1$ and $\frac{b}{a} \approx 0.8$ at $\lambda_{100} \approx 4.55\mu m$, with conversion efficiency$S_0 \approx 50\%$. Even a higher DCP ($b/a > 0.9$) is observed for the TM_{101} mode at $\lambda_{101} \approx 4.1\ \mu m$, thus demonstrating that these metasurfaces can be used for efficient narrow-band LP-to-CP conversion.

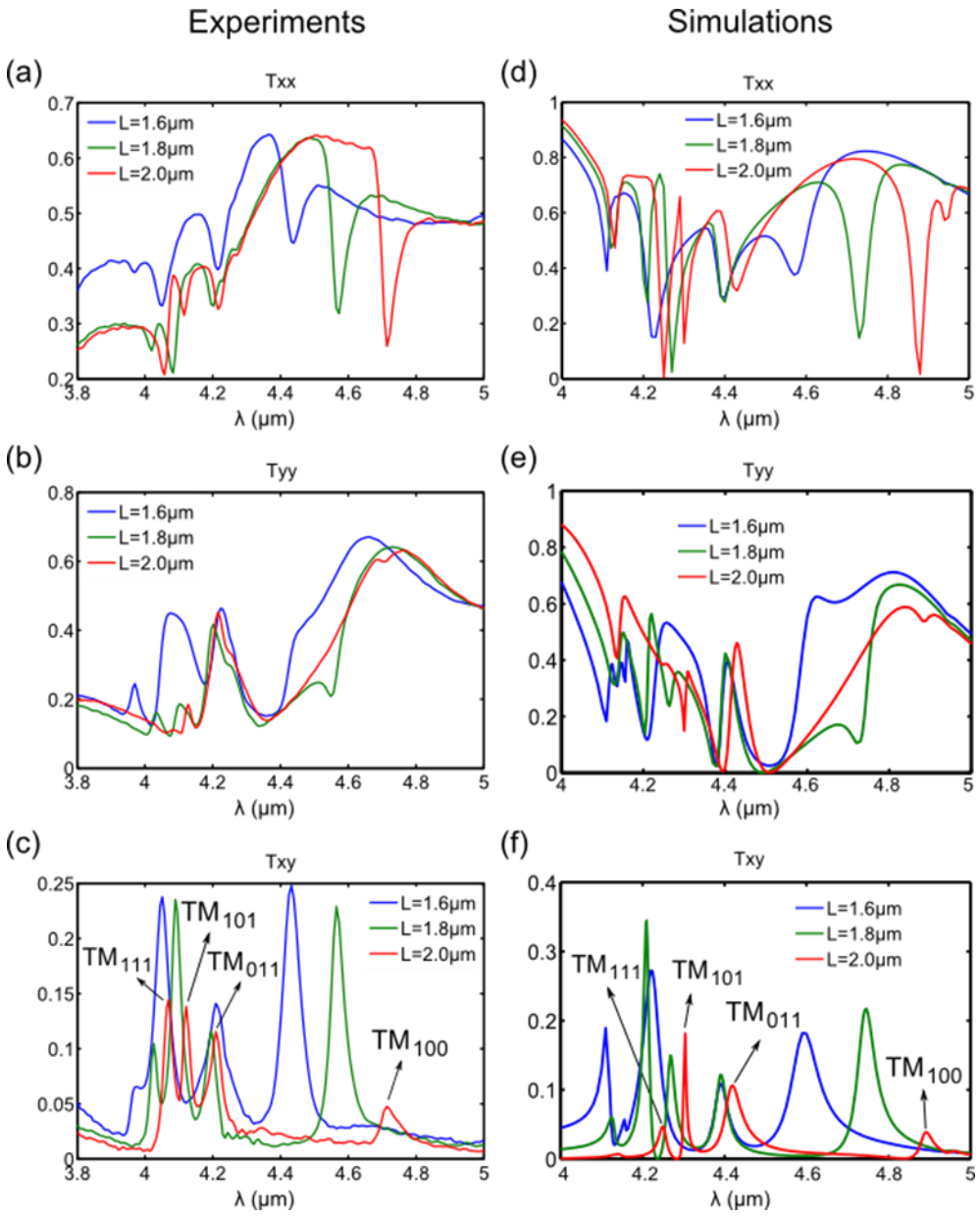

Figure D.1-3: Polarization resolved transmission spectra of the silicon metasurfaces. Measured (a-c) and calculated (d-f) transmission spectra of the silicon metamaterials with $L = 1.6\mu m$, (blue), $1.8\mu m$ (green), and $2.0\mu m$ (red). The spectra of T_{xx} are shown in (a) and (d),T_{yy} are in (b) and (e), and T_{xy} are in (c) and (f). The four dark resonances are labeled in (c) and (d) for the $L = 2\mu m$ sample.

D.1.2 Applications of Chiral Infrared Metasurfaces

The 2D chiral high-Q silicon metasurfaces described in this paper make them an attractive platform for a variety of applications that require spectral selectivity, small pixel size, relatively weak angular sensitivity and strong field enhancement. The simplicity and widespread availability of silicon fabrication techniques used in the semiconductor industry only add to the attractiveness of Si-based metasurfaces for practical applications. Recent advances[227] in transferring the otherwise stiff and brittle silicon structures on flexible substrates is another potentially important contributing factor to future adoption of Si-based metasurfaces by applications that require conformable or stretchable platforms. Below we outline two potential applications that are enabled by the metasurfaces described in this communication: one is the thermal emission of circularly polarized infrared radiation enabled by the extreme chirality of Si-based metasurfaces, and the other is sensing and bio-sensing enabled by the strong optical field concentration and spectral selectivity of these Fano-resonant metasurfaces.

The 2D chiral nature of the metasurfaces discussed above lends itself to another unique application as a source of spectrally selective CP thermal infrared radiation61, which is uniquely distinct from the non-CP thermal radiation emitted by natural environments. High spectral selectivity is required for applications such as infrared identifiers (IRIDs) that rely on unique spectral and polarization signatures of infrared tags. Below we briefly outline the conceptual differences between 2D chiral metasurfaces [84] and other metamaterials used for LP-to-CP conversion, such as the recently demonstrated single-layer plasmonic quarter-wave plates[89] or chiral volumetric metamaterials [91,194].

The action of a quarter-wave plate is based on the phenomenon of birefringence, owing to which the two orthogonal polarizations of light acquire different phase shifts $\phi_{x,y}$ in transmission. The incident LP light can be converted into a right-handed circularly polarized (RCP) or left-handed circularly polarized (LCP) polarization state in transmission if the phase difference $\Delta\phi = \phi_x - \phi_y = \pm\pi/2$. By changing the initial direction of the incoming linear polarization, either RCP or LCP state can be achieved. While quarter-wave plates based on birefringent metasurfaces can be used for efficient LP-to-CP polarization conversion, they cannot be used as stand-alone elements for controlling the polarization state of thermal radiation driven by unpolarized electromagnetic fluctuations dictated63 by the fluctuation-dissipation theorem. On the contrary, it can be demonstrated that the 2D chiral metasurface shown in Figure D.1-1 transmits primarily one CP state. To see this, note that the air-side transmission through the metasurface is highly unusual as indicated by the results of the COMSOL simulations shown in Figure D.1-5. For example, for a planar non-chiral interface one expects that the diagonal elements of the cross-polarized transmission matrix $T_{\alpha,\beta}(\lambda)$ in the circularly polarized basis (a, b: RCP or LCP) dominate over the polarization-converting off-diagonal elements for all wavelengths λ. This is clearly not the case for the studied 2D chiral metasurfaces: according to Figure D.1-5b the diagonal elements are very small while the off-diagonal element TLR is dominant at the resonant wavelength $\lambda \approx 4.7\mu m$. Because of the resonant nature of the metasurface, the RCP-to-LCP and LCP-to-RCP transmission coefficients differ significantly at Fano resonances: $T_{LR} \gg T_{RL}$ despite that $T_{LL} \approx T_{RR}$ as expected for non-3D chiral metamaterials with small substrate effects. This extreme chirality implies that, unlike in the case of a birefringent metasurface, the transmitted radiation is primarily CP even for unpolarized incident light Depending on

the position of the nanorod's bend, the resulting CP state can be engineered to be either mostly LCP (if $T_{LL} \approx T_{RR} \approx 0$ and $T_{LR} \gg T_{RL}$ as shown in Figure D.1-5b) or mostly RCP (if $T_{LR} \ll T_{RL}$).

The strong asymmetry of the total transmission of the two circular polarization states through the 2D chiral dielectric metasurface makes it very distinct from ultrathin 2D chiral metallic metasurfaces that rely on either Ohmic dissipation or symmetry-breaking substrate effects to achieve such transmission asymmetry. Numerical simulations (not shown) indicate that even in the absence of substrate effects (that is, when the $z \to -z$ special inversion symmetry is preserved) and dissipation (which is negligible in Si for mid-IR frequencies) it is possible for the total transmission of the RCP light, $T_R \equiv T_{RR} + T_{RL}$, to be different from the total transmission of the LCP light,$T_L \equiv T_{LL} + T_{RL}$. The physical reason for this is that the combination of spatial inversion and time reversal symmetries only enforces the $T_{LL} \equiv T_{RR}$ requirement. The $T_{LR} \neq T_{RL}$ inequality does not violate any symmetry and does indeed occur for all dielectric metasurfaces with small but finite thickness.

In fact, it can be shown that a lossless all-dielectric metasurface shown in Figure D.1-1 embedded in a fully symmetric dielectric environment can be designed to satisfy the following transmission property at a specific wavelength: $T_{LL} = T_{RR} = T_{RL} = 0$ and $T_{LR} \neq 0$. Satisfying these conditions of extreme chirality ensures that $T_L = 0$ while $T_R \neq 0$, making the metasurface a functional equivalent of an optical device comprising a quarter-wave plate with principal optical axes (x', y'), followed by a linear polarizer whose transmission axis is tilted at 45 with respect to (x', y'), followed by an identical quarter-wave plate. Remarkably, this functionality is achieved by a metasurface that is only about a micron thick. Such functionality cannot be accomplished by an ultrathin 2D

chiral metallic metasurface because the continuity of the electric field across the metasurface enforces the $T_{LR} = T_{RL}$ condition for lossless metallic metasurfaces[81,89] embedded in a symmetric dielectric environment.

Even more significant are the implications of strong spectrally selective reflection asymmetry ($R_{LL} \neq R_{RR}$ as shown in Figure D.1-5a) for applications involving thermal emission of circularly polarized states of light because the emissivity is related to the surface reflectivity through Kirchhoff's law. For example, the circularly polarized emissivity coefficients $\epsilon_R(\lambda)$ and $\epsilon_L(\lambda)$ for a bulk absorbing emitter can be expressed as $\epsilon_R = 1 - R_{RR} - R_{LR}$ and $\epsilon_R = 1 - R_{RR} - R_{LR}$. Thus, calculated CP emissivity coefficients plotted in Figure D.1-5c show a high $DCP(\lambda) \equiv \epsilon_R/\epsilon_L$ of the thermal emission at the Fano resonance wavelength λ_F: $DCP(\lambda)$ has a spectral FWHM of $\delta\lambda_{FWHM} \approx 30nm$ and the peak value of $DCP(\lambda_F) > 20$, which is almost two orders of magnitude higher than its baseline value outside of this narrow resonance region. The unique spectral (very narrow band) and polarization (high DCP) characteristics of the thermal radiation produced by the proposed 2D chiral metasurfaces suggest their applications to IRID tag technologies because they can be easily distinguished from the unpolarized thermal radiation emitted by the environment, and because multiple narrow emission bands with high DCP can be used within the atmospheric transparency window ($3\mu m < \lambda < 5\mu m$). Although fully-3D helical metamaterials8 or their multilayer equivalents[91] can potentially deliver similar performance, their fabrication is considerably more complex than that of a single-layer micron thick metasurface described here.

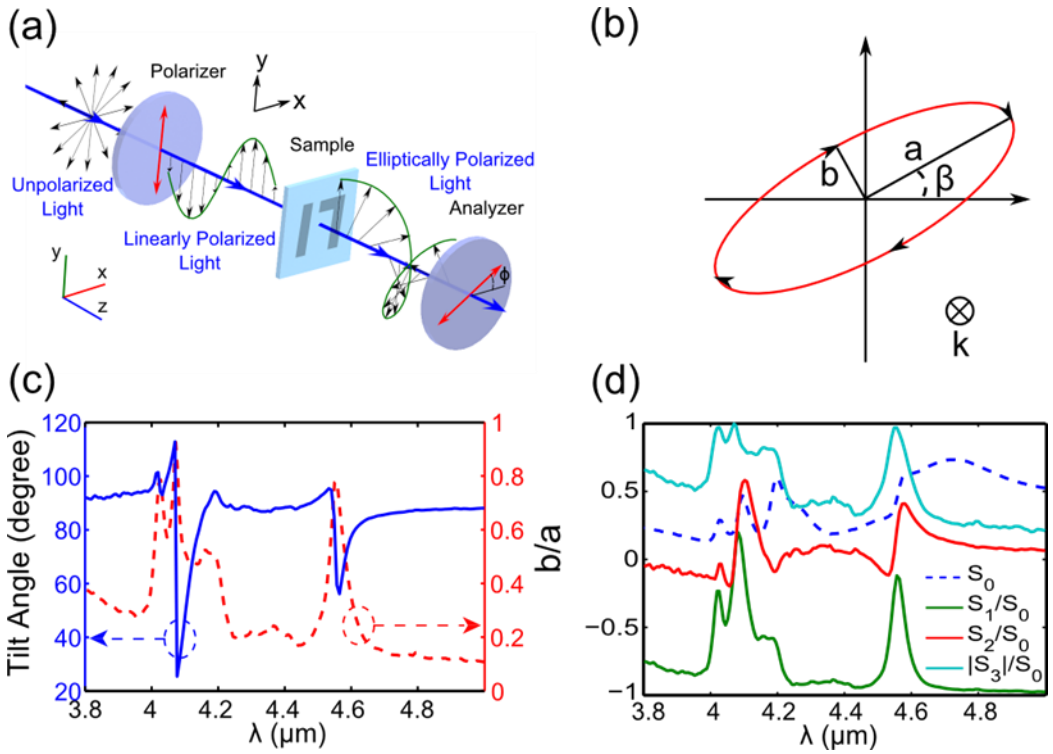

Figure D.1-4: Polarization state manipulation using Fano-resonant 2D chiral metasurfaces. (a) A schematic for the rotating analyzer Stokes polarimetry. The incident beam is polarized in the $y-$ direction. (b) Definition of the polarization ellipse parameters. (c) The measured tilt angle β and the inverse of the ellipticity b/a of the polarization ellipse. (d) The measured Stokes parameters for the $L = 1.8\mu m$ sample. S_1, S_2, and $|S_3|$ are normalized with respect to S_0. Unit cell dimensions: as in Figure D.1-1, and $L = 1.8\mu m$.

High-quality factor and large optical concentration suggest that the above considered metasurfaces could be employed as an excellent platform for enhancing light–matter interaction and for sensing/spectroscopy of minute quantities of matter

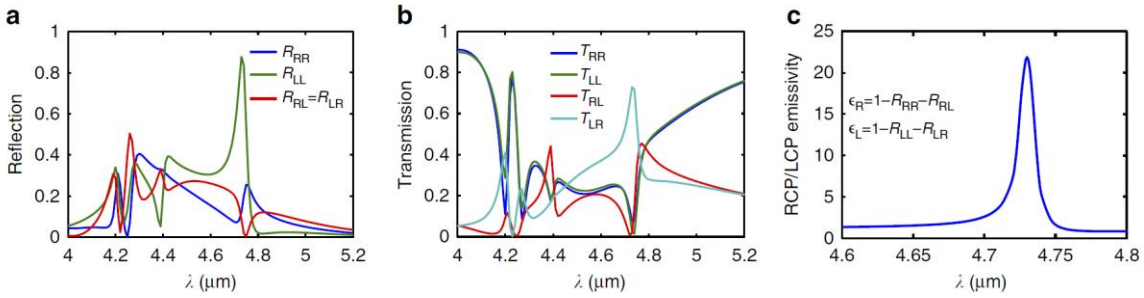

Figure D.1-5: Narrow-band thermal emission of infrared light with high DCP. (a) Numerical (COMSOL) simulation of the cross-polarized reflectivity matrix Ra,b in the circularly polarized basis (a, b: RCP or LCP). Note that $R_{RL} \equiv R_{LR}$ by reciprocity. (b) Air-side cross-polarized transmission matrix Ta,b. Note that the slight deviation from $T_{RR} = T_{LL}$ is a substrate effect in SOI-based metasurfaces: $n_{SiO2} \neq n_{air}$. (c) Estimated DCP of thermal infrared radiation emitted by an infrared-absorbing slab capped by the 2D chiral metasurface. Unit cell dimensions are defined in Figure D.1-1 and $L = 1.8\,\mu m$.

As one representative example, we consider the enhancement of the interaction of infrared light with SLG without the need to focus infrared light to wavelength-scale spots [202]. The optical response of metal-based antennas[6,228] and metasurfaces[225] has been modified by combining them with SLG, and the extracted information was further used to estimate the carrier density in SLG. However, as the spectral linewidth of metal-based structures is fairly broad, only modest changes of the optical response (transmission or reflection) of metasurfaces have been accomplished so far. Our numerical simulations demonstrate that much stronger SLG-induced modification of the transmission through the high-Q non-metallic metasurfaces can be obtained.

As the second representative example, we consider the effect of conformally coating protein monolayers on the optical response of Si-based metasurfaces. Those can be readily functionalized by proteins and protein monolayers that naturally attach to the native oxide formed on the metasurface.

D.1.3 Conclusions and Outlook

The high-Q Fano-resonant dielectric metasurfaces described here represent a novel and promising platform for a variety of applications that depend on high optical energy enhancement and precise spectral matching between molecular/atomic and electromagnetic resonances. Those include infrared spectroscopy of biological and chemical substances and nonlinear infrared optics. Chiral properties of such metasurfaces might be exploited for developing novel ultrathin infrared detectors sensitive to light's chirality, as well as spectrally selective CP thermal emitters61. Even higher quality factors ($Q > 1{,}000$) Fano-resonant metasurfaces can be developed by judicious engineering of near-field coupling between resonant modes if inhomogeneous broadening because of fabrication imperfections can be overcome. Combining the large field enhancements achieved in such high-Q silicon metasurfaces with coherent radiation sources such as quantum cascade lasers capable of delivering high-power low-divergence beams67 would open new exciting opportunities in nonlinear infrared optics such as harmonics generation and four-wave mixing[195,196] using free space excitation.

Appendix D.2: In-Vivo Sensing of Cells using Metamaterial Sensors

In this Chapter we shall discuss cell sensing in vivo. The purpose of this work is to develop a protocol for in vivo cell identification. In the following discussion we shall discuss both live cells immersed in PBS and also fixed cell immersed in PBS. The reason for our interest in fixed cells is because these cells are `frozen' in their state, and therefore measurements on these cells are far more reproducible than on live cells. This is an ongoing work, and I will highlight the portions of the work that have been completed. In the end I will discuss possible future works.

The advantages of performing the experiments in vivo are that a) cells have smaller index contrast with water compared to air (in Chapter C.4) and therefore it is easier to compare the spectra before and after introduction of cells b) it has the potential to shorten the duration of the process.

Cell sorting in microfluidic devices is a new and vigorous field [130,138,229]. Several approaches have been investigated, including size based[137,149,230] image processing based[231], antibody based[232], and dielectrophoresis based[139,140,233]. Here we shall use the last two strategies for their compatibility and complementary nature.

D.2.1 Spectroscopy In-Vivo

The goal of this work is to isolate and identify cancerous cells (CTCs) in patient blood using a microfluidic device. The concept is explained in Figure D.2-1 where patient blood (cleared of its erythrocytes and platelets) is passed through a microfluidic cells. The combined strategy of dielectrophoresis and antibody binding is used to isolate

target cells (CTCs) on sensor arrays. A spectroscopic analysis is performed on the cells isolated on the sensor arrays to confirm cell type.

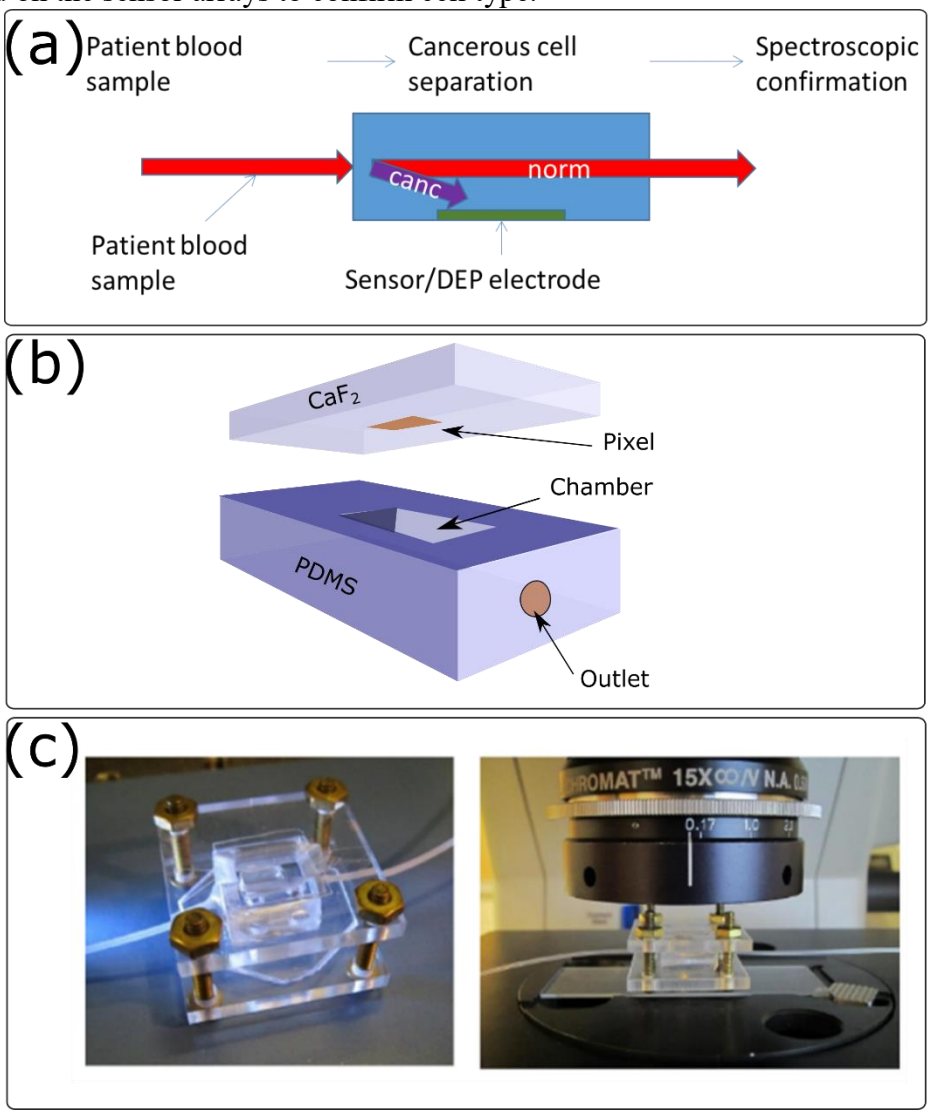

Figure D.2-1: Schematic of the goal of the project

Schematic of the chamber used for experiment consists of a large (2mm x 2mm x 0.5mm) chamber with an inlet and an outlet for liquid. The chamber is made of PDMS on

5 sides with the last side covered by a CaF_2 piece which has an array of sensor pixels on it facing the chamber.

Experimental Procedure

Three sets of data were collected— (i) the `bare' data with the chamber filled with PBS, (ii) the `live' data with live cells on the sensor pixels, and the chamber filled with PBS, and (iii) the `fixed' data with the cells on the sensor pixels fixed, and the chamber filled with PBS.

Cell Preparation and Deposition:

The cells were prepared as described before in Chapter C.4.

The cells suspended in PBS or (in some cases) cell culture media were introduced into the chamber through the inlet with a syringe, as the chamber was being monitored on an inverted microscope. The introduction has to be slow, so that pressure does not build up in the system. There are a few precautions to be taken to avoid bubble— (i) the chamber should be held by hand in such an orientation that the outlet is directly above the inlet. (ii) The introduction of liquid should be slow, allowing enough time for the surfaces to get wet. The PDMS is hydrophobic, which makes formation of bubbles in the corner more likely. It is extremely difficult to avoid bubbles entirely, but bubbles in the corner tends to stay there.

After the chamber is filled with liquid, the chamber is set down on the microscope stage. The chamber was set with the CaF_2 window below, on the sample stage of an inverted microscope with either the 10X or the 20X objective focused on the sensor pixels. The cells, which are slightly heavier than PBS, settle down on the CaF_2 window. This process takes about 5-10 minutes. Once they do, the chamber is allowed to incubate

at 37°C for 4 hours in media. This allows the cell to attach to the substrate (with the sensor array). This was found to give better results than taking data right after cell deposition. After incubation, the media in the chamber is replaced with PBS, and spectra from the sensor pixels are collected. Then the cells are fixed with ice cold acetone, and then PBS is reintroduced into the chamber. Data is collected with the fixed cells immersed in PBS.

In the wet experiments, the derivative spectra do not show very clear features. However, the plot of $\ln(\frac{R_{cell}}{R_{bare}})$ shows much clearer signal from the vibrational lines. In the dry experiments, introduction of the cells led to redshift of the dipole peak, and the Fano feature was diminished. The change was due to the significant difference of refractive index between air and cells. Moreover, this change was difficult to take into account because of the statistical nature of the distribution of cells on the surface. This wasn't a large problem for the dry sensing experiments because the signal stregths were strong enough that we did not need to compare the bare spectra to the cell spectra.

In this case, however, the difference in refractive index between the cell and the medium (PBS or FBS) is weak. As a result, the Fano shape of the spectra of the sensors are preserved. This allows us to compare the bare and the cell spectra (both in PBS), and extract the features. One added advantage of this method is that the contribution from water is much more reproducible than the `dry' case, and the analysis $\ln(\frac{R_{cell}}{R_{bare}})$ automatically accounts for the contribution from water.

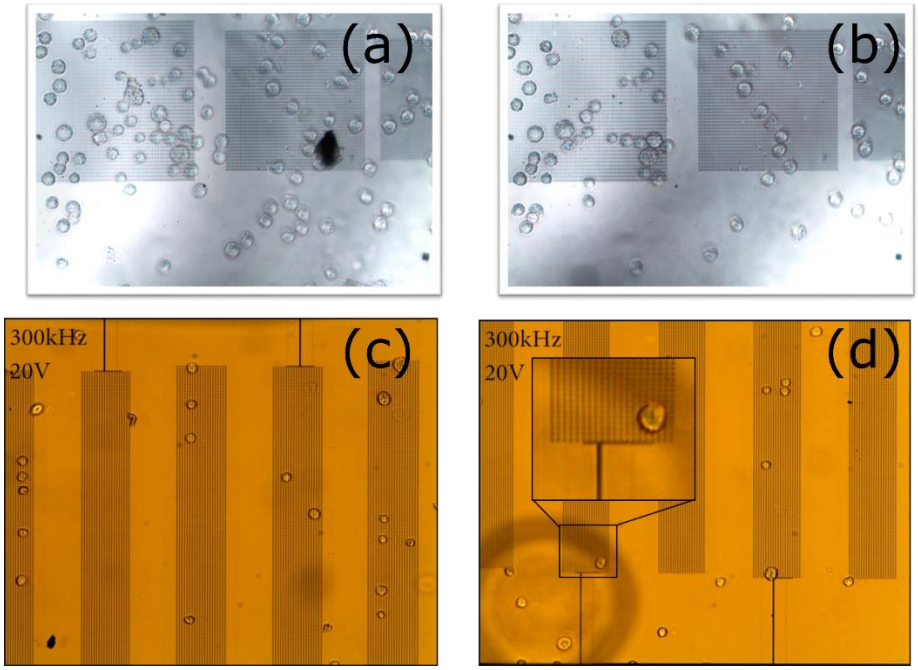

Figure D.2-2: Two strategies were implemented for capturing cancerous cells. (a-b) Shows the result of the first strategy. The sensor pixel is coated with an antibody (anti-epidermal growth factor receptor or anti-EGFR in these experiments) that corresponds to an antibody that some human cancerous cells expresse (EGFR). (a) Was taken after cell deposition on the sensor pixel, and (b) was taken on the same pixel after a vigorous wash. The cells that stay in place are attached to antibody. (c-d) Illustrates results from the second strategy. This is discussed in detail in the following chapter.

D.2.2 DIELECTROPHORESIS (DEP)

As we discussed before, there are largely two classes of methods of identifying cancerous cells. First type of methods use molecular markers (like an antibody) to identify a cell type. Second type of methods use physical properties of cells to identify a cell type. Dielectrophoresis uses response of a cell to an applied electric field to characterize it. Therefore it falls within the second class of methods. DEP has the added advantage in that it not only allows us to distinguish cells, but also separate them.

DEP is the manipulation of dielectric particles in a high gradient AC field. Over the last decade, DEP has emerged as a powerful, non-destructive, and versatile technique for manipulation of dielectric particles, including cells. DEP has been shown to be biocompatible, with no damage done to the cell or its function. A growing body of work uses DEP for applications like immunoassays, real-time polymerase chain reaction (PCR), stem-cell characterization etc. Increasingly, DEP has also been used for single cell characterization and manipulation.

Principle of DEP

DEP is the physical movement of particles caused by static (DC) or alternating (AC) electric field gradient. The basic principle may be explained as follows: a dielectric particle placed in a non-uniform field is polarized, but the two poles experience different forces due to the spatially changing field amplitude. This leads to a net force on the particle.

Cells in suspension are approximated as spherical dielectric particles. The force is on a spherical particle of radius r is given by[234]:

$$< F_{DEP} > = 2\pi r^3 \epsilon_s^* Re\left[\frac{\epsilon_p^* - \epsilon_s^*}{\epsilon_p^* + 2\epsilon_s^*}\right] \nabla\left|\vec{E}_{rms}\right|^2$$

Where $\epsilon_{s^*} = \epsilon_s + i\,\sigma_s/2\pi f$ is the (complex) permittivity of the particle, with ϵ_s being the real part, and σ being the conductivity. f is frequency of the applied field, ϵ_p^* is the permittivity of the particle. The term in the square bracket is referred to the Claussius Mossotti factor. The $\nabla\left|\vec{E}_{rms}\right|^2$ term captures the field inhomogeneity. This equation may be recast in the form:

$$< F_{DEP} > = 2\pi r^3 \epsilon_s^* \left[\frac{f^2 - f_0^2}{f^2 + 2f_0^2}\right] \nabla\left|\vec{E}_{rms}\right|^2$$

Here, $f_0 = \frac{1}{2\pi}\left[\frac{(\sigma_s-\sigma_p)(\sigma_p+2\sigma_s)}{(\epsilon_p-\epsilon_s)(\epsilon_p+2\epsilon_s)}\right]^{1/2}$ is a constant. It is evident that the force changes sign at frequency f_0. This is called the crossover frequency.

Mammalian cells may be safely approximated as a uniform dielectric sphere of permittivity $\epsilon_i^* = \epsilon_i + i\sigma_i/2\pi f$ with a thin (thickness d) membrane an effective dielectric permittivity of ϵ_m^*. The effective permittivity of the cell, then, is

$$\epsilon_p^* = \epsilon_m^* \frac{\left(\frac{r+d}{r}\right)^3 + 2\left(\frac{\epsilon_i^* - \epsilon_m^*}{\epsilon_i^* + 2\epsilon_m^*}\right)}{\left(\frac{r+d}{r}\right)^3 - \left(\frac{\epsilon_i^* - \epsilon_m^*}{\epsilon_i^* + 2\epsilon_m^*}\right)}$$

The cell membrane is made of a lipid bilayer, which has a lower conductivity and permittivity than inside the cell where conduction happens through ions, i.e. $\sigma_i \gg \sigma_m$ and $\epsilon_i > \epsilon_m$. This allows us to write the approximate relation:

$$\epsilon_p^* \sim \epsilon_m^* \frac{r}{d}$$

Therefore, conductance and capacitance of the cell membrane is approximately:

$$C_m \approx \epsilon_p/r \text{ and } g_m \approx \sigma_p/r$$

The crossover frequency is then

$$f_0^2 = \frac{1}{2\pi} \frac{(\sigma_s - r g_m)(2\sigma_s + r g_m)}{(r c_m - \epsilon_s)(r c_m + 2\epsilon_s)}$$

Note that a real solution for f_0 is not always present. When $r g_m \gg \sigma_s$, f_0 is a imaginary number which means that there is no crossover frequency. This can happen when, for example, the cell dies and its membrane breaks down. Such a cell will not be affected by DEP forces and settle down due to gravitational pull.

For viable typical human cells we assume $r g_m \ll \sigma_s$ and $r c_m \gg \epsilon_s$, therefore, the crossover frequency is approximately equal to

$$f_0 = \frac{\sigma_s}{\sqrt{2}\,\pi\, r c_m}$$

For cell membrane, the factor c_m is changes as the cell undergoes morphological changes—healthy human cell membrane folds and changes shape. The conductivity of the cytoplasm σ_s may be assumed to not change as much.

By exploiting different f_0 for different cell types, it is possible to separate different types of cells using DEP. It is most effective in low overall cell concentrations, and when the chamber is not too large. In a large chamber it is difficult to create a field that has strong gradient in most of the chamber. The fields tend to become more uniform farther from the chamber.

DEP was first used to distinguish between dead cells and live ones by Pohl and Hawk[235] in 1966. Pohl noticed a crossover frequency below which the cells are attracted to high field gradient, and above which the cells were repulsed from high field gradients. They predicted that this crossover frequency may be used to distinguish cell types.

Experimental Procedure

A gradual approach was adopted to achieving separation with DEP. The first goal of the project was to confirm that we can indeed attract cells to a DEP electrode. To distinguish different cell types is to be completed in future.

Indium Tin Oxide (ITO) electrodes

First it was verified that cells can indeed be attracted to electrodes. First set of experiments were performed with ITO electrodes deposited on glass substrates, because ITO electrodes are transparent, so we can monitor through the substrate the cells at the surface. The experimental set-up (Figure D.2-3) consisted of a reservoir for liquid made of PDMS, on a glass slide with the electrodes. An ITO-glass cover slip covered the reservoir top. This was useful for two reasons— (i) it allows observation from both top

and bottom, and (ii) the allowed for the inverted microscopes used for these observations. The ITO electrodes consists of parallel linear electrodes. They were connected in two different configurations. In one configuration, AC voltage was applied between altering electrodes (interdigitated configuration). In the second configuration (as shown in Figure D.2-3), all the electrodes were shorted. The top cover was used as the second electrode, and AC voltage was applied between the electrodes and the top cover.

The connections to the electrodes were made using copper tape, which were then connected to a sinusoidal signal generator. We applied a 20V peak to peak AC with varying frequency in the range $100\,KHz - 10MHz$. We noted for the cells under investigation (A-431), the crossover point was approximately at $350KHz$.

The first experiment was performed by putting the cell suspension (cell type: A431) in the chamber, and then covering with the cover slip. The electrical connections were made at this point in the interdigitated configuration, and the AC voltage was applied.

The effect on the cells nearby was immediately visible for the cells that were near the surface. Cells that were far (out of focus), did not respond much to the applied electrical field. The applied frequency was changed from $100KHz - 10MHz$.

At $10MHz$ the cells did not respond to the applied electric field. At a much lower frequency of $600KHz$, the cells were attracted to the electrodes. When the frequency was dialed down to less than $100KHz$, the cells were being repelled from the electrodes.

To perform the dielectrophoresis experiments, we needed a platform that can work both as an electrode for DEP and also as a plasmonic metamaterial sensor. We implemented two solutions to achieve this objective.

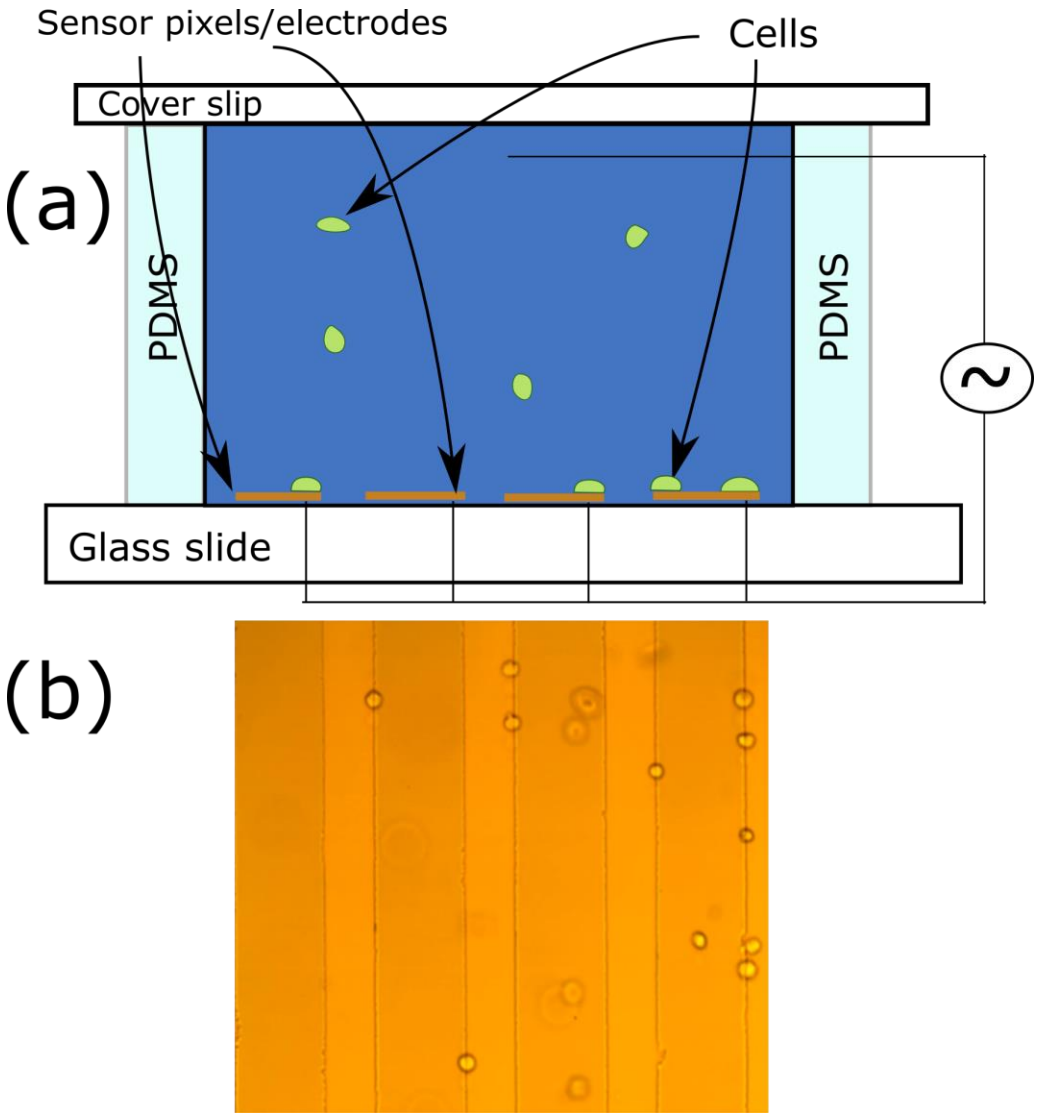

Figure D.2-3: Shows schematic of the DEP setup.

The connected pi

I designed a new metamaterial which is connected to applied DC voltages, or low frequency AC voltages (at least to the range where the DEP operates), but to incident

THz light (near-mid IR), it acts as a plasmonic structure. The benefit of such a structure is that it allows the use of the metamaterial sensor as a DEP electrode.

The experimental set up was essentially the same, except that metamaterial patch was being used as the electrode. We successfully attracted cells to the electrode on application of the AC field.

While performing the preliminary study, both in the ITO electrodes, and the metamaterial electrodes, we found that the cells are attracted to the edges of electrodes. This is because the field gradient is the strongest near the edge of an electrode. This, however, causes a problem— the cells tend to be collected at the edge of the metasurface, making it near impossible to obtain usable spectra from the metasurface. However, there is a simple solution to this problem— the cells gather at the edge of the DEP electrode, and does not care about the edge of the metasurface. Keeping this in mind, we redesigned the metasurface so that the edge of the DEP electrode is in the middle of the metasurface.

The disconnected pi pixels with wire electrodes

Another solution to the same problem consists of simply adding conducting lines to sensor pixels used in the previous study. Since DEP uses comparatively low frequency (a few hundred KHz) that has very long wavelength, adding electrodes (wires) to a pixel would do the job of a DEP electrode.

Appendix D.3: Notes to Chapter B.2

Supplemental Information: Optical realization of double-continuum Fano interference and coherent control in plasmonic metasurfaces

D.3.1 Perturbation Theory: General Formalism

A plasmonic metasurface investigated in this work can be viewed as an extended (in the $x-$ and $y-$ directions) electromagnetic cavity which is open to the light incident along the the $z-$ direction. Such a cavity supports multiple electromagnetic eigenmodes. Because we restrict our analysis to normally incident light, only those eigenmodes that are periodic in x and y are considered. In this work we have focused on three such eigenmodes (resonances) of the unperturbed metasurface shown in Figure B.2-1 that are spectrally close to each other. Based on the charge distribution of these resonances shown in Figure B.2-1, we classified them as DX (electric dipole moment directed along the $x-$ direction), DY (electric dipole moment directed along the $y-$ direction), and DQ ("dark" quadrupole).

When the unit cell of a metasurface is perturbed by the finite displacement s_y of the horizontal nanorod coupler (HNC), the three modes couple to each other and form a set of new eigenmodes of the perturbed metasurface. The coupling between the unperturbed eigenmodes and the formation of the new eigenmodes is described within the framework of the perturbation theory based on the classic work by J. C. Slater[236]. Such perturbation theory was used to calculate the dependence of the normalized coupling coefficients ($\tilde{\kappa}_{XY}, \tilde{\kappa}_{XQ}, \text{and } \tilde{\kappa}_{YQ}$) introduced in Chapter B.2 on the small perturbation parameter s_y. In this Supplemental Material, we perform a semi-analytic perturbative

calculation to achieve a quantitative understanding of the modes' coupling under such perturbation.

Following Slater[236], we consider an unperturbed cavity (volume V) that supports multiple eigenmodes with complex-valued eigenfrequencies $\tilde{\omega}_m$. Their respective eigenmodes are represented by the set of electric and magnetic fields $(\boldsymbol{E}_m, \boldsymbol{H}_m)$. When a wall (of perfect electric conductor) in the cavity is deformed so that the volume is altered by ΔV, the new eigenfields $(\boldsymbol{E}'_m, \boldsymbol{H}'_m)$ and their eigenfrequencies $\tilde{\omega}'$ are also perturbed. The m subscript has been dropped for the perturbed modes, but it is implicitly understood that the number of the perturbed eigenmodes is the same as that of the unperturbed eigenmodes. The perturbed eigenmodes are expanded as

$$\boldsymbol{E}' = \sum_n a_n \boldsymbol{E}_n \text{ and } \boldsymbol{H}' = \sum_n a_n \boldsymbol{H}_n \qquad \text{D.3-1}$$

where a_n-s representing the degree of hybridization between different (unperturbed) eigenmodes. Following the generalization[237] of the classic Slater's theory[236] to the case of a multi-mode cavity, the following matrix equation is derived:

$$\begin{pmatrix} \tilde{\omega}_1 + \Delta_{11} & \Delta_{12} & \cdots \\ \Delta_{21} & \tilde{\omega}_2 + \Delta_{22} & \cdots \\ \vdots & \vdots & \ddots \end{pmatrix} \begin{pmatrix} a_1 \\ a_2 \\ \vdots \end{pmatrix} = \tilde{\omega}' \begin{pmatrix} a_1 \\ a_2 \\ \vdots \end{pmatrix} \qquad \text{D.3-2}$$

where $\tilde{\omega}'$s obtained by solving Eq. D.3-2 are the perturbed eigenfrequencies of the perturbed eigenmodes, and the mode-coupling coefficients are given by the following expression:

$$\Delta_{mn} = \int_{\Delta V} \left(\tilde{\omega}_n \boldsymbol{H}_m^* \cdot \boldsymbol{H}_n - \tilde{\omega}_m \boldsymbol{E}_m^* \cdot \boldsymbol{E}_n \right) dV \qquad \text{D.3-3}$$

where * denotes complex conjugation.

In deriving Eqs. D.3-2, D.3-3 the following normalization has been assumed: $\int_V |E_m|^2 + |H_m|^2 dV = 1$.

The matrix elements Δ_{mn} are responsible for the hybridization between all unperturbed eigenmodes, but we will keep the number of the eigenmodes to just three. As has been earlier noted[237], the matrix given by Eq. D.3-2 is asymmetric, i.e. $\Delta_{mn} \neq \Delta_{nm}^{*}$. The effect of the asymmetry on the correction to eigenfrequencies is second order in Δ_{mn}, and can be neglected because it exceeds the accuracy of our model. The non-zero diagonal elements only cause a trivial renormalization of the eigenfrequencies $\widetilde{\omega}_m'$ while leaving the eigenmodes essentially unchanged. Therefore, in what follows we symmetrize the off-diagonal matrix elements by defining $\kappa_{mn} \equiv |\Delta_{mn} + \Delta_{nm}^{*}|/2$, and we have removed the arbitrary phase of Δ_{mn} so that κ_{mn} are real. The modes' hybridization due to non-zero off-diagonal elements κ_{mn} quantify the degree of modes' hybridization. This gives rise to strong modification in reflection spectrum manifested as the Fano feature induced by the hybridization between two bright dipolar modes and the dark quadrupolar mode. Strong circular dichroism near the quadrupolar resonance is yet another manifestation of the modes' hybridization.

D.3.2 Calculating The Coupling Coefficients (*K*'s) Using Overlap Integrals.

To make the connection between Eqs. D.3-2 and B.2-1, we generalize the latter to include the direct coupling coefficient $\tilde{\kappa}_{YQ} = \tilde{\kappa}_{YQ}^{(dir)}(\widetilde{\omega}_Y - \widetilde{\omega}_Q))$ (which defines $\tilde{\kappa}_{YQ}^{(dir)}$, not to be confused with $\tilde{\kappa}_{YQ}$) and recast in the form of an eigenvalue equation (i.e. by assuming that the incident fields are zero):

$$\begin{pmatrix} \widetilde{\omega}_Y + \kappa_{YY} & \kappa_{YQ} & \kappa_{XY} \\ \kappa_{YQ} & \widetilde{\omega}_Q + \kappa_{QQ} & \kappa_{XQ} \\ \kappa_{XY} & \kappa_{XQ} & \widetilde{\omega}_X + \kappa_{XX} \end{pmatrix} \begin{pmatrix} D_Y \\ Q \\ D_X \end{pmatrix} = \widetilde{\omega}' \begin{pmatrix} D_Y \\ Q \\ D_X \end{pmatrix} \qquad \text{D.3-4}$$

Here Eq. D.3-2 is truncated to just three dominant eigenmodes with amplitudes $D_Y, Q,$ and D_X. The coefficients κ_{mn} are given by Eq. D.3-3. The eigenfrequencies $\widetilde{\omega}'$ correspond to the perturbed system. Let us remind the reader that $\tilde{\kappa}_{YY}$ is defined as $\tilde{\kappa}_{XY} \equiv \kappa_{XY}/(\widetilde{\omega}_X - \widetilde{\omega}_Y)$ and similarly, $\tilde{\kappa}_{XQ} \equiv \kappa_{XQ}/(\widetilde{\omega}_X - \widetilde{\omega}_Q)$.

The perturbed system is treated using a number of coupling coefficients that mix the three relevant eigenmodes (DX, DY and DQ). In Chapter B.2 the normalized coupling coefficients $\tilde{\kappa}_{XY}$ (between DX and DY), and $\tilde{\kappa}_{XQ}$ (between DX and DQ) are introduced. The interaction between DY and DQ emerges in the first-order perturbation theory (referred to as the direct $\tilde{\kappa}_{YQ}^{(dir)}$) and in the second order of the perturbation theory (referred to as the indirect $\tilde{\kappa}_{YQ}^{(ind)}$). It was shown in Chapter B.2 that $\tilde{\kappa}_{YQ}^{(ind)} = \tilde{\kappa}_{XY}\tilde{\kappa}_{XQ}$, and the direct contribution was neglect due to its smallness. Therefore, it was assumed that $\tilde{\kappa}_{YQ} = \tilde{\kappa}_{YQ}^{(dir)} + \tilde{\kappa}_{XY}\tilde{\kappa}_{XQ} \approx \tilde{\kappa}_{XY}\tilde{\kappa}_{XQ}$, see Eq. B.2-4. Below, using the first order Slater's perturbation theory and calculating the overlap integrals given by Eq. D.3-3, we demonstrate that $|\kappa_{YQ}^{dir}| \ll |\kappa_{YQ}^{ind}|$.

A. Perturbative evaluation of $\tilde{\kappa}_{XY}$ and $\tilde{\kappa}_{XQ}$

The unperturbed unit cell shown in Figure D.3-1(a), which is referred to as "Structure A" from here onward, is used to calculate the overlap integrals Δ_{XY} and Δ_{XQ}. The unit cell is perturbed by moving the HNC up by a distance s_y, which is accomplished using a two-step perturbation procedure. First, a metal volume with height s_y shown by a blue box is removed from the bottom of the HNC. Second, an equal volume, shown by a red box in S1, is added to the top of the HNC. The overlap integrals Δ_{mn} (where $m = X$ and $n = Y, Q$) from the total perturbation can be shown (see

below), to the leading order in s_y, to be twice the overlap integral from the second step perturbation:

$$\Delta_{mn} = 2\int_{red\ box} \left(\tilde{\omega}_n \boldsymbol{H}_m^{A^*} \cdot \boldsymbol{H}_m^A - \tilde{\omega}_m \boldsymbol{E}_m^{A^*} \cdot \boldsymbol{E}_n^A\right) dV \quad \text{D.3-5}$$

where $\boldsymbol{E}_m^A$ and $\boldsymbol{H}_m^A$ are, respectively, the electric and magnetic fields corresponding to the nth mode of the unperturbed Structure A. The spatial distribution of the electric and magnetic fields is shown in

Figure D.3-3 (top row). The strongest contribution to Δ_{XY} and Δ_{XQ} comes from the $z-$ component of the magnetic field.

After obtaining the Δ_{mn} it is then symmetrized as described above to obtain κ_{mn}.

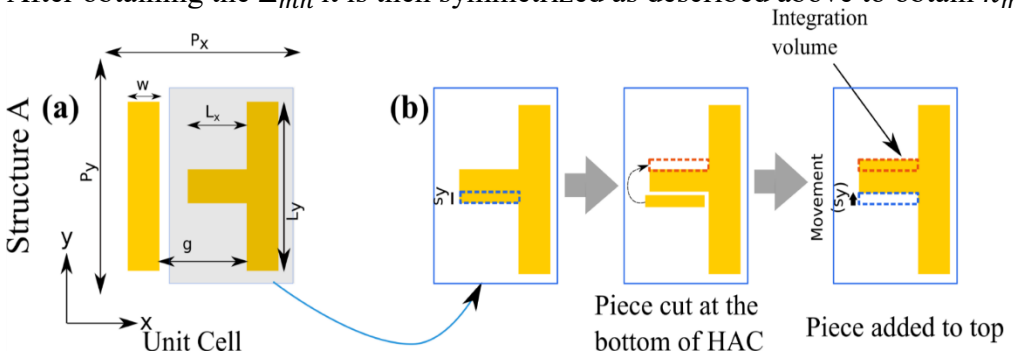

Figure D.3-1: (a) The unit cell of the metasurface in the symmetric ($s_y = 0$) case. (b) A two-step procedure describing how the horizontal nano-coupler (HNC) is vertically displaced by the distance s_y from its symmetric position. This procedure enables a perturbative calculation of the overlap integrals Δ_{XY} and Δ_{XQ}. For all metasurfaces considered here $P_x = 2.7\mu m, P_y = 3.15\mu m, w = 0.36\mu m,\ L_x = 0.92\mu m, L_y = 1.8\mu m$, and $g = 0.66\mu m$.

The fields of DY and DQ eigenmodes have the same mirror reflection symmetry with respect to the $x-$axis passing through the middle of the Structure A. The reflection symmetry of the fields corresponding to the DX eigenmode is opposite to that of the DY and DQ modes. This difference can be best appreciated for the dominant H_z fields: they are even in y for the DY and DQ modes, but odd for the DX mode. If we further assume that the fields created in the blue box (after moving the HAC up) has the same strength as

its nearby fields, then from this symmetry argument one can conclude that the perturbation produced by removing a piece of metal in the blue box is equivalent to the perturbation of adding an identically sized metal volume in the red box. This argument explains the factor 2 in Eq. D.3-5.

The scaling of κ_{XY} and κ_{XQ} with s_y can now be most easily obtained by looking at the contribution of the dominant (H_z) fields to the overlap integrals given by Eq. D.3-5. In the limit of s_y much smaller than the width w of the HNC, the overlap integrals are proportional to the perturbed volume $\Delta V = L_x \times t \times s_y$ shown by the red box from which the fields are displaced. Here t is the metal thickness and L_x is the length of the HNC. Therefore, both κ_{XY} and κ_{XQ} are linearly proportional to s_y. This simple scaling clearly breaks down for large s_y (e.g, $s_y \sim w$) because the fields inside the perturbed integration volume can no longer be regarded as being constant.

We have numerically calculated the coupling coefficients Δ_{mn}s using Eq. D.3-5, and then symmetrizing the Δ_{mn} to obtain κ_{mn}. From the κ_{mn} we obtain $\tilde{\kappa}_{XY}$ and $\tilde{\kappa}_{XQ}$ for different values of s_y. Those coupling coefficients are plotted in Figure D.3-4. It follows from Figure D.3-4 that both $\tilde{\kappa}_{XY}$ and $\tilde{\kappa}_{XQ}$ are indeed linear for $s_y \ll w$, but show saturation for large values of s_y where perturbative calculation is longer valid.

B. Perturbative evaluation of $\tilde{\kappa}_{XQ}$

The indirect coupling coefficient $\tilde{\kappa}_{YQ}^{(ind)}$, which was the only one retained in this work, was directly calculated from the numerically calculated $\tilde{\kappa}_{XY}$ and $\tilde{\kappa}_{XQ}$. Its evolution with s_y is shown in Figure D.3-4. Because $\tilde{\kappa}_{YQ}^{(ind)}$ emerges from the second-order perturbation theory, it is small in comparison with $\tilde{\kappa}_{XY}$ and $\tilde{\kappa}_{XQ}$, both of which were calculated in before from the first-order perturbation theory. Therefore, it had to be multiplied by a factor ×10 in Figure D.3-4 for clarity.

In this part we evaluate $\tilde{\kappa}_{YQ}^{(dir)}$ from the first-order perturbation theory and demonstrate that it is even smaller than $\tilde{\kappa}_{YQ}^{(ind)}$. The numerical demonstration of $\tilde{\kappa}_{YQ}^{(dir)} \ll \tilde{\kappa}_{YQ}^{(ind)}$ justifies our neglecting of $\tilde{\kappa}_{YQ}^{(dir)}$ in Chapter B.2, where $\tilde{\kappa}_{YQ} = \tilde{\kappa}_{YQ}^{(ind)}$ was used.

Applying Eq. D.3-3 to the unperturbed Structure A for calculating $\kappa_{Y\,Q}$ is not trivial because no simple reduction to the expression similar to Eq. D.3-5 is possible. In fact, the contribution of the displaced blue-box volume (Figure D.3-1) cancels that of the red-box volume to the lowest order in s_y because the integrand is even in y:

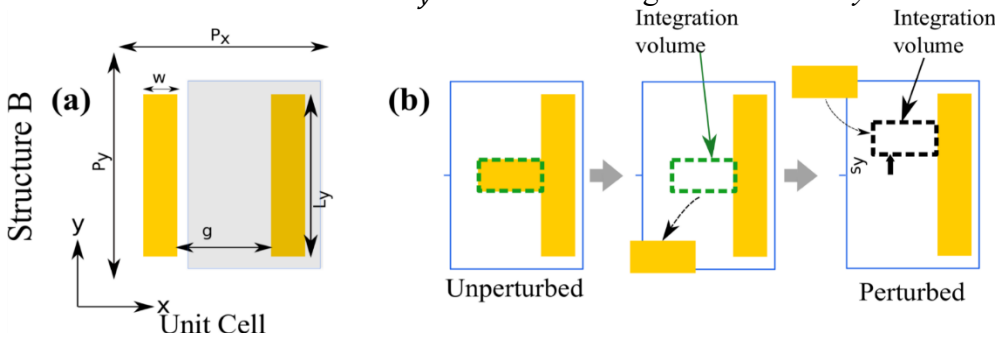

Figure D.3-2: (a) A unit cell of an auxiliary unperturbed metasurface ("Structure B") consists of two vertical nano-antennas. (b) A two-step procedure describing how the horizontal nano-coupler (HNC) is first symmetrically placed at the center of the Structure B, and then vertically displaced by the distance s_y from its symmetric position. This procedure enables a perturbative calculation of the overlap integral Δ_{YQ}.

$$\Delta_{YQ} = \int_{red\ box} \left(\tilde{\omega}_Q \boldsymbol{H}_Y^{A^*} \cdot \boldsymbol{H}_Q^A - \tilde{\omega}_Y \boldsymbol{E}_Y^{A^*} \cdot \boldsymbol{E}_Q^A\right) dV - \int_{blue\ box} \left(\tilde{\omega}_Q \boldsymbol{H}_Y^{A^*} \cdot \boldsymbol{H}_Q^A - \tilde{\omega}_Y \boldsymbol{E}_Y^{A^*} \cdot \boldsymbol{E}_Q^A\right) dV$$
$$\approx \int_{red\ box} \left(\tilde{\omega}_Q \boldsymbol{H}_Y^{A^*} \cdot \boldsymbol{H}_Q^A - \tilde{\omega}_Y \boldsymbol{E}_Y^{A^*} \cdot \boldsymbol{E}_Q^A\right) dV - \int_{red\ box} \left(\tilde{\omega}_Q \boldsymbol{H}_Y^{A^*} \cdot \boldsymbol{H}_Q^A - \tilde{\omega}_Y \boldsymbol{E}_Y^{A^*} \cdot \boldsymbol{E}_Q^A\right) dV$$
$$= 0$$

This indicates that the direct coupling between DY and DQ is zero to first order in s_y. Therefore, as expected, the quadratic in s_y terms become dominant, i.e $\tilde{\kappa}_{YQ}^{dir} \propto \kappa_{YQ} \propto s_y^2$ Therefore, slight differences between the strength of the unperturbed field in the red box and the strength of the perturbed field created after the metal was removed in the

blue box can't be ignored. This makes the numerical calculation of κ_{YQ} using the Structure A as the unperturbed unit cell technically challenging.
Fortunately, there is an easy work-around that involves an ancillary unperturbed unit cell (referred to as "Structure B" from here onward) which is shown in Figure D.3-2. Both DY and DQ resonances are supported by the Structure B as shown in

Figure D.3-3. Therefore, the sought after coupling coefficient κ_{YQ}between the modes due to the diplacement of the HNC from the "green box" location to the "black box" location (see S2) is proportional to the *difference* between the overlap integrals inside the black-box volume (see S2(b), right) and inside the green-box volume (see S2(b), middle). Removing the HNC of the unperturbed Structure A in the green box and then adding an equal HNC back at shifted position in the black box effectively moves the HNC along the y–axis by s_y from the center. Mathematically, this transformation is expressed as follows

$$\Delta_{YQ} = \int_{black} \left(\widetilde{\omega}_Q \boldsymbol{H}_Y^{B^*} \cdot \boldsymbol{H}_Q^B - \widetilde{\omega}_Y \boldsymbol{E}_Y^{B^*} \cdot \boldsymbol{E}_Q^B\right) dV - \int_{green} \left(\widetilde{\omega}_Q \boldsymbol{H}_Y^{B^*} \cdot \boldsymbol{H}_Q^B - \widetilde{\omega}_Y \boldsymbol{E}_Y^{B^*} \cdot \boldsymbol{E}_Q^B\right) dV \quad \text{D.3-6}$$

where where $\boldsymbol{E}^B{}_n$ and $\boldsymbol{H}^B{}_n$ are, correspondingly, the electric and magnetic fields corresponding to the n'th ($n = Q, Y$) mode of the unperturbed Structure B. The spatial distribution of the electric and magnetic fields is shown in
Figure D.3-3 (bottom row).

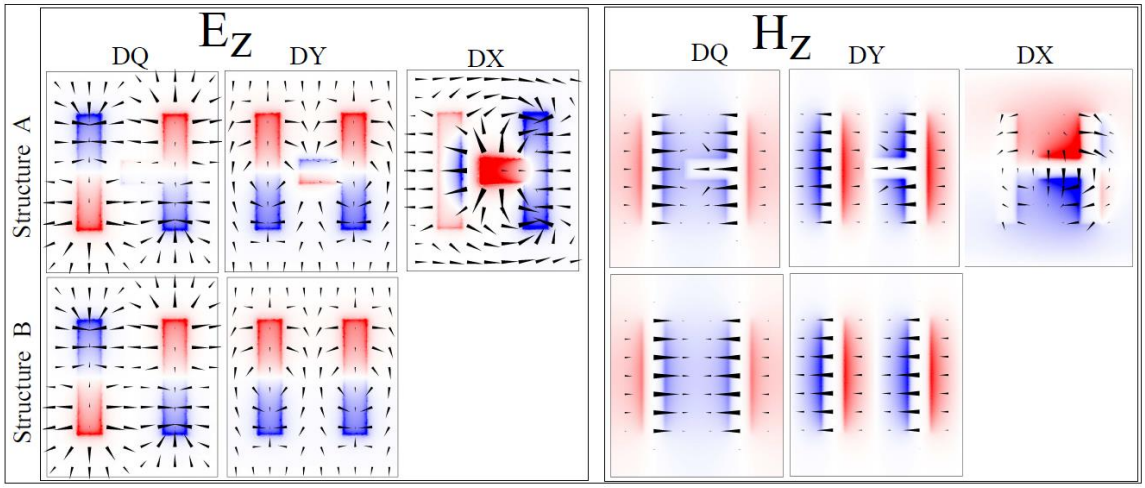

Figure D.3-3: : Field profiles of electromagnetic eigenmodes used to calculate the overlap integrals given by Eq. D.3-3 for the unperturbed Structure A (top row) and by Eq. D.3-6 for the unperturbed Structure B (bottom row). Left panel: E_z (color-coded) and $E_{x,y}$ (arrows). Left panel: H_z (colorcoded) and $H_{x,y}$ (arrows). Note that there is no DX mode for Structure B.

We have numerically calculated the coupling coefficients κ_{YQ} using Eq. D.3-6, and then used the definition of dimensionless $\tilde{\kappa}_{YQ} \equiv \kappa_{YQ}/(\tilde{\omega}_Y - \tilde{\omega}_Q)$ for numerical evaluation of the latter. A plot of $\tilde{\kappa}_{YQ}^{dir}$, multiplied by a factor ×10, is shown in S4, can be compared with $\tilde{\kappa}_{YQ}^{ind}$ plotted in the same figure. Clearly $|\tilde{\kappa}_{YQ}^{dir}| \ll |\tilde{\kappa}_{YQ}^{ind}|$, even though both $\tilde{\kappa}_{YQ}^{dir}$ and $\tilde{\kappa}_{YQ}^{ind}$ are proportional to s_y^2. Therefore $\tilde{\kappa}_{YQ}^{ind}$ is the dominant term. This is the first and the most important justification for neglecting the κ_{YQ} term in Eq. B.2-1 of the Chapter B.2.

It is important, however, to consider whether any new effects are introduced by the inclusion of $\tilde{\kappa}_{YQ}^{dir}$, no matter how small. One of the most important discoveries in this work is the demonstration of the coherent control of optical energy concentration which

is exercised by changing the relative phase between the $x-$ and $y-$ electric field components of the incident light. It was demonstrated in Chapter B.2 that, at the Fano resonance, the amplitude of the dark mode is given by $Q = \left(E_0/\sqrt{2}\right) \times \left(q_{xx} + \exp\left(i\phi\right) q_{yy}\right) / (\omega - \tilde{\omega}'_Q)$, where

$$q_{xx} = \frac{\alpha_x \ \kappa_{XQ}(s_y)}{\tilde{\omega}_X - \tilde{\omega}_Q}, q_{yy} = \frac{\alpha_y \ \kappa_{XQ}(s_y) \ \kappa_{XY}(s_y)}{(\tilde{\omega}_X - \tilde{\omega}_Q)(\tilde{\omega}_Y - \tilde{\omega}_Q)} \quad \text{D.3-7}$$

are complex-valued field enhancement coefficients. The finite phase of $\Delta\varphi = arg(q_{xx}/q_{yy})$ gives rise to chiral dichroism (CD).

The inclusion of a nonzero direct coupling term $\tilde{\kappa}_{YQ}^{dir}$ modifies Eq. D.3-7 as follows:

D.3-8

$$\begin{aligned}
q_{xx} &= \frac{\alpha_x \left[\tilde{\kappa}_{XY} \, \tilde{\kappa}_{YQ}^{(dir)} \, (\tilde{\omega}_X - \tilde{\omega}_Y)(\tilde{\omega}_Y - \tilde{\omega}_Q) + \tilde{\kappa}_{XQ} \, (\tilde{\omega}_X - \tilde{\omega}_Q)(\tilde{\omega}_Y - \tilde{\omega}_Q)\right]}{(\tilde{\omega}_X - \tilde{\omega}_Q)(\tilde{\omega}_Y - \tilde{\omega}_Q)} \\
&= \alpha_x [\tilde{\kappa}_{XY} \, \tilde{\kappa}_{YQ}^{(dir)} \, \frac{(\tilde{\omega}_X - \tilde{\omega}_Y)}{(\tilde{\omega}_X - \tilde{\omega}_Q)} + \tilde{\kappa}_{XQ} \,] \\
&\approx \alpha_x \tilde{\kappa}_{XQ} \\
q_{yy} &= \frac{\alpha_y \left[\tilde{\kappa}_{XY} \, \tilde{\kappa}_{XQ} \, (\tilde{\omega}_X - \tilde{\omega}_Y)(\tilde{\omega}_X - \tilde{\omega}_Q) + \tilde{\kappa}_{YQ}^{(dir)} \, (\tilde{\omega}_Y - \tilde{\omega}_Q)(\tilde{\omega}_X - \tilde{\omega}_Q)\right]}{(\tilde{\omega}_X - \tilde{\omega}_Q)(\tilde{\omega}_Y - \tilde{\omega}_Q)} \\
&= \alpha_y \left[\tilde{\kappa}_{YQ}^{(ind)} \, \frac{(\tilde{\omega}_X - \tilde{\omega}_Y)}{(\tilde{\omega}_Y - \tilde{\omega}_Q)} + \tilde{\kappa}_{YQ}^{(dir)}\right]
\end{aligned}$$

We observe from Eq. D.3-8 that the addition of a small term $|\tilde{\kappa}_{YQ}^{dir}| \ll |\tilde{\kappa}_{YQ}^{ind}|$ slightly changes the phase of q_{yy}. Therefore, the earlier results predicting chiral dichroism due to the finite phase of $\Delta\varphi = \arg(q_{xx}/q_{yy})$ remain valid even for finite .

D.3.3 Fitting Of The Experimental Data To The Analytic CMT Model

In this Section we use the analytic expressions for the reflectivies r_{xx} and r_{yy} given by Eqs. B.2-2, B.2-3 to fit the experimentally measured reflectivities $R_{xx} \equiv |r_{xx}|^2$ and $R_{yy} \equiv |r_{yy}|^2$ in the frequency range of the quadrupolar resonance ($\omega \approx 5 - 7\mu m$). For easy reference, the equations are repeated below:

D.3-9

$$r_{xx} = \frac{\alpha_x^2}{(\omega - \tilde{\omega}_X)} + \frac{\alpha_x^2 \tilde{\kappa}_{XY}^2}{(\omega - \tilde{\omega}_Y)} + \frac{\alpha_x^2 \tilde{\kappa}_{XQ}^2}{(\omega - \tilde{\omega}'_Q)},$$

$$r_{yy} = \frac{\alpha_y^2}{(\omega - \tilde{\omega}_Y)} + \frac{\alpha_y^2 \tilde{\kappa}_{XY}^2}{(\omega - \tilde{\omega}_X)} + \frac{\alpha_y^2 \tilde{\kappa}_{YQ}^2}{(\omega - \tilde{\omega}'_Q)},$$

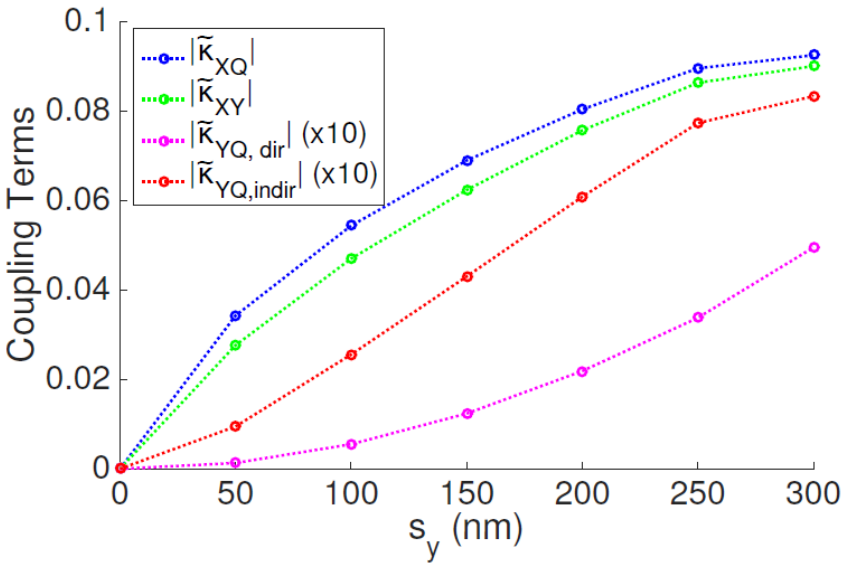

Figure D.3-4: The dependence of the dimensionless coupling coefficients $\tilde{\kappa}_{m,n}$, (where the subscripts *m,n* correspond to *X*, *Y* , and *Q*) on the position s_y of the horizontal nano-coupler (HNC). Note that $|\tilde{\kappa}_{YQ}^{ind}| \gg |\tilde{\kappa}_{YQ}^{dir}|$ for all values of s_y. The perturbation method for calculating $\tilde{\kappa}_{mn}$ based *on calculating the overlap integrals* Δ_{mn} *is valid only for very small values of* s_y.

Numerical fitting of the experimentally measured R_{xx} and R_{yy} was performed for the smaller values of s_y ($s_y \leq 0.52\mu m$), where the analytic theory in Chapter B.2 is formally valid. Matlab optimization toolbox was used to find the best numerical fits for the coefficients ($\alpha_{x,y}$, $\tilde{\kappa}_{XQ}$, and complex-valued $\tilde{\omega}_{X,Y}$). The experimental curves and their fits are shown in Fig. S5. The top row of figures in Figure D.3-5 corresponds to the symmetric case of $s_y = 0$. Therefore, $\tilde{\kappa}_{mn} = 0$ was assumed for Figure D.3-5(a,b). The numerical values of $\tilde{\omega}_{X,Y}$ and $\alpha_{x,y}$ were obtained from the symmetric case.

We further assume that $\widetilde{\omega}_{X,Y}$ and $\alpha_{x,y}$ do not strongly depend on s_y. Therefore, those quantities are used to extract the coupling coefficients $\tilde{\kappa}$'s from the experimentally measured reflectivity curves $R_{xx}(\lambda)$ corresponding to $s_y = 0.6\mu m$ shown in Figure D.3-5 (c,d). Note that in the vicinity of the DQ resonance the contribution from the second term in Eq. S-10 is small compared with that of the third term. As a result, the fitted value of κ_{XY} would have a large error range if it is left as a free parameter. To make the fit more robust, $\tilde{\kappa}_{XY}$ was set equal to $\tilde{\kappa}_{XQ}$. The justification for doing so is that $\tilde{\kappa}_{XY}$ and $\tilde{\kappa}_{XQ}$ are close in value as seen from the overlap integral and from the theoretical plots of $\tilde{\kappa}_{XY}$ and $\tilde{\kappa}_{XQ}$ shown in Fig. S4. Therefore, $\widetilde{\omega}'_Q$ and $\tilde{\kappa}_{XQ}$ were treated as s_y-dependent free parameters to be extracted for several values of s_y. The obtained numerical fits shown in Figure D.3-5 (c) approximate the experimentally measured reflectivity curves reasonably well. The fitted values of $\tilde{\kappa}_{XQ}$ is shown in Figure D.3-5 (d), which shows a monotonic increase in the value of $\tilde{\kappa}_{XQ}$ as expected. The extracted value of $\tilde{\kappa}_{XQ}$ for $s_y = 0.2\mu m$ from the fit is approximately twice the value predicted by the perturbative calculation shown in Figure D.3-4.

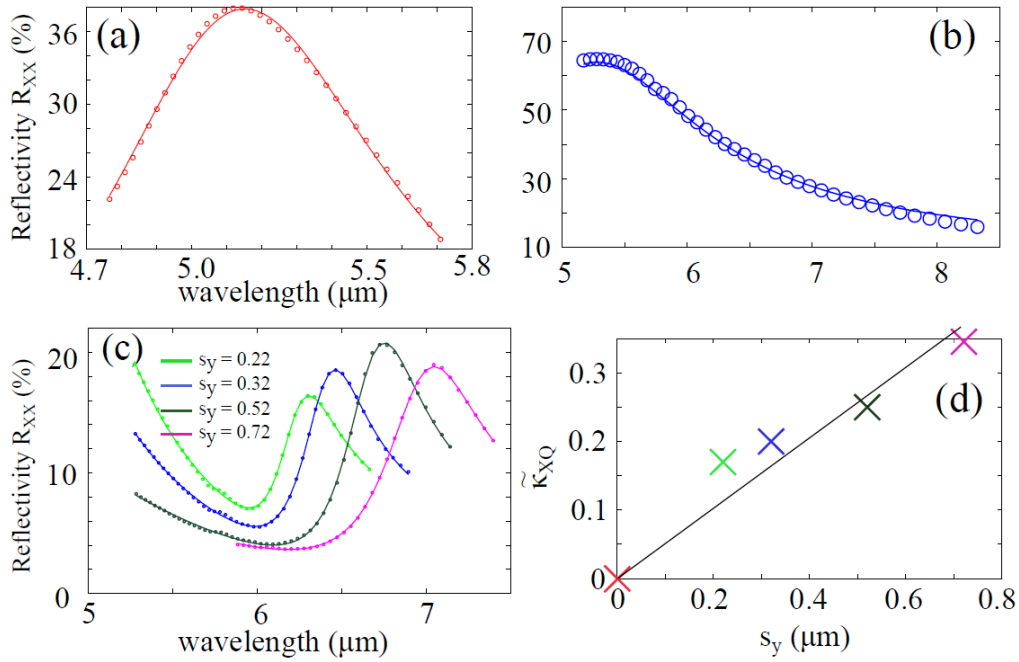

Figure D.3-5: Experimental data (circles) and fitted curve (solid lines) for the symmetric case (s_y = 0) reflectivities (a) R_{xx} and (b) R_{yy}. (c) Experimental data (circles) and fitted curves (solid lines) of asymmetric samples with $s_y \leq 0.72\mu m$. (c) Extracted values of $\tilde{\kappa}_{XQ}$ as a function of s_y. The crosses correspond to extracted values of $\tilde{\kappa}_{XQ}$ from the fits, the solid line is the guide to the eye

Such discrepancy between analytic theory and experiment is not very surprising for several reasons. First, the perturbative calculation is only reliable for $s_y \ll w$. Second, the eigenvalue COMSOL simulation presented in

Figure D.3-3 and used for calculating the overlap integrals were performed under the perfect electrical conductor (PEC) assumption, and also neglected the underlying dielectric substrate. Finally, the assumption that α_x does not change between different values of s_y is yet another approximation that loses validity for large values of s_y because the coupling strength of the x-dipole resonance to the incident field is altered by its position along the nanoantenna.

Nevertheless, there is a good qualitative agreeement between the overlap integrals and the fitted values in the linear increase of $\tilde{\kappa}_{XQ}$. Most importantly, the value of $\tilde{\kappa}_{XQ}$ is shown to monotonically increase as a function of s_y despite the fact that the Fano feature decreases for large values of s_y as can be clearly seen from Figure D.3-5 (c). This confirms the competition between two modes of the continuum in an optical system exhibiting double-continuum Fano interference. Specifically, the near-field coupling between two bright resonances (DX and DY) causes rapid increase of the radiative decay rate of the DX resonance with increasing s_y. This causes the Fano feature observed in x-polarization to decrease for large values of s_y despite the fact that the coupling coefficient $\tilde{\kappa}_{XQ}$ between the ”bright” DX and ”dark” DQ resonances monotonically increases as a function of s_y.

Appendix D.4: Notes to Chapter C.2

D.4.1 Fabrication of the Metamaterial-Based Plasmonic Substrate

Multiple $150\mu m \times 150\mu m$ FRAMM pixels with different antenna sizes were fabricated on a 0.5 mm thick quartz substrates using Electron Beam Lithography (EBL). Polymethyl methacrylate (MicroChem 950 PMMA C2) was spun at 1700 revolutions per second for 30 seconds on the substrate. A thin layer (5 nm) of Chromium was deposited on the PMMA to promote conduction. This layer was etched away with chemical etchant (Transcene chromium etchant 1020AC) after exposure, before developing the sample. Desired structures were written (dosage was 300nC/cm^2 at 10pA beam current) using a Raith 50 electron beam lithography system and then developed in 1:3 MIBK:IPA developer (MicroChem) for 40s. Then 80 nm thick layer of gold was deposited using a thermal evaporator at base pressure of 9x10^{-7} torr. A 3 nm thin layer of chromium was used to enhance adhesion of the gold layer on quartz. Finally, the sample was immersed in acetone for approximately an hour for liftoff.

D.4.2 Optical and Structure Characterization

The reflectivity data on the FRAMM substrates was collected using a Fourier Transform Infrared Spectrometer (FTIR) (Bruker, IFS 66/s) and IR microscope (Bruker, Hyperion 1000). All spectra are normalized to a background taken off of an Aluminum reference mirror. In all cases, both the background and sample spectra are collected at a resolution of 4 cm^{-1} and consist of 256 scans co-added with a mirror repetition rate of 40 kHz. Data are collected under dry air purge to limit atmospheric absorption. The

thickness of the protein layers was independently characterized through ellipsometer (VASE, J. A. Woollam) measurements. For the infrared reflection absorption spectroscopy (IRRAS), 100 nm thick Au on Si slides were immobilized with protein and the reflection of p-polarized infrared light, incident at 80 deg. was measured using a fixed angle grazing incidence unit (Bruker) in the front compartment of an FTIR (Tensor 37, Bruker). The dielectric constant about the Amide-I and II absorption bands of the protein layers on Au was obtained from infrared-reflection absorption spectroscopy measurements in the manner described elsewhere[9]. The thickness obtained from ellipsometer measurements is inserted into a thin film equation to convert reflectance data to Im$(1/\epsilon_n)$. A Lorentz-oscillator dielectric model function is then fit to the data.

D.4.3 Model of the Proteins Permittivity

The following parameters of the effective permittivity $\epsilon_n$given by equation C.2-3 are obtained from IRRAS measurements: (i) $\tilde{A}_{\mathrm{I}} = 0.54 \times 10^{13} rad/s$, $\tilde{A}_{\mathrm{II}} = 0.365 \times 10^{13} rad/s$, $\gamma_{\mathrm{I}} = 0.545 \times 10^{13} rad/s$ and $\gamma_{\mathrm{II}} = 0.45 \times 10^{13} rad/s$ for the protein A/G, and (ii) $\tilde{A}_{\mathrm{I}} = 0.345 \times 10^{13} rad/s$, $\tilde{A}_{\mathrm{II}} = 0.28 \times 10^{13} rad/s$, $\gamma_{\mathrm{I}} = 0.49 \times 10^{13}\ rad/s$ and $\gamma_{\mathrm{II}} = 0.501 \times 10^{13} rad/s$ for the protein IgG. The subscripts I and II indicate amide-I and amide-II resonances, which are spectrally located at the frequencies $\omega_{\mathrm{I}} = 3.12 \times 10^{14} rad/s$ and $\omega_{\mathrm{II}} = 2.91 \times 10^{14} rad/s$ for both proteins.

D.4.4 Supplement D: COMSOL Simulations

To design electromagnetic response of the metamaterial, the commercially available FEM Solver COMSOL Multiphysics was used. Permittivity of the metal

antennas was modeled by the Drude expression $\epsilon_m = 1 + \frac{\omega_p^2}{\omega(\omega+i\gamma)}$ with the parameters corresponding to gold[49]: $\omega_p = 1.32 \times 10^{16}$ rad/s, and $\gamma = 1.2 \times 10^{14}$ rad/s. Periodic boundary conditions were imposed in x- and y-directions to consider periodic arrangement of the meta-molecules.

Appendix D.5: Notes to Chapter C.4

D.5.1 Formal Introduction to Principal Component Analysis

Quoting Bro et al.[187]

> The data are collected in a matrix $\boldsymbol{X}$ with I rows ($i = 1,2 \ldots$; usually samples/objects) and J columns ($j = 1, \ldots, J$; usually variables), hence of size $I \times J$. The individual variables (columns) of $\boldsymbol{X}$ are denoted by x_j ($j = 1 \ldots, J$) and are all vectors in the I-dimensional space. A linear combination of those $\boldsymbol{x}$ variables can be written as $\boldsymbol{t} = w_1 \times \boldsymbol{x}_1 + \cdots + w_J \times \boldsymbol{x}_J$, where $\boldsymbol{t}$ is now a new vector in the same space as the $\boldsymbol{x}$ variables (because it is a linear combination of these). In matrix notation, this becomes $\boldsymbol{t} = \boldsymbol{X}\boldsymbol{w}$, with $\boldsymbol{w}$ being the vector with elements $\boldsymbol{w}_j (j = 1, \ldots J)$. Since the matrix $\boldsymbol{X}$ contains variation relevant to the problem, it seems reasonable to have as much as possible of that variation also in $\boldsymbol{t}$. If this amount of variation in $\boldsymbol{t}$ is appreciable, then it can serve as a good summary of the $\boldsymbol{x}$ variables. Hence, the fourteen variables of $\boldsymbol{X}$ can then be replaced by only one variable $\boldsymbol{t}$ retaining most of the relevant information.
>
> The variation in $\boldsymbol{t}$ can be measured by its variance, $\mathrm{var}(\boldsymbol{t})$, defined in the usual way in statistics. Then the problem translates to maximizing this variance choosing optimal weights $w_1, \ldots, w_J$. There is one caveat, however, since multiplying an optimal w with an arbitrary large number will make the variance of $\boldsymbol{t}$ also arbitrary large. Hence, to have a proper problem, the weights have to be normalized. This is done by requiring that their norm, i.e. the sum-of-squared values, is one. Throughout we will use the symbol $|| \cdot ||^2$ to indicate the squared Frobenius norm (sum-of-squares). Thus, the formal problem becomes
>
> $$\mathrm{argmax}\, \mathrm{var}(\boldsymbol{t})$$

which should be read as the problem of finding the $\boldsymbol{w}$ of length one that maximizes the variance of $\boldsymbol{t}$ (note that $||w|| = 1$ is the same as requiring $||w||^2 = 1$). The function argmax is the mathematical notation for returning the argument w of the maximization function. This can be made more explicit by using the fact that $\boldsymbol{t} = \boldsymbol{Xw}$:

$$\text{argmax}(\boldsymbol{tt})|_{||\boldsymbol{w}||=1} = \text{argmax}(\boldsymbol{w^T X^T Xw})|_{||\boldsymbol{w}||=1}$$

where it is assumed that the matrix $\boldsymbol{X}$ is mean-centered (then all linear combinations are also mean-centered). The latter problem is a standard problem in linear algebra and the optimal $\boldsymbol{w}$ is the (standardized) first eigenvector (i.e. the eigenvector with the largest value) of the covariance matrix $\boldsymbol{X^T X}/(n-1)$ or the corresponding cross-product matrix $\boldsymbol{X^T X}$.

The variance of $\boldsymbol{t}$ can now be calculated but a more meaningful assessment of the summarizing capability of t is obtained by calculating how representative $\boldsymbol{t}$ is in terms of replacing $\boldsymbol{X}$. This can be done by projecting the columns of $\boldsymbol{X}$ on $\boldsymbol{t}$ and calculating the residuals of that projection. This is performed by regressing all variables of X on t using the ordinary regression equation

$$\boldsymbol{X} = \boldsymbol{tp}^T + \boldsymbol{E}$$

where $\boldsymbol{p}$ is the vector of regression coefficients and $\boldsymbol{E}$ is the matrix of residuals. Interestingly, $\boldsymbol{p}$ equals $\boldsymbol{w}$ and the whole machinery of regression can be used to judge the quality of the summarizer $\boldsymbol{t}$. Traditionally, this is done by calculating

$$\frac{||\boldsymbol{X}||^2 - \left|\left|\boldsymbol{E}\right|\right|^2}{||\boldsymbol{X}||^2} 100\%$$

which is referred to as the percentage of explained variation of $\boldsymbol{t}$.

D.5.2 GENERATING DATA

The Matlab script below was used to generate data for illustrating the use of PCA. The variable `usedats` is the generated dataset.

```
% begin script
weight = {[.2 .2]; [.8 .1]; [.1, .8]};
n = 6;
for country=1:3
    socnet = rand(n,1)*200*weight{country}(1);
    esca = rand(n,1)*150*weight{country}(2);

    news{country} = (esca + rand(n,1)*8);
    blogs{country} = (esca/1.5 + socnet/5 + rand(n,1)*2);
    vids{country} = (esca/1.1 + socnet/10 + rand(n,1)*3);
    facebook{country} = (socnet + esca/20 + rand(n,1)*5);
    email{country} = (socnet/5 + esca/30 + rand(n,1)*2);
    usedat{country} = round([news{country} blogs{country}
vids{country} facebook{country} email{country}]);

    try
        usedats = [usedats; usedat{country}];
    catch
        usedats = usedat{country};
    end
end
```

D.5.3 PROCEDURE FOR CALCULATING THE PRINCIPAL COMPONENTS

This tutorial uses data from Table C.4-1. I used Matlab 2015b for this, but the methods should be applicable for versions that are close.

The analysis is described here step by step.

1. **Defining the dataset matrix**: The data is assigned as a matrix in Matlab. The easiest way is to use the workspace browser in Matlab, define a new variable through context menu brought up by right clicking. We will name the new variable $usedat$. Double clicking the variable name opens the `variables' window. This window should look very similar to spreadsheet. Now the data copied from the table can be pasted into the spreadsheet. The columns ($\boldsymbol{v}_i$) represent a vector. The matrix has 5 columns and 20 rows.
2. **(Optional) Normalizing the dataset:** This step is necessary if to make sure all the vectors have the norm of 1 (i.e. $|\boldsymbol{v}_i^{norm}| = 1$). This is done with the Matlab command

   ```
   usedc = normc( usedat )
   ```

   Where usedc is the normalized matrix.

   We normalized the data for the example case, but did not use column normalization for analyzing cell data. For the cell data, the weaker resonance features will get equal weightage as a strong feature if we normalized this way. That would amplify the noises (and the spurious signals that come with it).
3. **Finding the principal components:** The principal components, and the latent score are found with the command

   ```
   [p,~,latent] = pca(usedc);
   ```

Where p is the principal component matrix, which is in this case a 5x5 matrix. The principal components are given by

$$\boldsymbol{v}_i^{pc} = \sum_j \boldsymbol{p}_{ij}\boldsymbol{v}_j'$$

4. **Reduced dimensionality:** To find how many dimensions in the principal component space are important, we calculate

   ```
   captured_variability = cumsum(latent)./sum(latent)
   ```

   For the example data this turns out to be: 0.615, 0.998, 0.999, 1.000, and 1.000, respectively. This means that the first component captures 61% of the variation, and the first two components capture 99.8% of the variation in the data, in other words, just the first principal component is not enough. However, two variables capture most of the variation in the dataset.

5. **Transforming to the principal component basis**: To transform the data to principal component basis, we just multiply the dataset with the rotation matrix $\boldsymbol{c}$. In Matlab:

   ```
   usepc = usedc*c
   ```

BIBLIOGRAPHY

1. Holloway, C. L. *et al.* An overview of the theory and applications of metasurfaces: The two-dimensional equivalents of metamaterials. *Antennas Propag. Mag. IEEE* **54,** 10–35 (2012).
2. Kildishev, A. V., Boltasseva, A. & Shalaev, V. M. Planar photonics with metasurfaces. *Science (80-.).* **339,** 1232009 (2013).
3. Ni, X., Emani, N. K., Kildishev, A. V., Boltasseva, A. & Shalaev, V. M. Broadband light bending with plasmonic nanoantennas. *Science (80-.).* **335,** 427–427 (2012).
4. Schuller, J. A. *et al.* Plasmonics for extreme light concentration and manipulation. *Nat. Mater.* **9,** 193–204 (2010).
5. Yao, J. *et al.* Optical negative refraction in bulk metamaterials of nanowires. *Science (80-.).* **321,** 930–930 (2008).
6. Yao, Y. *et al.* Broad electrical tuning of graphene-loaded plasmonic antennas. *Nano Lett.* **13,** 1257–1264 (2013).
7. Kravets, V. G. *et al.* Singular phase nano-optics in plasmonic metamaterials for label-free single-molecule detection. *Nat. Mater.* **12,** 304–309 (2013).
8. Wu, C. *et al.* Fano-resonant asymmetric metamaterials for ultrasensitive spectroscopy and identification of molecular monolayers. *Nat. Mater.* **11,** 69–75 (2011).
9. Adato, R. *et al.* Ultra-sensitive vibrational spectroscopy of protein monolayers with plasmonic nanoantenna arrays. *Proc. Natl. Acad. Sci.* **106,** 19227–19232 (2009).
10. Vollmer, F. & Arnold, S. Whispering-gallery-mode biosensing: label-free detection down to single molecules. *Nat. Methods* **5,** 591–596 (2008).
11. Powell, D. A. *et al.* Nonlinear control of tunneling through an epsilon-near-zero channel. *Phys. Rev. B* **79,** 245135 (2009).
12. Lee, J. *et al.* Giant nonlinear response from plasmonic metasurfaces coupled to intersubband transitions. *Nature* **511,** 65–69 (2014).
13. Zharov, A. A., Shadrivov, I. V. & Kivshar, Y. S. Nonlinear Properties of Left-Handed Metamaterials. *Phys. Rev. Lett.* **91,** 037401 (2003).
14. Saleh, B. E., Teich, M. C. & Saleh, B. E. *Fundamentals of photonics*. **22,** (Wiley New York, 1991).
15. Shalaev, V. M. Optical negative-index metamaterials. *Nat. Photonics* **1,** 41–48 (2007).
16. Liu, Y. & Zhang, X. Metamaterials: a new frontier of science and technology. *Chem. Soc. Rev.* **40,** 2494–2507 (2011).
17. Chen, K., Adato, R. & Altug, H. Dual-band perfect absorber for multispectral

plasmon-enhanced infrared spectroscopy. *ACS Nano* **6,** 7998–8006 (2012).
18. Liu, N., Mesch, M., Weiss, T., Hentschel, M. & Giessen, H. Infrared perfect absorber and its application as plasmonic sensor. *Nano Lett.* **10,** 2342–2348 (2010).
19. Wu, C. *et al.* Metamaterial-based integrated plasmonic absorber/emitter for solar thermo-photovoltaic systems. *J. Opt.* **14,** 24005 (2012).
20. Avitzour, Y., Urzhumov, Y. A. & Shvets, G. Wide-angle infrared absorber based on a negative-index plasmonic metamaterial. *Phys. Rev. B* **79,** 45131 (2009).
21. Landy, N. I., Sajuyigbe, S., Mock, J. J., Smith, D. R. & Padilla, W. J. Perfect metamaterial absorber. *Phys. Rev. Lett.* **100,** 207402 (2008).
22. Wu, C. *et al.* Large-area wide-angle spectrally selective plasmonic absorber. *Phys. Rev. B* **84,** 75102 (2011).
23. Schurig, D. *et al.* Metamaterial electromagnetic cloak at microwave frequencies. *Science (80-.).* **314,** 977–980 (2006).
24. Cai, W., Chettiar, U. K., Kildishev, A. V. & Shalaev, V. M. Optical cloaking with metamaterials. *Nat. Photonics* **1,** 224–227 (2007).
25. Furlani, E. P. & Baev, A. Optical nanotrapping using cloaking metamaterial. *Phys. Rev. E* **79,** 026607 (2009).
26. Guild, M. D., Haberman, M. R. & Alù, A. Plasmonic cloaking and scattering cancelation for electromagnetic and acoustic waves. *Wave Motion* **48,** 468–482 (2011).
27. Gabrielli, L. H., Cardenas, J., Poitras, C. B. & Lipson, M. Silicon nanostructure cloak operating at optical frequencies. *Nat. Photonics* **3,** 461–463 (2009).
28. Pendry, J. B. J. J. B. Negative refraction makes a perfect lens. *Phys. Rev. Lett.* **85,** 3966–9 (2000).
29. Fleury, R., Sounas, D. & Alù, A. An invisible acoustic sensor based on parity-time symmetry. *Nat. Commun.* **6,** (2015).
30. Zhu, J. *et al.* A holey-structured metamaterial for acoustic deep-subwavelength imaging. *Nat. Phys.* **7,** 52–55 (2011).
31. Li, J. & Chan, C. T. Double-negative acoustic metamaterial. *Phys. Rev. E* **70,** 055602 (2004).
32. Zhang, S., Yin, L. & Fang, N. Focusing ultrasound with an acoustic metamaterial network. *Phys. Rev. Lett.* **102,** 194301 (2009).
33. Bose, J. C. On the rotation of plane of polarisation of electric waves by a twisted structure. *Proc. R. Soc. London* **63,** 146–152 (1898).
34. Chao, C.-Y. & Guo, L. J. Biochemical sensors based on polymer microrings with sharp asymmetrical resonance. *Appl. Phys. Lett.* **83,** 1527–1529 (2003).
35. Liu, N., Tang, M. L., Hentschel, M., Giessen, H. & Alivisatos, A. P. Nanoantenna-enhanced gas sensing in a single tailored nanofocus. *Nat. Mater.* **10,** 631–636 (2011).
36. Veselago, V. G. & Vesslago, V. The electrodynamics of substances with simultaneously negative values of É› and Î¼'. *Sov. Phys. Usp* **10,** 509 (1968).

37. Veselago, V. G. Electrodynamics of materials with negative index of refraction. *Physics-Uspekhi* **46,** 764–768 (2003).
38. Veselago, V., Braginsky, L., Shklover, V. & Hafner, C. Negative refractive index materials. *J. Comput. Theor. Nanosci.* **3,** 189–218 (2006).
39. Smith, D. R., Pendry, J. B. & Wiltshire, M. C. K. Metamaterials and negative refractive index. *Science (80-.).* **305,** 788–792 (2004).
40. Dolling, G., Enkrich, C., Wegener, M., Soukoulis, C. M. & Linden, S. Simultaneous negative phase and group velocity of light in a metamaterial. *Science (80-.).* **312,** 892–894 (2006).
41. Fedotov, V. A. *et al.* Spectral collapse in ensembles of metamolecules. *Phys. Rev. Lett.* **104,** 223901 (2010).
42. Yen, T.-J. *et al.* Terahertz magnetic response from artificial materials. *Science (80-.).* **303,** 1494–1496 (2004).
43. Hoffman, A. J. *et al.* Negative refraction in semiconductor metamaterials. *Nat. Mater.* **6,** 946–950 (2007).
44. Fano, U. Effects of configuration interaction on intensities and phase shifts. *Phys. Rev.* **124,** 1866–1878 (1961).
45. Fan, S., Suh, W. & Joannopoulos, J. D. Temporal coupled-mode theory for the Fano resonance in optical resonators. *JOSA A* **20,** 569 (2003).
46. Fedotov, V., Rose, M., Prosvirnin, S., Papasimakis, N. & Zheludev, N. Sharp Trapped-Mode Resonances in Planar Metamaterials with a Broken Structural Symmetry. *Phys. Rev. Lett.* **99,** 147401 (2007).
47. Miroshnichenko, A., Flach, S. & Kivshar, Y. Fano resonances in nanoscale structures. *Rev. Mod. Phys.* 1–42 (2010).
48. Luk'yanchuk, B. *et al.* The Fano resonance in plasmonic nanostructures and metamaterials. *Nat. Mater.* **9,** 707–715 (2010).
49. Liu, N. *et al.* Plasmonic analogue of electromagnetically induced transparency at the Drude damping limit. *Nat. Mater.* **8,** 758–62 (2009).
50. Hao, F. *et al.* Symmetry Breaking in Plasmonic Nanocavities: Subradiant LSPR Sensing and a Tunable Fano Resonance. *Nano Lett.* **8,** 3983–3988 (2008).
51. Pendry, J. B. J. B., Holden, a. J. J., Robbins, D. J. J. & Stewart, W. J. J. Magnetism from conductors and enhanced nonlinear phenomena. *IEEE Trans. Microw. Theory Tech.* **47,** 2075–2084 (1999).
52. Bennink, R. S., Yoon, Y.-K., Boyd, R. W. & Sipe, J. E. Accessing the optical nonlinearity of metals with metal–dielectric photonic bandgap structures. *Opt. Lett.* **24,** 1416 (1999).
53. Henzler-Wildman, K. & Kern, D. Dynamic personalities of proteins. *Nature* **450,** 964–972 (2007).
54. Jimenez, R., Salazar, G., Yin, J., Joo, T. & Romesberg, F. E. Protein dynamics and the immunological evolution of molecular recognition. *Proc. Natl. Acad. Sci. U. S. A.* **101,** 3803–3808 (2004).
55. Kabashin, a V *et al.* Plasmonic nanorod metamaterials for biosensing. *Nat. Mater.*

8, 867–71 (2009).
56. Lassiter, J. B. *et al.* Fano resonances in plasmonic nanoclusters: geometrical and chemical tunability. *Nano Lett.* **10,** 3184–3189 (2010).
57. Le, F. *et al.* Metallic nanoparticle arrays: a common substrate for both surface-enhanced Raman scattering and surface-enhanced infrared absorption. *ACS Nano* **2,** 707–718 (2008).
58. Enders, D., Rupp, S., Küller, A. & Pucci, A. Surface enhanced infrared absorption on Au nanoparticle films deposited on SiO 2/Si for optical biosensing: Detection of the antibody–antigen reaction. *Surf. Sci.* **600,** L305–L308 (2006).
59. Yu, C., Ganjoo, A., Jain, H., Pantano, C. G. & Irudayaraj, J. Mid-IR biosensor: detection and fingerprinting of pathogens on gold island functionalized chalcogenide films. *Anal. Chem.* **78,** 2500–2506 (2006).
60. Boehr, D. D. & Wright, P. E. How do proteins interact? *Science (80-.).* **320,** 1429–1430 (2008).
61. James, L. C., Roversi, P. & Tawfik, D. S. Antibody multispecificity mediated by conformational diversity. *Science (80-.).* **299,** 1362–1367 (2003).
62. Gizeli, E. & Lowe, C. R. *Biomolecular sensors*. (CRC Press, 2003).
63. Ramachandran, N., Larson, D. N., Stark, P. R. H., Hainsworth, E. & LaBaer, J. Emerging tools for real-time label-free detection of interactions on functional protein microarrays. in *FEBS Journal* **272,** 5412–5425 (2005).
64. Phillips, K. S. Jirí Homola (Ed.): Surface plasmon resonance-based sensors. *Anal. Bioanal. Chem.* **390,** 1221–1222 (2008).
65. Gakamsky, D. M., Luescher, I. F. & Pecht, I. T cell receptor-ligand interactions: a conformational preequilibrium or an induced fit. *Proc. Natl. Acad. Sci. U. S. A.* **101,** 9063–9066 (2004).
66. Nie, S. & Emory, S. R. Probing single molecules and single nanoparticles by surface-enhanced Raman scattering. *Science (80-.).* **275,** 1102–1106 (1997).
67. Cubukcu, E., Zhang, S., Park, Y.-S., Bartal, G. & Zhang, X. Split ring resonator sensors for infrared detection of single molecular monolayers. *Appl. Phys. Lett.* **95,** 043113 (2009).
68. Dong, A., Huang, P. & Caughey, W. S. Protein secondary structures in water from second-derivative amide I infrared spectra. *Biochemistry* **29,** 3303–3308 (1990).
69. DeFlores, L. P., Ganim, Z., Nicodemus, R. A. & Tokmakoff, A. Amide I′- II′ 2D IR spectroscopy provides enhanced protein secondary structural sensitivity. *J. Am. Chem. Soc.* **131,** 3385–3391 (2009).
70. Kauffmann, E., Darnton, N. C., Austin, R. H., Batt, C. & Gerwert, K. Lifetimes of intermediates in the β-sheet to α-helix transition of β-lactoglobulin by using a diffusional IR mixer. *Proc. Natl. Acad. Sci.* **98,** 6646–6649 (2001).
71. (US, N. C. for H. S. *Health Risk Factors*. (National Center for Health Statistics (US), 2014).
72. Stewart, B. & Wild, C. P. World cancer report 2014. *World* (2015).
73. Wittekind, C. & Neid, M. Cancer invasion and metastasis. *Oncology* **69,** 14–16

(2005).
74. Clayden, J., Greeves, N., Warren, S. & Wothers, P. Organic Chemistry. *Am. Nat.* **40,** 1990–1992 (2001).
75. Bonner, W. A. Parity violation and the evolution of biomolecular homochirality. *Chirality* **12,** 114–126 (2000).
76. Khanikaev, A. B., Wu, C. & Shvets, G. Fano-resonant metamaterials and their applications. *Nanophotonics* **2,** 247–264 (2013).
77. Gallinet, B. & Martin, O. J. F. Ab initio theory of Fano resonances in plasmonic nanostructures and metamaterials. *Phys. Rev. B* **83,** 235427 (2011).
78. Wu, C., Khanikaev, A. B. & Shvets, G. Broadband Slow Light Metamaterial Based on a Double-Continuum Fano Resonance. *Phys. Rev. Lett.* **106,** 107403 (2011).
79. Osley, E. J. *et al.* Fano Resonance Resulting from a Tunable Interaction between Molecular Vibrational Modes and a Double Continuum of a Plasmonic Metamolecule. *Phys. Rev. Lett.* **110,** 087402 (2013).
80. Chong, Y. D., Ge, L., Cao, H. & Stone, A. D. Coherent Perfect Absorbers: Time-Reversed Lasers. *Phys. Rev. Lett.* **105,** 053901 (2010).
81. Fedotov, V. A. *et al.* Asymmetric Propagation of Electromagnetic Waves through a Planar Chiral Structure. *Phys. Rev. Lett.* **97,** 167401 (2006).
82. Haus, H. A. Waves and fields in optoelectronics. (1983).
83. García de Abajo, F. J., De Abajo, F. G. & García de Abajo, F. J. Colloquium: Light scattering by particle and hole arrays. *Rev. Mod. Phys.* **79,** 1267–1290 (2007).
84. Fedotov, V. A., Schwanecke, A. S., Zheludev, N. I., Khardikov, V. V. & Prosvirnin, S. L. Asymmetric transmission of light and enantiomerically sensitive plasmon resonance in planar chiral nanostructures. *Nano Lett.* **7,** 1996–1999 (2007).
85. Hendry, E. *et al.* Ultrasensitive detection and characterization of biomolecules using superchiral fields. *Nat. Nanotechnol.* **5,** 783–787 (2010).
86. Tang, Y. & Cohen, A. E. Optical chirality and its interaction with matter. *Phys. Rev. Lett.* **104,** 163901 (2010).
87. Tang, Y. & Cohen, A. E. Enhanced enantioselectivity in excitation of chiral molecules by superchiral light. *Science (80-.).* **332,** 333–336 (2011).
88. Hentschel, M. *et al.* Three-dimensional chiral plasmonic oligomers. *Nano Lett.* **12,** 2542–2547 (2012).
89. Zhao, Y. & Alù, A. Manipulating light polarization with ultrathin plasmonic metasurfaces. *Phys. Rev. B* **84,** 205428 (2011).
90. Zhao, Y. & Alù, A. Tailoring the dispersion of plasmonic nanorods to realize broadband optical meta-waveplates. *Nano Lett.* **13,** 1086–1091 (2013).
91. Zhao, Y., Belkin, M. a. A. & Alù, A. Twisted optical metamaterials for planarized ultrathin broadband circular polarizers. *Nat. Commun.* **3,** 870 (2012).
92. Yanik, A. A. *et al.* Seeing protein monolayers with naked eye through plasmonic

Fano resonances. *Proc. Natl. Acad. Sci.* **108,** 11784–11789 (2011).
93. Khanikaev, A. B. *et al.* Electromagnetically induced polarization conversion. *Opt. Commun.* **285,** 3423–3427 (2012).
94. Papasimakis, N., Fedotov, V. A., Zheludev, N. I. & Prosvirnin, S. L. Metamaterial analog of electromagnetically induced transparency. *Phys. Rev. Lett.* **101,** 253903 (2008).
95. Zhang, S., Genov, D. A., Wang, Y., Liu, M. & Zhang, X. Plasmon-Induced Transparency in Metamaterials. *Phys. Rev. Lett.* **101,** 047401 (2008).
96. Tassin, P. *et al.* Electromagnetically induced transparency and absorption in metamaterials: the radiating two-oscillator model and its experimental confirmation. *Phys. Rev. Lett.* **109,** 187401 (2012).
97. Taubert, R., Hentschel, M., Kästel, J. & Giessen, H. Classical analog of electromagnetically induced absorption in plasmonics. *Nano Lett.* **12,** 1367–1371 (2012).
98. Alonso-Gonzalez, P. *et al.* Real-space mapping of Fano interference in plasmonic metamolecules. *Nano Lett.* **11,** 3922–3926 (2011).
99. Lu, F. & Belkin, M. A. Infrared absorption nano-spectroscopy using sample photoexpansion induced by tunable quantum cascade lasers. *Opt. Express* **19,** 19942–19947 (2011).
100. Lu, F., Jin, M. & Belkin, M. A. Tip-enhanced infrared nanospectroscopy via molecular expansion force detection. *Nat. Photonics* **8,** 307–312 (2014).
101. Papasimakis, N., Fedotov, V. A., Fu, Y. H., Tsai, D. P. & Zheludev, N. I. Coherent and incoherent metamaterials and order-disorder transitions. *Phys. Rev. B* **80,** 041102 (2009).
102. Shvets, G., Wu, C.-H. & Khanikaev, A. Infrared Plasmonic Metamaterials for Slow-Light Applications. in FWO1 (Optical Society of America, 2010).
103. Fan, J. A. *et al.* Fano-like interference in self-assembled plasmonic quadrumer clusters. *Nano Lett.* **10,** 4680–4685 (2010).
104. Fan, J. A. *et al.* Self-assembled plasmonic nanoparticle clusters. *Science (80-.).* **328,** 1135–1138 (2010).
105. Verellen, N. *et al.* Plasmon line shaping using nanocrosses for high sensitivity localized surface plasmon resonance sensing. *Nano Lett.* **11,** 391–397 (2011).
106. Chen, H., Huang, J., Lee, J., Hwang, S. & Koh, K. Surface plasmon resonance spectroscopic characterization of antibody orientation and activity on the calixarene monolayer. *Sensors Actuators B Chem.* **147,** 548–553 (2010).
107. Kumar, S., Aaron, J. & Sokolov, K. Directional conjugation of antibodies to nanoparticles for synthesis of multiplexed optical contrast agents with both delivery and targeting moieties. *Nat. Protoc.* **3,** 314–320 (2008).
108. Lewis, E. N. *et al.* Fourier transform spectroscopic imaging using an infrared focal-plane array detector. *Anal. Chem.* **67,** 3377–3381 (1995).
109. Bellisola, G. & Sorio, C. Infrared spectroscopy and microscopy in cancer research and diagnosis. *Am. J. Cancer Res.* **2,** 1–21 (2012).

110. Bassan, P. *et al.* Reflection contributions to the dispersion artefact in FTIR spectra of single biological cells. *Analyst* **134,** 1171–1175 (2009).
111. Baker, M. J. *et al.* Using Fourier transform IR spectroscopy to analyze biological materials. *Nat. Protoc.* **9,** 1771–91 (2014).
112. Yashunsky, V., Lirtsman, V., Golosovsky, M., Davidov, D. & Aroeti, B. Real-time monitoring of epithelial cell-cell and cell-substrate interactions by infrared surface plasmon spectroscopy. *Biophys. J.* **99,** 4028–4036 (2010).
113. Lee, S. Y. *et al.* Veterinary Science Infrared spectroscopy characterization of normal and lung cancer cells originated from epithelium. **10,** 299–304 (2009).
114. Kazarian, S. G. & Chan, K. L. A. ATR-FTIR spectroscopic imaging: recent advances and applications to biological systems. *Analyst* **138,** 1940–51 (2013).
115. Benard, A. *et al.* Infrared imaging in breast cancer: automated tissue component recognition and spectral characterization of breast cancer cells as well as the tumor microenvironment. *Analyst* **139,** 1044–56 (2014).
116. Mackanos, M. A. & Contag, C. H. FTIR microspectroscopy for improved prostate cancer diagnosis. *Trends Biotechnol.* **27,** 661–663 (2009).
117. Mackanos, M. A. & Contag, C. H. Fiber-optic probes enable cancer detection with FTIR spectroscopy. *Trends Biotechnol.* **28,** 317–323 (2010).
118. Matthäus, C., Bird, B., Miljkovi, M., Chernenko, T. & Romeo, M. NIH Public Access. 275–308 (2010). doi:10.1016/S0091-679X(08)00610-9.Infrared
119. Mostaço-Guidolin, L. B. & Bachmann, L. Application of FTIR Spectroscopy for Identification of Blood and Leukemia Biomarkers: A Review over the Past 15 Years. *Appl. Spectrosc. Rev.* **46,** 388–404 (2011).
120. Liu, K. Z., Xu, M. & Scott, D. A. Biomolecular characterisation of leucocytes by infrared spectroscopy. *Br. J. Haematol.* **136,** 713–722 (2007).
121. Walsh, M. J. *et al.* IR microspectroscopy : potential applications in cervical cancer screening. **246,** 1–11 (2007).
122. Cristofanilli, M. *et al.* Circulating tumor cells, disease progression, and survival in metastatic breast cancer. *N. Engl. J. Med.* **351,** 781–791 (2004).
123. Rehman, S. *et al.* Raman spectroscopic analysis of breast cancer tissues: Identifying differences between normal, invasive ductal carcinoma and ductal carcinoma in situ of the breast tissue. *J. Raman Spectrosc.* **38,** 1345–1351 (2007).
124. Kwak, J. T., Hewitt, S. M., Sinha, S. & Bhargava, R. Multimodal microscopy for automated histologic analysis of prostate cancer. *BMC Cancer* **11,** 62 (2011).
125. Travo, A. *et al.* IR spectral imaging of secreted mucus: A promising new tool for the histopathological recognition of human colonic adenocarcinomas. *Histopathology* **56,** 921–931 (2010).
126. Kazarian, S. G. & Chan, K. L. A. Applications of ATR-FTIR spectroscopic imaging to biomedical samples. *Biochim. Biophys. Acta - Biomembr.* **1758,** 858–867 (2006).
127. Martin, F. L. *et al.* Distinguishing cell types or populations based on the computational analysis of their infrared spectra. *Nat. Protoc.* **5,** 1748–1760 (2010).

128. Barth, A. Infrared spectroscopy of proteins. *Biochim. Biophys. Acta - Bioenerg.* **1767,** 1073–1101 (2007).
129. English, D. & Andersen, B. R. Single-step separation of red blood cells, granulocytes and mononuclear leukocytes on discontinuous density gradients of Ficoll-Hypaque. *J. Immunol. Methods* **5,** 249–252 (1974).
130. Vona, G. *et al.* Isolation by size of epithelial tumor cells: a new method for the immunomorphological and molecular characterization of circulating tumor cells. *Am. J. Pathol.* **156,** 57–63 (2000).
131. Liberti, P. A., Rao, C. G. & Terstappen, L. W. M. M. Optimization of ferrofluids and protocols for the enrichment of breast tumor cells in blood. *J. Magn. Magn. Mater.* **225,** 301–307 (2001).
132. Gascoyne, P. R. C. & Shim, S. Isolation of circulating tumor cells by dielectrophoresis. *Cancers (Basel).* **6,** 545–579 (2014).
133. Hanahan, D. & Weinberg, R. A. The hallmarks of cancer. *Cell* **100,** 57–70 (2000).
134. Paterlini-Brechot, P. & Benali, N. L. Circulating tumor cells (CTC) detection: clinical impact and future directions. *Cancer Lett.* **253,** 180–204 (2007).
135. Bhattacharya, S. *et al.* Selective trapping of single mammalian breast cancer cells by insulator-based dielectrophoresis. *Anal. Bioanal. Chem.* **406,** 1855–1865 (2014).
136. Gascoyne, P. R. C. & Vykoukal, J. Particle separation by dielectrophoresis. *Electrophoresis* **23,** 1973 (2002).
137. Gascoyne, P. R. C. & Vykoukal, J. V. Dielectrophoresis-based sample handling in general-purpose programmable diagnostic instruments. *Proc. IEEE* **92,** 22–42 (2004).
138. Hu, X. *et al.* Marker-specific sorting of rare cells using dielectrophoresis. *Proc. Natl. Acad. Sci. U. S. A.* **102,** 15757–15761 (2005).
139. Huang, Y., Holzel, R., Pethig, R. & Wang, X.-B. Differences in the AC electrodynamics of viable and non-viable yeast cells determined through combined dielectrophoresis and electrorotation studies. *Phys. Med. Biol.* **37,** 1499 (1992).
140. Bustin, S. A. Absolute quantification of mRNA using real-time reverse transcription polymerase chain reaction assays. *J. Mol. Endocrinol.* **25,** 169–193 (2000).
141. Pfaffl, M. W. A new mathematical model for relative quantification in real-time RT–PCR. *Nucleic Acids Res.* **29,** e45–e45 (2001).
142. Vandesompele, J. *et al.* Accurate normalization of real-time quantitative RT-PCR data by geometric averaging of multiple internal control genes. *Genome Biol.* **3,** 1–12 (2002).
143. Wang, H.-N. & Vo-Dinh, T. Multiplex detection of breast cancer biomarkers using plasmonic molecular sentinel nanoprobes. *Nanotechnology* **20,** 065101 (2009).
144. Ring, A. E., Zabaglo, L., Ormerod, M. G., Smith, I. E. & Dowsett, M. Detection of circulating epithelial cells in the blood of patients with breast cancer: comparison of three techniques. *Br. J. Cancer* **92,** 906–912 (2005).

145. Plaks, V., Koopman, C. D. & Werb, Z. Circulating tumor cells. *Sci. (New York, NY)* **341,** (2013).
146. Huang, X., Jain, P. K., El-Sayed, I. H. & El-Sayed, M. A. Gold nanoparticles: interesting optical properties and recent applications in cancer diagnostics and therapy. (2007).
147. Huang, X., Jain, P. K., El-Sayed, I. H. & El-Sayed, M. A. Plasmonic photothermal therapy (PPTT) using gold nanoparticles. *Lasers Med. Sci.* **23,** 217–228 (2008).
148. Dickerson, E. B. *et al.* Gold nanorod assisted near-infrared plasmonic photothermal therapy (PPTT) of squamous cell carcinoma in mice. *Cancer Lett.* **269,** 57–66 (2008).
149. Anker, J. N. *et al.* Biosensing with plasmonic nanosensors. *Nat. Mater.* **7,** 442–453 (2008).
150. Hentschel, M. *et al.* Transition from isolated to collective modes in plasmonic oligomers. *Nano Lett.* **10,** 2721–2726 (2010).
151. Joannopoulos, J. D., Johnson, S. G., Winn, J. N. & Meade, R. D. Photonic crystals: molding the flow of light. (2011).
152. Jiang, X. *et al.* Resolving voltage-dependent structural changes of a membrane photoreceptor by surface-enhanced IR difference spectroscopy. *Proc. ...* **105,** 12113–12117 (2008).
153. Englund, D. *et al.* Controlling cavity reflectivity with a single quantum dot. *Nature* **450,** 857–861 (2007).
154. Bae, Y. M., Oh, B.-K., Lee, W. W. H., Lee, W. W. H. & Choi, J.-W. Study on orientation of immunoglobulin G on protein G layer. *Biosens. Bioelectron.* **21,** 103–110 (2005).
155. Yang, H. *et al.* Protein conformational dynamics probed by single-molecule electron transfer. *Science* **302,** 262–6 (2003).
156. Karatekin, E. & Rothman, J. E. Fusion of single proteoliposomes with planar, cushioned bilayers in microfluidic flow cells. *Nat. Protoc.* **7,** 903–20 (2012).
157. Dulkeith, E. *et al.* Fluorescence Quenching of Dye Molecules near Gold Nanoparticles: Radiative and Nonradiative Effects. *Phys. Rev. Lett.* **89,** 203002 (2002).
158. Anger, P., Bharadwaj, P. & Novotny, L. Enhancement and Quenching of Single-Molecule Fluorescence. *Phys. Rev. Lett.* **96,** 113002 (2006).
159. Cetin, A. E. *et al.* Handheld high-throughput plasmonic biosensor using computational on-chip imaging. *Light Sci. Appl.* **3,** e122 (2014).
160. Choi, B. *et al.* Overcoming metal-induced fluorescence quenching on plasmo-photonic metasurfaces coated by a self-assembled monolayer. *Chem. Commun.* **51,** 11470–11473 (2015).
161. Wu, C. *et al.* Fano-resonant asymmetric metamaterials for ultrasensitive spectroscopy and identification of molecular monolayers. *Nat. Mater.* **11,** 69–75 (2012).
162. Shvets, G. *et al.* Fano-resonant Asymmetric Metamaterials for Sensing and

Vibrational Fingerprinting of Protein Monolayers. in QM4F–6 (Optical Society of America, 2012).
163. Ye, X. *et al.* Investigations of Heme Protein Absorption Line Shapes, Vibrational Relaxation, and Resonance Raman Scattering on Ultrafast Time Scales †. *J. Phys. Chem. A* **107,** 8156–8165 (2003).
164. Arju, N., Ma, T., Khanikaev, A., Purtseladze, D. & Shvets, G. Optical Realization of Double-Continuum Fano Interference and Coherent Control in Plasmonic Metasurfaces. *Phys. Rev. Lett.* **114,** 237403 (2015).
165. Wong, P. T., Wong, R. K., Caputo, T. a, Godwin, T. a & Rigas, B. Infrared spectroscopy of exfoliated human cervical cells: evidence of extensive structural changes during carcinogenesis. *Proc. Natl. Acad. Sci. U. S. A.* **88,** 10988–10992 (1991).
166. Cohenford, M. a & Rigas, B. Cytologically normal cells from neoplastic cervical samples display extensive structural abnormalities on IR spectroscopy: implications for tumor biology. *Proc. Natl. Acad. Sci. U. S. A.* **95,** 15327–32 (1998).
167. Argov, S. *et al.* Diagnostic potential of Fourier-transform infrared microspectroscopy and advanced computational methods in colon cancer patients. *J. Biomed. Opt.* **7,** 248–254 (2002).
168. Gazi, E. *et al.* The combined application of FTIR microspectroscopy and ToF-SIMS imaging in the study of prostate cancer. *Faraday Discuss.* **126,** 77–92 (2004).
169. Tfayli, A., Piot, O., Durlach, A., Bernard, P. & Manfait, M. Discriminating nevus and melanoma on paraffin-embedded skin biopsies using FTIR microspectroscopy. *Biochim. Biophys. Acta - Gen. Subj.* **1724,** 262–269 (2005).
170. German, M. J. *et al.* Infrared spectroscopy with multivariate analysis potentially facilitates the segregation of different types of prostate cell. *Biophys. J.* **90,** 3783–95 (2006).
171. Huang, Z. *et al.* Near-infrared Raman spectroscopy for optical diagnosis of lung cancer. *Int. J. Cancer* **107,** 1047–52 (2003).
172. Haka, A. S. *et al.* Diagnosing breast cancer by using Raman spectroscopy. *Proc. Natl. Acad. Sci. U. S. A.* **102,** 12371–6 (2005).
173. Hammiche, A., German, M. J., Hewitt, R., Pollock, H. M. & Martin, F. L. Monitoring cell cycle distributions in MCF-7 cells using near-field photothermal microspectroscopy. *Biophys. J.* **88,** 3699–706 (2005).
174. Mordechai, S. *et al.* Possible common biomarkers from FTIR microspectroscopy of cervical cancer and melanoma. *J. Microsc.* **215,** 86–91 (2004).
175. Petibois, C. & Deleris, G. Chemical mapping of tumor progression by FT-IR imaging: towards molecular histopathology. *Trends Biotechnol.* **24,** 455–462 (2006).
176. Budínová, G., Salva, J. & Volka, K. Application of molecular spectroscopy in the mid-infrared region to the determination of glucose and cholesterol in whole blood

and in blood serum. *Appl. Spectrosc.* **51,** 631–635 (1997).
177. Shaw, R. A., Kotowich, S., Mantsch, H. H. & Leroux, M. Quantitation of protein, creatinine, and urea in urine by near-infrared spectroscopy. *Clin. Biochem.* **29,** 11–19 (1996).
178. Heise, H. M. & Bittner, A. Multivariate calibration for physiological samples using infrared spectra with choice of different intensity data. *J. Mol. Struct.* **348,** 127–130 (1995).
179. Tobin, M. J. *et al.* Infrared microscopy of epithelial cancer cells in whole tissues and in tissue culture, using synchrotron radiation. *Faraday Discuss.* **126,** 27–39; discussion 77–92 (2004).
180. Sahu, R. K. *et al.* Can Fourier transform infrared spectroscopy at higher wavenumbers (mid IR) shed light on biomarkers for carcinogenesis in tissues? *J. Biomed. Opt.* **10,** 054017–1 – 054017–10 (2015).
181. Krafft, C., Sobottka, S. B., Geiger, K. D., Schackert, G. & Salzer, R. Classification of malignant gliomas by infrared spectroscopic imaging and linear discriminant analysis. *Anal. Bioanal. Chem.* **387,** 1669–1677 (2007).
182. Arju, N., Ma, T., Khanikaev, A., Purtseladze, D. & Shvets, G. Optical Realization of Double-Continuum Fano Interference and Coherent Control in Plasmonic Metasurfaces. *Phys. Rev. Lett.* **114,** 237403 (2015).
183. Aksu, S. *et al.* High-throughput nanofabrication of infrared plasmonic nanoantenna arrays for vibrational nanospectroscopy. *Nano Lett.* **10,** 2511–2518 (2010).
184. Adato, R. & Altug, H. In-situ ultra-sensitive infrared absorption spectroscopy of biomolecule interactions in real time with plasmonic nanoantennas. *Nat. Commun.* **4,** 2154 (2013).
185. Adato, R. *et al.* Ultra-sensitive vibrational spectroscopy of protein monolayers with plasmonic nanoantenna arrays. *Proc. Natl. Acad. Sci.* **106,** 19227–19232 (2009).
186. Dresselhaus, M. S., Dresselhaus, G., Saito, R. & Jorio, a. Raman spectroscopy of carbon nanotubes. *Phys. Rep.* **409,** 47–99 (2005).
187. Bro, R. & Smilde, A. K. Principal component analysis. *Anal. Methods* **6,** 2812 (2014).
188. Richter, T. *et al.* Identification of tumor tissue by FTIR spectroscopy in combination with positron emission tomography. *Vib. Spectrosc.* **28,** 103–110 (2002).
189. Saleh, M. N. *et al.* Combined modality therapy of A431 human epidermoid cancer using anti-EGFr antibody C225 and radiation. *Cancer Biother. Radiopharm.* **14,** 451–463 (1999).
190. Rodriguez, S. R. K., Schaafsma, M. C., Berrier, A. & Rivas, J. G. Collective resonances in plasmonic crystals: Size matters. *Phys. B Condens. Matter* **407,** 4081–4085 (2012).
191. Wu, C. *et al.* Spectrally selective chiral silicon metasurfaces based on infrared Fano resonances. *Nat. Commun.* **5,** 1–9 (2014).

192. Yu, N. *et al.* Light propagation with phase discontinuities: generalized laws of reflection and refraction. *Science (80-.).* **334,** 333–337 (2011).
193. Spinelli, P., Verschuuren, M. A. & Polman, A. Broadband omnidirectional antireflection coating based on subwavelength surface Mie resonators. *Nat. Commun.* **3,** 692 (2012).
194. Gansel, J. K. *et al.* Gold helix photonic metamaterial as broadband circular polarizer. *Science (80-.).* **325,** 1513–1515 (2009).
195. Klein, M. W., Enkrich, C., Wegener, M. & Linden, S. Second-harmonic generation from magnetic metamaterials. *Science (80-.).* **313,** 502–504 (2006).
196. Zhang, Y., Wen, F., Zhen, Y.-R., Nordlander, P. & Halas, N. J. Coherent Fano resonances in a plasmonic nanocluster enhance optical four-wave mixing. *Proc. Natl. Acad. Sci.* **110,** 9215–9219 (2013).
197. Liu, X. *et al.* Taming the blackbody with infrared metamaterials as selective thermal emitters. *Phys. Rev. Lett.* **107,** 045901 (2011).
198. Zheludev, N. I., Prosvirnin, S. L., Papasimakis, N. & Fedotov, V. A. Lasing spaser. *Nat. Photonics* **2,** 351–354 (2008).
199. Vahala, K. J. Optical microcavities. *Nature* **424,** 839–846 (2003).
200. Armani, D. K., Kippenberg, T. J., Spillane, S. M. & Vahala, K. J. Ultra-high-Q toroid microcavity on a chip. *J. High Energy Phys* **8,** 37 (2000).
201. Gan, X. *et al.* Strong enhancement of light–matter interaction in graphene coupled to a photonic crystal nanocavity. *Nano Lett.* **12,** 5626–5631 (2012).
202. Gan, X., Mak, K., Gao, Y., You, Y. & Hatami, F. Strong Enhancement of Light–Matter Interaction in Graphene Coupled to a Photonic Crystal Nanocavity. *Nano …* (2012).
203. Thurman, S. T. & Morris, G. M. Controlling the spectral response in guided-mode resonance filter design. *Appl. Opt.* **42,** 3225–3233 (2003).
204. Kravets, V. G., Schedin, F. & Grigorenko, A. N. Extremely narrow plasmon resonances based on diffraction coupling of localized plasmons in arrays of metallic nanoparticles. *Phys. Rev. Lett.* **101,** 087403 (2008).
205. Tetz, K. A., Pang, L. & Fainman, Y. High-resolution surface plasmon resonance sensor based on linewidth-optimized nanohole array transmittance. *Opt. Lett.* **31,** 1528–1530 (2006).
206. Zhen, B. *et al.* Enabling enhanced emission and low-threshold lasing of organic molecules using special Fano resonances of macroscopic photonic crystals. *Proc. Natl. Acad. Sci.* **110,** 13711–13716 (2013).
207. Lin, C. & Povinelli, M. L. Optical absorption enhancement in silicon nanowire arrays with a large lattice constant for photovoltaic applications. *Opt. Express* **17,** 19371–19381 (2009).
208. Mashev, L. & Popov, E. Zero order anomaly of dielectric coated gratings. *Opt. Commun.* **55,** 377–380 (1985).
209. Hsu, C. W. *et al.* Observation of trapped light within the radiation continuum. *Nature* **499,** 188–191 (2013).

210. Grepstad, J. O. *et al.* Finite-size limitations on quality factor of guided resonance modes in 2d photonic crystals. *Opt. Express* **21,** 23640–23654 (2013).
211. Galli, M. *et al.* Light scattering and Fano resonances in high-Q photonic crystal nanocavities. *Appl. Phys. Lett.* **94,** 71101 (2009).
212. Munk, B. A. Frequency selective surfaces theory and design. john Wiley&Sons. (2000).
213. Wang, F. & Shen, Y. R. General properties of local plasmons in metal nanostructures. *Phys. Rev. Lett.* **97,** 206806 (2006).
214. Chu, Y., Schonbrun, E., Yang, T. & Crozier, K. B. Experimental observation of narrow surface plasmon resonances in gold nanoparticle arrays. *Appl. Phys. Lett.* **93,** 181108 (2008).
215. Auguié, B. & Barnes, W. L. Collective resonances in gold nanoparticle arrays. *Phys. Rev. Lett.* **101,** 143902 (2008).
216. Barth, A. & Zscherp, C. What vibrations tell about proteins. *Q. Rev. Biophys.* **35,** 369–430 (2002).
217. Lewin, L. The electrical constants of a material loaded with spherical particles. *Electr. Eng. III Radio Commun. Eng. J. Inst.* **94,** 65–68 (1947).
218. Miroshnichenko, A. E. & Kivshar, Y. S. Fano resonances in all-dielectric oligomers. *Nano Lett.* **12,** 6459–6463 (2012).
219. Kuznetsov, A. I., Miroshnichenko, A. E., Fu, Y. H., Zhang, J. & Luk'yanchuk, B. Magnetic light. *Sci. Rep.* **2,** (2012).
220. Schuller, J. A., Zia, R., Taubner, T. & Brongersma, M. L. Dielectric metamaterials based on electric and magnetic resonances of silicon carbide particles. *Phys. Rev. Lett.* **99,** 107401 (2007).
221. Ginn, J. C. *et al.* Realizing Optical Magnetism from Dielectric Metamaterials. *Phys. Rev. Lett.* **108,** 097402 (2012).
222. Moitra, P. *et al.* Realization of an all-dielectric zero-index optical metamaterial. *Nat. Photonics* **7,** 791–795 (2013).
223. Staude, I. *et al.* Tailoring directional scattering through magnetic and electric resonances in subwavelength silicon nanodisks. *ACS Nano* **7,** 7824–7832 (2013).
224. West, P. R. *et al.* Searching for better plasmonic materials. *Laser Photon. Rev.* **4,** 795–808 (2010).
225. Mousavi, S. H. H. H. *et al.* Inductive tuning of Fano-resonant metasurfaces using plasmonic response of graphene in the mid-infrared. *Nano Lett.* **13,** 1111–1117 (2013).
226. Goldstein, D. H. Polarized light. (2010).
227. Chen, Y., Li, H. & Li, M. Flexible and tunable silicon photonic circuits on plastic substrates. *Sci. Rep.* **2,** 622 (2012).
228. Emani, N. K. *et al.* Electrically tunable damping of plasmonic resonances with graphene. *Nano Lett.* **12,** 5202–5206 (2012).
229. Stott, S. L. *et al.* Isolation and characterization of circulating tumor cells from patients with localized and metastatic prostate cancer. *Sci. Transl. Med.* **2,** 25ra23–

25ra23 (2010).
230. Pinzani, P. *et al.* Isolation by size of epithelial tumor cells in peripheral blood of patients with breast cancer: correlation with real-time reverse transcriptase–polymerase chain reaction results and feasibility of molecular analysis by laser microdissection. *Hum. Pathol.* **37,** 711–718 (2006).
231. Stott, S. L. *et al.* Isolation of circulating tumor cells using a microvortex-generating herringbone-chip. *Proc. Natl. Acad. Sci.* **107,** 18392–18397 (2010).
232. Yu, M., Stott, S., Toner, M., Maheswaran, S. & Haber, D. A. Circulating tumor cells: approaches to isolation and characterization. *J. Cell Biol.* **192,** 373–382 (2011).
233. Shim, S., Stemke-Hale, K., Noshari, J., Becker, F. F. & Gascoyne, P. R. C. Dielectrophoresis has broad applicability to marker-free isolation of tumor cells from blood by microfluidic systems. *Biomicrofluidics* **7,** 011808 (2013).
234. Kirby, B. J. *Micro-and nanoscale fluid mechanics: transport in microfluidic devices*. (Cambridge University Press, 2010).
235. Herbert A. Pohl, I. H. Separation of Living and Dead Cells by Dielectrophoresis. *Science* **152,** 647 (1966).
236. Slater, J. C. Microwave electronics. *Rev. Mod. Phys.* **18,** 441 (1946).
237. Dombrowski, G. E. Matrix formulation of Slater's cavity perturbation theorem. *J. Appl. Phys.* **55,** 2648–2650 (1984).

Vita

Nihal Arju attended Birbhum Zilla School in Birbhum district, West Bengal, India. He completed his undergraduate studies at the Presidency College, Kolkata earning a Bachelor of Science degree with honors. He then moved to the Indian Institute of Science for graduate studies as an Integrated PhD student. There he did research with Prof. Venki Venkataraman on field effect in semimetals. He decided to move to the University of Texas at Austin to complete his graduate studies and from 2009-2016 he was a graduate student at Prof. Gennady Shvets' lab.

This dissertation was typeset by the author.